

# **Chemical Sensing Using Novel Silicon Photonic Devices and Materials**

**A thesis submitted to the University of Manchester for the  
degree of**

**Doctor of Philosophy**

**in the Faculty of Science and Engineering.**

**2017**

**Siham Mohamed Ahmed Hussein**

**School of Electrical and Electronic Engineering**

Blank page

## **Table of content**

<b>Table of content</b> .....	<b>3</b>
<b>List of figures</b> .....	<b>7</b>
<b>Abstract</b> .....	<b>9</b>
<b>Declaration</b> .....	<b>11</b>
<b>Copyright statement</b> .....	<b>11</b>
<b>Publications related to this thesis</b> .....	<b>12</b>
<b>Acknowledgements</b> .....	<b>13</b>
<b>Chapter 1: Introduction</b> .....	<b>14</b>
<b>1.1. General background</b> .....	<b>14</b>
<b>1.2. Silicon Photonics</b> .....	<b>18</b>
<b>1.3. Silicon photonic devices for chemical sensing applications</b> .....	<b>20</b>
<b>1.4 Broad objectives and scope of the research</b> .....	<b>21</b>
<b>1.5. Outline of this thesis</b> .....	<b>21</b>
<b>1.6. References</b> .....	<b>23</b>
<b>Chapter 2: Evanescent field based bio- and gas/vapour sensing with SOI micro-ring resonators</b> .....	<b>28</b>
<b>2.1. Introduction</b> .....	<b>28</b>
<b>2.2. Evanescent wave sensing</b> .....	<b>29</b>
<b>2.3. Theory and operation principle of micro-ring resonators</b> .....	<b>31</b>
<b>2.4 Spectral characteristics</b> .....	<b>36</b>
<b>2.4.1. Quality factor Q</b> .....	<b>36</b>
<b>2.4.2. Free spectral range (FSR)</b> .....	<b>37</b>
<b>2.4.3. Finesse (F)</b> .....	<b>37</b>
<b>2.4.4. Extinction ratio (ER)</b> .....	<b>37</b>
<b>2.5. Losses in a silicon ring resonators</b> .....	<b>38</b>
<b>2.6. Waveguide geometry of ring resonator based biosensors</b> .....	<b>38</b>
<b>2.6.1. Photonic wire waveguides</b> .....	<b>38</b>
<b>2.6.2. Photonic Rib waveguides</b> .....	<b>39</b>
<b>2.6.3. Photonic Slot waveguides</b> .....	<b>40</b>
<b>2.7. Coupling light into/out of the waveguide</b> .....	<b>43</b>
<b>2.8. Waveguide sensing materials</b> .....	<b>43</b>
<b>2.9. Optical ring resonator based sensor performance metrics</b> .....	<b>44</b>
<b>2.9.1. Sensitivity</b> .....	<b>44</b>

2.9.2. Selectivity .....	46
2.9.3. Resolution .....	46
2.9.4. Limit of Detection (LOD) .....	46
2.9.5. Dynamic range.....	47
2.9.6. System noise.....	47
2.9.7. Cost .....	48
2.9.8. Portability .....	49
2.8.9. Response time/Recovery time.....	49
2.10. Surface functionalization of silicon photonic chips for bio-chemical sensing .....	49
2.10. References .....	51
Chapter 3: Experimental Methods.....	57
3.1. Sample details .....	57
3.1.1. Strip waveguide based racetrack resonators.....	57
3.1.2. Slot waveguide based ring resonators .....	58
3.2 Synthesis methods .....	58
3.2.1 Chemical vapour deposition (CVD) .....	58
3.2.2. Spin coating .....	59
3.3. Structural characterization techniques.....	60
3.3.1. Raman spectroscopy .....	60
3.3.2. Atomic force microscopy (AFM) .....	64
3.3.3. Scanning Electron Microscopy (SEM) .....	65
3.4. Waveguide optical transmission .....	66
3.4.1. Free-space spectroscopic (tuneable laser with InGaAs array) .....	66
3.4.2. Free-space spectroscopic (broadband SLED and detection via OSA) .....	68
3.5. Vapour sensing characterization .....	68
3.5.1. Vapour sensing system.....	68
3.5.2. Optical gas sensing measurements .....	70
3.6. Measurement instruments.....	70
3.6.1. Tunable laser .....	70
3.6.2. BayspecSuperGamut© spectrometer .....	71
3.6.3. Broadband source .....	71
3.6.4. Optical Spectrum Analyzers (OSAs).....	71
3.6.5. Monitoring System .....	71

<b>Chapter 4: Experimental and theoretical study of monolayer graphene coated silicon MRRs.....</b>	<b>75</b>
4.1. Determination of the quasi-TE mode (in-plane) graphene linear absorption coefficient via integration with silicon-on-insulator cavity ring resonators .....	75
4.1.1. Introduction .....	75
4.1.2. Sample preparation and characterization .....	77
4.1.2.1 Sample layout and cleaning.....	77
4.1.2.2 Raman Spectroscopy characterization.....	78
4.1.2.3. AFM scanning characterization .....	79
4.1.3. Results and dissuasion .....	80
4.1.3.1 Optical transmission measurements of cavity resonator's before coating with graphene .....	81
4.1.3.2. Optical transmission measurements of the RR's after coating with Graphene.....	83
4.2. Model of the graphene optical losses (based on the height-length parameters) for racetrack resonators and discussion .....	87
4.3. Summary .....	91
4.4. References .....	92
5.1. Introduction.....	95
5.2. Experimental details .....	96
5.2.1. Sample layout .....	96
5.2.2. Raman mapping characterisation .....	96
5.3. Results and discussion .....	97
5.3.1. Raman line scan mapping .....	97
5.3.1. Raman areal mapping .....	97
5.4. Conclusion.....	109
5.5. References .....	110
<b>Chapter 6: Investigation of the light absorption in graphene oxide incorporated into hybrid silicon slot waveguide based ring resonators.....</b>	<b>113</b>
6.1. Introduction .....	113
6. 2.Experimental details .....	114
6. 2.1. Sample layout .....	114
6.2.2. Preparation of GO incorporated cavity resonators .....	115
6.3. Structure characterization and results.....	115
6.3.1. SEM scanning characterization .....	115

6.3.2. Raman Spectroscopy characterisation and results .....	117
6.4. Optical characterisation .....	119
6.5. Optical results and discussion .....	119
6.6. Conclusion.....	126
6.7. References .....	127
7.1. Introduction .....	130
7.2 Experimental details .....	130
7.2.1 Optical device and GO synthesis .....	130
7.2.2 Sensing characterisation.....	131
7.3. Results and discussion .....	132
7.5 References .....	150
Chapter 8: Conclusions and future work .....	153
8.1 Conclusion.....	153
8.2 Future work .....	154

## List of figures

Figure 1.1 Illustration of a refractive index sensing approach using a surface functionalized micro-ring resonator (MRR)[19]. Analyte binding to the functionalised MRR alters the resonant condition leading to a measurable change in wavelength (or intensity at a fixed wavelength) as a result of small changes in the near-surface refractive index.	16
Figure 1.2 Schematic of silicon Rib- and Ridge-type waveguides lithographically derived from 220nm SOI, courtesy of <a href="http://www.3dic.org/Waveguide">http://www.3dic.org/Waveguide</a> [46]	19
Figure2.1:(a)schematic represents evanescent field (EF) sensing. The bio-molecular interaction takes place on the waveguide surface (core) inside the evanescent area, which influences the $n_{eff}$ of the transmitted mode light	34
Figure2.2 Schematic view of a regular ring coupled to single bus waveguide	31
Figure2.3 Add drop ring resonator, the input field amplitude is denoted by $E_{i1}$ , transmitted field is denoted by $E_{t1}$ and dropped field amplitude by $E_{t2}$ , with field coupling factors, $\kappa_1$ and $\kappa_2$	32
Figure2.4 Through port transmission spectra of ring resonator	35
Figure2.5Through and drop port transmission spectra of add drop RR, where red and black spectra represent intensity of through port and blue and green spectra for the drop port	36
Figure2.6 Shows cross section of wire waveguide type	39
Figure2.7 Shows cross section of rib waveguide type	40
Figure2.8overhead view of a slot waveguide	41
Figure2.9 Shows image of a slot-based MRR in $\text{Si}_3\text{N}_4$ used by Barrios et al for the biochemical sensing	42
Figure3.1 Energy level diagrams showing the states involved in the Raman Effect	62
Figure3.2 Raman spectrum with peak for $\text{SiO}_2$ /Si wafer	62
Figure3.3 calculated phonon dispersion of graphene	62
Figure3.4 Raman spectra of single layer of graphene coated $\text{SiO}_2$ /Si wafer	62
Figure3.5 An optical image showing SOI ring resonator of 25 $\mu\text{m}$ radius.(b) SEM image cross section view of a GO film on an SOI waveguide.	66
Figure3.6 Schematic representation of optical set-up testing platform	67
Figure3.4 Shows gas circuit diagram	69
Figure4.1 Microscope image for the top view of the fabricated SOI nanowires with graphene on the top (b) Schematic of the graphene integrated race-track resonator; the image illustrates the selective (partial) coverage of the racetrack at the coupling section with the uncoated	78
Figure4.2 Raman spectra with peaks for single layer graphene	79
Figure4.3 AFM topographic image of CVD graphene coated cavity resonator (b) AFM thickness measurement of graphene using height profile between ON and OFF graphene sample	80
Figure4.4 Measured transmission spectrum at the throughput port of the silicon racetrack resonator with no graphene (physical dimensions, $r = 40\mu\text{m}$ and $L_c = 13\mu\text{m}$ ).	82
Figure4.5 Measured (red) and modelled (Eq. (4.1) blue line,) transmission spectra of two corresponding graphene integrated silicon racetrack resonators with (top) $r = 10\mu\text{m}$ and (bottom) $r = 20\mu\text{m}$ .	83
Figure4.6 Measured (red) and modelled (Eq. (4.1) blue line) transmission spectra of six different sizes racetrack ring resonator with varying radii and coupling lengths	85
Figure4.7 Measured peak extinction as a function of graphene length	86
Figure4.8 (a): Contour plots of the signal loss ( $A_g$ ) as a function of length, $L_g$ and height, $h$ of graphene over the silicon cavity resonator.	88
Figure5.1 Raman spectra of single layer of graphene coated $\text{SiO}_2$ /Si wafer	97
1Figure5.2 Typical Graphene G Raman peaks the underlying silicon MRR waveguide structure (a) OFF ring, and (b) ON ring. Lines represent double Lorentzian fits to the measured data. The asymmetry in the G-peak as a result of the lowering of the degeneracy of the in-plane $E_{2g}$ optical phonon and these distinct scattering modes are labelled $G^+$ and $G^-$ .	98

Figure5.3 Typical 2D Raman peaks the underlying silicon ring waveguide structure (a) OFF-ring, and (b) ON-ring. Red lines represent single Lorentzian fits to the measured data.	99
Figure5.4:(a, b) Optical images of the graphene coated, 10 $\mu$ m radius MRRs, (c, d) Raman mapping area of the G and 2D peak position, (e, f) Raman mapping area of Fermi level	103
Figure5.5 Optical images of the graphene coated, 20 $\mu$ m radius MRR, (c, d) Raman mapping area of the G and 2D peak position, and (e, f) Raman mapping area of Fermi level maps	104
Figure5.6: The Fermi level as a function of spatial coordinate along the mapping line scans for 10 $\mu$ m cavity (top), and (bottom) 20 $\mu$ m radius cavity.	106
Figure5.7 Correlation plot showing data for three line-scan measurements across the graphene integrated ring resonator.	107
Figure6.1(a) SEM image of uncoated silicon MRR, (b-f) scanning electron microscope images of the silicon ring resonator coating with different GO concentrations	116
Figure6.2 Shows Raman characterization of GO is obtained for different GO concentrations	118
Figure6.3 Measured (red) transmission spectrum for a silicon cavity ring resonator	121
Figure6.4 (a-e) measured (red) and fitted (eq. (2.6), blue) transmission spectra (left side).	123
Figure6.5 Shows the relationship of data point of the measured peak extinction of MRR and the concentration of GO placed on these cavities.	124
Figure6.6 Shows the linear relationship between the measured peak extinction and the concentration of GO	125
Figure7.1 Comparison of the optical transmission spectra of the MRR before (black) and after (red) coating with GO	133
Figure7.2 Measured transmission spectra for (a) uncoated and (b) GO coated MRR as a function of ethanol vapour concentration	134
Figure7.3 Cavity resonance wavelength shift with ethanol concentration for (a) bare MRR and (b) GO coated MRR.	135
Figure7.4 Resonant wavelength shift with ethanol vapour concentration (in the low concentration limit) for (a) bare and (b) GO coated MRR	137
Figure7.5 Dynamic ethanol vapour sensing characteristics for a) bare and (b) GO coated MRR cavities.	138
Figure7.6 Measured transmission spectra of (a) bare and (b) GO coated MRR as a function of pentene vapour concentration	140
Figure7.7 Cavity resonance wavelength shift with pentene concentration for (a) bare MRR and (b) GO coated MRR.	141
Figure7.8 Dynamic pentene vapour sensing characteristics for a) bare and (b) GO coated MRR cavities.	142
Figure7.9 Measured transmission spectra of (a) bare and (b) GO coated MRR as a function of acetone vapour concentration	144
Figure7.10 Cavity resonance wavelength shift with acetone concentration for (a) bare MRR and (b) GO coated MRR	145
Figure7.11 Real-time acetone vapour sensing characteristics of sensors characteristics at 110ppm concentration based on a) uncoated, and (b) on GO coated cavity resonators	146



## Abstract

This thesis presents a detailed study of chip based silicon photonic waveguide technologies for chemical sensing applications. The project specifically focuses on the use of strip and slot waveguide based micro-ring resonators (MRRs) integrated with graphene and graphene oxide (GO) as potential functional sensor coatings.

The primary objective is to understand the effect of graphene/GO on the optical properties of such a device, to assess performance in bio-/chemical sensing applications and to identify ways in which such a device may be optimised. A detailed analysis of how the MRR cavity optical extinction ratio (ER) varies with the interaction length of surface integrated graphene reveals, for the first time using this technique, the in-plane graphene linear absorption coefficient,  $\alpha_{g_{TE}} = 0.11 \pm 0.01 \text{ dB}\mu\text{m}^{-1}$ . A model of the MRR cavity optical losses for different graphene lengths and heights (above the waveguide surface) provides a predictive capability for the design rules of optimised performance in sensing and photo-detector based applications.

The graphene integrated MRRs were also characterized by a Raman mapping technique from which careful analysis of the graphene G and 2D scattering peak frequencies and relative intensities revealed that the graphene is electrically intrinsic where it is suspended over the MRR yet moderately hole-doped where it sits on top of the waveguide structure. This ‘pinning’ of the graphene Fermi level at the graphene-silicon/SiO<sub>2</sub> interface is the result of ‘trapped’ ad-charges, the concentration of which may be increased at dangling bond sites after relatively aggressive (O<sub>2</sub> plasma) cleaning of the silicon/SiO<sub>2</sub> surface prior to graphene transfer. Quantifying this substrate doping effect is critically important when attempting to determine graphene’s optical properties and should be taken into account when designing graphene-silicon hetero-structures for opto-electronic devices.

The large absorption coefficient determined for the graphene integrated MRR devices means that cavity losses are far too high for practical realisation of refractive index based sensing. However, an alternative approach using GO as the functional layer for improved MRR based refractive index sensors remains a possibility on account of the much lower transmission loss. GO also has distinct

advantages over graphene; ease of integration, a high density of surface functional groups and micro-porosity. Transmission spectral analyses of both bare (uncoated) MRRs and those coated with different GO concentrations revealed the in-plane linear absorption coefficient for the GO film to be  $\alpha_{\text{GOTE}} = 0.027 \pm 0.02 \text{ dB} \mu\text{m}^{-1}$ , which is much lower than that for graphene.

Construction of a gas cell and integrated 'bubbler' arrangement for delivering variable vapour concentrations to the graphene/GO integrated MRR devices under test is presented. Both bare and GO coated MRRs were exposed to vapours from a series of typical organic solvents; ethanol, pentene and acetone delivered by a carrier gas ( $\text{N}_2$ ). Dynamic optical tracking of the MRR cavity resonance wavelength during vapour exposure, at different flow rates (vapour concentrations) reveals the sensitivity of the device(s) to small changes in refractive index. The dynamic response of the GO coated MRRs to the vapours were up to three times faster than the uncoated MRR with similar improvements in sensitivity and limit of detection, largely attributable to the porous nature and molecular binding affinity of the GO. Critically, these experiments reveal that the detection sensitivity and response of the GO is solvent dependent, which may mean that it is capable of providing a degree of selectivity, which is normally difficult to achieve in refractive index based gas sensing.

## **Declaration**

No portion of the work referred to in this thesis has been submitted in support of an application for another degree or qualification of this or any other university or institute of learning.

## **Copyright statement**

The author of this thesis (including any appendices and/or schedules to this thesis) owns certain copyright or related rights in it (the "Copyright") and he has given The University of Manchester certain rights to use such Copyright, including for administrative purposes.

Copies of this thesis, either in full or in extracts and whether in hard or electronic copy, may be made only in accordance with the Copyright, Designs and Patents Act 1988 (as amended) and regulations issued under it or, where appropriate, in accordance with licensing agreements which the University has from time to time. This page must form part of any copies made.

The ownership of certain Copyright, patents, designs, trade-marks and other intellectual property (the "Intellectual Property") and any reproductions of copyright works in this thesis, for example graphs and tables ("Reproductions"), which may be described in this thesis, may not be owned by the author and may be owned by third parties. Such Intellectual Property and Reproductions cannot and must not be made available for use without the prior written permission of the owners(s) of the relevant Intellectual Property and/or Reproductions.

Further information on the conditions under which disclosure, publication and commercialisation of this thesis, the Copyright and any Intellectual Property and/or Reproductions described in it may take place is available in the University IP policy (see <http://www.campus.manchester.ac.uk/medialibrary/policies/intellectualproperty.pdf>). in any relevant Thesis restriction declarations deposited in the \university Library's regulations (see <http://www.manchester.ac.uk/library/aboutus/regulations>) and in The University's policy on presentation of Theses.

## **Publications related to this thesis**

- (1) Chapter 4 of this thesis describes work, which has been published as “Determination of the quasi-TE mode (*in-plane*) graphene linear absorption coefficient *via* integration with silicon-on-insulator racetrack cavity resonators”, Optics express, 2014. 22(15): p. 18625-18632.
- (2) Chapter 5 of this thesis describes work, which has been published as “Raman mapping analysis of graphene integrated silicon micro-ring resonators”, Nanoscale Res. Lett., 2017 Nov 22;12(1):600.

## **Acknowledgements**

I would like to express my sincere gratitude and appreciation to my supervisor, Professor Matthew Halsall and my co-supervisor Dr Iain Crowe for their support and guidance during my doctoral study.

I would like to thank Mr Eric Whittaker for laboratory assistance and helping me design and build the gas cell and vapour handling system.

Many thanks also go to my colleague, Dr Thomas Catherall from our group for his help and cooperation.

I would like to express my gratitude to my Mum, my husband, my son, and my friend for their love and support throughout my life.

## Chapter 1: Introduction

### 1.1. General background

Chemical sensors are becoming increasingly important tools to provide chemical information ranging from analyte concentration and molecular and bio-molecular binding structure [1-5]. Intensive research in developing bio/chemical sensors by academia and industry for sensitive and fast detection has been conducted over several decades and has resulted in numerous devices. Optical based techniques are amongst those that have proven the most interesting for bio/gas sensing, due to the possibility of label-free and fast monitoring.

Optical sensors based on the silicon photonics platform have attracted a great deal of interest for research and development in the past decade. This is mainly due to the growing demand for low cost, mass-scalable, miniaturised sensing platforms in the areas of environmental monitoring and medical diagnoses. In addition the wide ranging material compatibility means that silicon photonics based sensing devices offer considerable promise and potential for other industrial applications. Research in optical sensors has resulted in a number of techniques with many signal transduction pathways, including transmission, fluorescence, absorbance, polarization, and refractive index (RI). Among these mechanisms, RI-based photonic devices have been applied as bio-and gas sensing and reported for detection of ultra-small concentrations of analyte [6]. They including surface plasmon resonance sensors [6,7], resonant micro-cavity based waveguide sensors [8,9], optical fibre, photonic crystal, and interferometers [10-12]. These sensors allow for rapid, direct and sensitive detection of molecular interactions at dielectric interfaces [6]; however some of the sensors are only suitable for measurements of relatively large biological molecules on the scale of 100nm, such as proteins and DNA or in the presence of relatively high concentrations of gas molecules. Much of the research in this area has been directed towards improving the sensitivity and selectivity whilst minimising size, cost and development time of these optical sensors. In this thesis, waveguide based silicon on insulator (SOI) photonic cavity devices based on micro ring resonators (MRRs) have been chosen for the sensor. The MRR is a well-studied photonic waveguide based device, in which the wavelength specific mode confinement of light arises from the high refractive index contrast at the

silicon/air or silicon/SiO<sub>2</sub> interface. Such cavity resonators are routinely fabricated using optical or e-beam lithography techniques with sub- $\mu\text{m}$  precision, to define a ring waveguide positioned adjacent (typically 100-300nm) to a straight section (rib or strip) bus-waveguide, providing a low loss resonant cavity [13]. The efficiency with which the evanescent coupling of the guided mode (between bus and ring) is achieved can be extremely high, and the cavity losses very low, resulting in long lived (storage) of the optical signal in the cavity. This provides sub-nm spectral resonances in the transmission spectrum of the bus waveguide, the precise wavelength and intensity of which is a strong function of the device geometry and, critically, the near surface RI of the ring. The tightly confined, intense evanescent field in the ring cavity strongly interacts with surface bound molecules providing for sensing [9,14,15] via small changes in RI as a result of the measurement of small spectral shifts in resonant wavelength or intensity variation at a specific wavelength [16-18]. The schematic in Figure1.1 depicts the basic working principle of a RI sensing scheme with SOI MRRs[19].

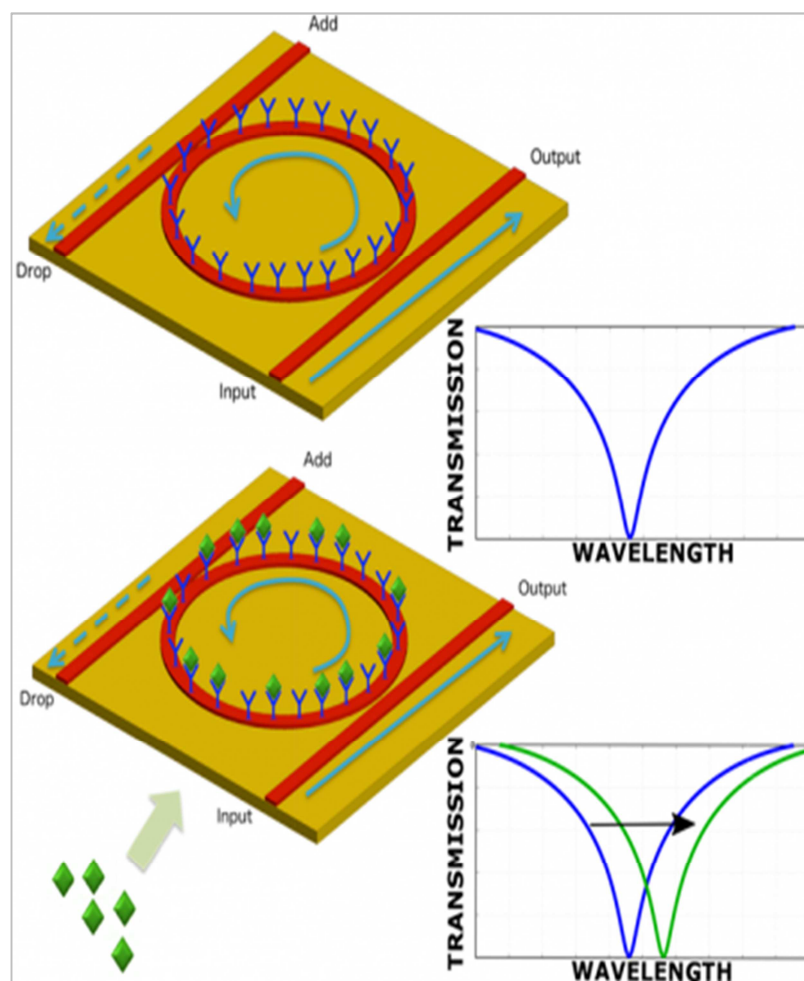


**Figure 1.1 Illustration of a refractive index (RI) sensing approach using a surface functionalized micro-ring resonator (MRR)[19]. Analyte binding to the functionalised MRR alters the resonant condition leading to a measurable change in wavelength (or intensity at a fixed wavelength) as a result of small changes in the near-surface RI.**

Whilst the principle of operation is straightforward, effective bio, chemical and gas based optical sensing is highly dependent on the precise surface chemistry. However, appropriate functionalization of the silicon surface is complicated by its relatively poor reactivity, which is an obstacle to the effective detection through reactions of biological or gaseous surface bound molecules. The route to achieving high sensitivity and selectivity from such chip based sensors is through the application of specific surface coatings. For gas/vapour sensing, one-dimensional (1D) semiconducting metal oxides have been widely investigated due to their high sensitivities toward different gaseous target analytes[20,21]. Recently, two-dimensional (2D) graphene and its derivatives consisting of hexagonally arrayed sp<sup>2</sup>-bonded carbon atoms [22] has been investigated



for photonic applications due to its superior thermal[23], electrical [24] and mechanical [25] properties and its large surface area make it a promising bio- and gas-sensing material [26,27].

In this work CVD graphene is integrated with silicon strip waveguide based MRR devices in order to determine its effect on the optical properties of the device and its potential as a surface functional layer for sensing. Graphene has a very large specific surface area of  $2630 \text{ m}^2\text{g}^{-1}$ , it is available commercially in high chemical purity, has high reactivity and can be functionalized [28]. Graphene's ability to interact with various biomolecules such as proteins, and nucleic acid by virtue of  $\pi$ - $\pi$  interaction is well studied [29]. However, there are several difficulties in obtaining the perceived benefits from CVD monolayer graphene film technology for optical based vapour/gas sensing, chiefly because of the significant, broadband optical absorption. RI changes introduced by vapour/gas molecules can be extremely small, requiring precise measurement of spectral shifts of the resonant wavelength in MRR cavity type devices, which is challenging if the losses introduced by the graphene are too severe. Also the transfer of CVD graphene, from the growth substrate, typically copper foil, to the silicon waveguides is a relatively complicated, multi-step process requiring a clean environment.

Recently, waveguide coating by a graphene oxide (GO) film through drop casting from solution has been reported [30]. This represents a relatively simple alternative for coating thin graphene-based films over large areas. Graphene oxide synthesis and transfer is extremely simple and can cover large surface areas, has lower optical absorption and is lower cost. These advantages mean that GO based gas/vapour sensors may represent the best route to achieving high performance optical based vapour/gas sensors.

In the following sections of this chapter, we first briefly introduce the basics of silicon integrated photonics in Sec.1.2, and expand this to silicon photonic devices specifically focussed on chemical sensing applications in Sec.1.3. The objectives and scope of the research are described in Sec.1.4 and the outline of the remainder of the thesis is given in Sec.1.5.

## 1.2. Silicon Photonics

In the field of optical communications, light is used as an information carrier. This field started with the discovery of the laser in the 1960s. Other advances followed, such as the laser diode in the 1970s and optical fibres for data transmission [31]. These discoveries created the basis for moving from bulky components to integrated photonic technologies [32].

Since Richard Soref first pioneered silicon photonics in the mid 1980's, enormous advances and worldwide academic effort in nanophotonic technology and applications has been reported. Silicon photonic components represent one of the promising technologies for incorporated photonics with high level of functionality, which can address a large variety of applications [33]. Its compatibility with well-known high-density complementary metal-oxide-semiconductor (CMOS) fabrication process offers advantages, such as high volume, low-cost production and extremely reliable fabrication with nano-scale precision [9,34-36]. These optical circuits can provide a platform for chip-to-chip and on-chip data transmission, which remains the key driver for the technology [9,10].

For more varied applications, silicon photonics has been integrated with several different material systems using the standard fabrication processes of integrated microelectronics systems, including III-V semiconductors and polymers alongside the CMOS mainstays of silicon dioxide ( $\text{SiO}_2$ ) and silicon-on-insulator (SOI) [37-41]. The main reason of use of silicon in photonics is due to the enormous possibilities for mass production offered by the CMOS foundry and thus the ability to monolithically incorporate electronics and optics, however, this aside it is an excellent dielectric medium for the guiding of infrared light [34,36], which includes the standard telecom wavelength range (1300-1550nm)[37]. The refractive index of silicon is relatively high, ranging from 3.4–3.6 depending upon the wavelength.  $\text{SiO}_2$  is also transparent in this wavelength range, but with lower index around 1.4–1.5 depending upon the quality. However, there are some drawbacks of silicon based photonic components; silicon has low light emission efficiency due to its indirect band gap, meaning that full integration of light sources with the silicon photonics platform is complicated. Silicon also has relatively high propagation losses (compared with silica based optical fibre) mainly as a result of side wall scattering of the waveguide, although improvements in the

fabrication processes are continuously being made to reduce this latter issue. Silicon and silicon dioxides can be combined easily for index guiding, the SOI platform is the most common in silicon photonics for integrated optics [38].

As illustrated in Fig.1.2, an SOI wafer comprises of a top silicon layer, typically 220nm thick on a silicon dioxide layer of several microns (known as buried oxide or BOX) on a supporting silicon substrate. Patterning of the top Si layer, by e-beam or photolithography, to form single- or multi-mode rib- or ridge-type waveguides is achieved in a commercial fabrication facility (e.g. CEA-LETI, France, IMEC, Belgium and A-star, Singapore)[42]. In the case of the devices described in this work, waveguide dimensions were designed around single mode operation in the near-infrared (near-IR). The light is guided by the high refractive index contrast between the core (silicon at  $n_{Si} \approx 3.48$ ) and the lower cladding layer ( $SiO_2$  at  $n_{SiO_2} \approx 1.45$ )[43-45] by total internal reflection. The high index contrast has the distinctive advantage, for chip based photonic applications, of strong confinement of the propagating mode, which allows for waveguides with extremely tight bend radii, leading to ultra-compact devices. For improved modal overlap with surface functional layers, i.e. for extended evanescent field interaction with surface bound species for sensing, one can reduce the waveguide dimensions, usually at the cost of marginally increased, although acceptable propagation and scattering losses [13,17].

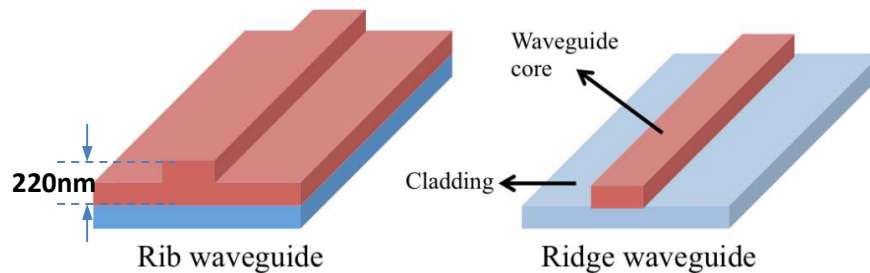


**Figure 1.2 Schematic of silicon Rib- and Ridge-type waveguides lithographically derived from 220nm SOI, courtesy of <http://www.3dic.org/Waveguide>[46]**

All this is achievable with scalable production techniques that are fully compatible with the CMOS process, making the technology highly attractive for mass produced optical devices.

### **1.3. Silicon photonic devices for chemical sensing applications**

Although the development of silicon photonics devices is mainly driven by telecommunications, its application to the field of sensing is becoming increasingly popular. Many photonic device architectures have been explored for achieving enhanced sensitivity in the field of chemical sensing with a wide range of novel device implementations; slot waveguides [47,48], Mach-Zehnder interferometers (MZI) [49, 50], photonic crystal waveguides [51] and micro-ring resonators (MRRs) [52,53]. Silicon photonics in chemical sensing is essentially motivated by the huge industrial, medical and environmental sensing market for which miniaturised, mass-scaled (low cost) devices is extremely attractive [54,55].

Since the early 2000s, silicon photonics has been applied to refractive index sensing applications in areas as diverse as industrial safety monitoring [56], healthcare [57] and defence [58], by taking advantage of the highly sensitive evanescent field that arises near the surface of the SOI photonic device[47,48]. Beside the figures of merit of the silicon photonic chemical sensors that we previous mentioned such as; selectivity, sensitivity, simplicity, cost effectiveness, and device footprint [16,54,59], the mass fabrication and high affinity for integration with other on-chip and micro-fluidic functions are critical factors in such applications [16,17,60]. Medical and environmental concerns are driving the development of integrated silicon photonic bio-,and gas-sensing application areas. The monitoring of health is one of the main laudable technological objectives challenging science and technology and early disease diagnosis and progress monitoring in the clinical setting are essential requirements for improved treatment and understanding of health related issues. For instance, many exhaled vapour and gaseous compounds found in human breath are markers for certain medical conditions. Among these, the presence of nitric oxide, carbon dioxide, ammonia and isoprene can be used to monitor various conditions[61]. The ultimate goal of gaseous monitoring in the biomedical sector is to detect any biomolecule (signal) associated with specific health conditions in the patient's breath to facilitate early disease diagnosis. For example, nitric oxide is a possible indicator of the early onset of bronchial tube inflammation [62,63]. Ammonia level monitoring in breath has the potential to aid the follow up of dialysis treatments on kidney patients [64] and current developments have indicated that parallel detection of some volatile organic

compounds in human breath can be used for the diagnosis of specific diseases. For instance, breath acetone is a biomarker for patients with diabetes ketoacidosis [65], liver diseases [66] and oral disease [61]. Pentane in the breath is considered as a marker of acute heart allograft rejection [67] and breath ethanol has been recognized as a biomarker in patients with hepatic injuries, and associated with non-alcoholic fatty liver diseases [66].

Gas sensors also offer the potential for applications in the Industrial sectors. As an example, food processing companies are employing optical sensors for food packaging and storage [68,69]. In this case, the presence of excessive concentrations of specific gases in packaged food products can serve as an early and accurate indicator of food spoilage. The increasing importance of environmental health and security monitoring is another area where gas sensors are finding application, e.g. for monitoring levels of toxic gases released from industrial and agricultural process [70]. Conventional gas sensor technologies such as mass spectrometers, and electrochemical sensors are overly complex, insufficiently sensitive or don't have the required selectivity for most medical and environmental applications. If a sensing technology is to be accessible to a large number of people it needs to be affordable, robust, portable and have low power consumption.

## **1. 4 Broad objectives and scope of the research**

The objectives of this research were:-

1. To investigate the surface functionalization of strip and slot waveguide based photonic MRR devices integrated with graphene and graphene oxide coatings.
2. To study the fundamentals of the photonic structures that we have employed and the properties of graphene and its derivative GO when coated onto the silicon photonic devices.
3. The development and implementation of a gas sensing device based on the knowledge gained from previous study.

## **1.5. Outline of this thesis**

This section provides an outline of the structure of the thesis. The work presented in this thesis is based on the research carried out by the author into the use of

experimental and analytical methods for characterisation and modelling of silicon photonic sensor devices. Following the introduction in Chapter 1, the background and theory behind silicon photonics MRRs is introduced in Chapter 2. This provides the theoretical background of MRRs as the main building block for chemical sensing, including the optical design, summary of the most important device performance parameters and assessment of the state-of-the-art in MRR based refractive index sensing.

Chapter 3 contains detailed experimental procedures and analytical techniques for optical material and device characterization.

Chapter4 contains the results and analysis of the optical characterization of both bare (uncoated) and monolayer CVD graphene coated MRRs. Comparison of graphene coated MRR devices of different length provides a means for determining the in-plane graphene linear absorption coefficient. This is combined with theoretical analysis to understand the effect of graphene on the optical properties in attempt to understand the practical implications for device sensitivity.

Chapter5 presents a Raman spatial mapping study of graphene G and 2D bands, after integration with MMRs to determine the effects of the graphene transfer processes on its structural and opto-electronic properties. Quantifying these effects is critically important when attempting to determine graphene's optical properties and for optimization of future graphene integrated silicon photonics devices.

Chapter 6 focuses on the integration of GO with slot waveguide based MRRs. We look at the effect of different GO concentrations to determine the optical absorption coefficient.

Finally, in chapter7, we demonstrate a vapour sensing technique based on the GO coated slot waveguide MRR, using a series of typical organic solvents; ethanol, pentene and acetone, delivered by a ( $N_2$ ) carrier gas. We compare the performance of the GO integrated device with a bare (uncoated) MRR, in terms of response time and sensitivity.

Chapter 8 completes the thesis by summarising the main conclusions of the research with a viewpoint on the potential future applications of the silicon photonics based sensors described in this thesis.

## 1.6. References

1. Justino, C.I., T.A. Rocha-Santos, and A.C. Duarte, *Review of analytical figures of merit of sensors and biosensors in clinical applications*. TrAC Trends in Analytical Chemistry, 2010. **29**(10): p. 1172-1183.
2. Yogeswaran, U. and S.-M. Chen, *A review on the electrochemical sensors and biosensors composed of nanowires as sensing material*. Sensors, 2008. **8**(1): p. 290-313.
3. Ghoshal, S., et al., *Biosensors and biochips for nanomedical applications: a review*. Sensors & Transducers, 2010. **113**(2): p. 1.
4. Rogers, K.R., *Principles of affinity-based biosensors*. Molecular biotechnology, 2000. **14**(2): p. 109-129.
5. Higson, S.P. and P.M. Vadgama, *Biosensors: a viable monitoring technology?* Medical and Biological Engineering and Computing, 1994. **32**(6): p. 601-609.
6. Hunt, H.K. and A.M. Armani, *Label-free biological and chemical sensors*. Nanoscale, 2010. **2**(9): p. 1544-1559.
7. McNaught, A.D. and A.D. McNaught, *Compendium of chemical terminology*. Vol. 1669. 1997: Blackwell Science Oxford.
8. Gorton, L., *Biosensors and modern biospecific analytical techniques*. Vol. 44. 2005: Elsevier.
9. Park, M.K., et al., *Label-free aptamer sensor based on silicon microring resonators*. Sensors and Actuators B: Chemical, 2013. **176**: p. 552-559.
10. Clark, L.C. and C. Lyons, *Electrode systems for continuous monitoring in cardiovascular surgery*. Annals of the New York Academy of sciences, 1962. **102**(1): p. 29-45.
11. Mandal, S. and D. Erickson, *Nanoscale optofluidic sensor arrays*. Optics express, 2008. **16**(3): p. 1623-1631.
12. Densmore, A., et al., *Spiral-path high-sensitivity silicon photonic wire molecular sensor with temperature-independent response*. Optics letters, 2008. **33**(6): p. 596-598.
13. Bogaerts, W., et al., *Silicon microring resonators*. Laser & Photonics Reviews, 2012. **6**(1): p. 47-73.
14. Iqbal, M., et al., *Label-free biosensor arrays based on silicon ring resonators and high-speed optical scanning instrumentation*. IEEE Journal of Selected Topics in Quantum Electronics, 2010. **16**(3): p. 654-661.
15. Ciminelli, C., et al., *High performance SOI microring resonator for biochemical sensing*. Optics & laser technology, 2014. **59**: p. 60-67.
16. Passaro, V., et al., *Recent advances in integrated photonic sensors*. Sensors, 2012. **12**(11): p. 15558-15598.
17. Ramachandran, A., et al., *A universal biosensing platform based on optical micro-ring resonators*. Biosensors and Bioelectronics, 2008. **23**(7): p. 939-944.

18. Claes, T., W. Bogaerts, and P. Bienstman, *Experimental characterization of a silicon photonic biosensor consisting of two cascaded ring resonators based on the Vernier-effect and introduction of a curve fitting method for an improved detection limit*. Optics express, 2010. **18**(22): p. 22747-22761.
19. group, P.d. *biosensing*. [cited 2017 May 2017]; Available from: <http://photonics.deib.polimi.it/biosensing/>.
20. Yebo, N.A., et al., *An integrated optic ethanol vapor sensor based on a silicon-on-insulator microring resonator coated with a porous ZnO film*. Optics express, 2010. **18**(11): p. 11859-11866.
21. Eranna, G., et al., *Oxide materials for development of integrated gas sensors—a comprehensive review*. Critical Reviews in Solid State and Materials Sciences, 2004. **29**(3-4): p. 111-188.
22. Geim, A.K. and K.S. Novoselov, *The rise of graphene*. Nature materials, 2007. **6**(3): p. 183-191.
23. Balandin, A.A., et al., *Superior thermal conductivity of single-layer graphene*. Nano letters, 2008. **8**(3): p. 902-907.
24. Novoselov, K.S., et al., *Electric field effect in atomically thin carbon films*. science, 2004. **306**(5696): p. 666-669.
25. Frank, I., et al., *Mechanical properties of suspended graphene sheets*. Journal of Vacuum Science & Technology B: Microelectronics and Nanometer Structures Processing, Measurement, and Phenomena, 2007. **25**(6): p. 2558-2561.
26. Kobayashi, Y., et al. *Integrated graphene sensor on high-Q silicon-ring resonator for neurotransmitter detection*. in *CLEO: Applications and Technology*. 2016. Optical Society of America.
27. Schedin, F., et al., *Detection of individual gas molecules adsorbed on graphene*. Nature materials, 2007. **6**(9): p. 652-655.
28. Xu, Y., et al., *Flexible graphene films via the filtration of water-soluble noncovalent functionalized graphene sheets*. Journal of the American Chemical Society, 2008. **130**(18): p. 5856-5857.
29. Guo, Q., et al., *Silicon-on-glass graphene-functionalized leaky cavity mode nanophotonic biosensor*. Acs Photonics, 2014. **1**(3): p. 221-227.
30. Chong, W., et al., *Photo-induced reduction of graphene oxide coating on optical waveguide and consequent optical intermodulation*. Scientific reports, 2016. **6**: p. 23813.
31. Soref, R.A., *Silicon-based optoelectronics*. Proceedings of the IEEE, 1993. **81**(12): p. 1687-1706.
32. *Photonics*. August 2016 September 2016 [cited 2016 august]; <https://en.wikipedia.org/wiki/Photonics>].
33. Soref, R., *Silicon photonics: a review of recent literature*. Silicon, 2010. **2**(1): p. 1-6.
34. Soref, R., *The past, present, and future of silicon photonics*. IEEE Journal of Selected Topics in Quantum Electronics, 2006. **12**(6): p. 1678-1687.
35. Kou, R., et al., *Influence of graphene on quality factor variation in a silicon ring resonator*. Applied Physics Letters, 2014. **104**(9): p. 091122.
36. Baehr-Jones, T., et al., *Myths and rumours of silicon photonics*. Nature Photonics, 2012. **6**(4): p. 206-208.
37. Soref, R., *The impact of silicon photonics*. IEICE transactions on electronics, 2008. **91**(2): p. 129-130.



38. Kurdi, B. and D. Hall, *Optical waveguides in oxygen-implanted buried-oxide silicon-on-insulator structures*. Optics letters, 1988. **13**(2): p. 175-177.
39. Vivien, L. and L. Pavesi, *Handbook of silicon photonics*. 2013: Taylor & Francis.
40. Heck, M.J., et al., *Hybrid silicon photonic integrated circuit technology*. IEEE Journal of Selected Topics in Quantum Electronics, 2013. **19**(4): p. 6100117-6100117.
41. Liang, D. and J.E. Bowers, *Recent progress in lasers on silicon*. Nature Photonics, 2010. **4**(8): p. 511-517.
42. Dumon, P. *The ePIXnet silicon photonics platform*. in *Group IV Photonics, 2007 4th IEEE International Conference on*. 2007. IEEE.
43. Jalali, B. and S. Fathpour, *Silicon photonics*. Journal of lightwave technology, 2006. **24**(12): p. 4600-4615.
44. Cortesi, E., F. Namavar, and R. Soref. *Novel silicon-on-insulator structures for silicon waveguides*. in *SOS/SOI Technology Conference, 1989., 1989 IEEE*. 1989. IEEE.
45. Dumon, P., et al., *Linear and nonlinear nanophotonic devices based on silicon-on-insulator wire waveguides*. Japanese journal of applied physics, 2006. **45**(8S): p. 6589.
46. Waveguides. 2017 [cited 2017 15/12]; Available from: [http://www.3dic.org/Waveguide#cite\\_note-1](http://www.3dic.org/Waveguide#cite_note-1).
47. Carlborg, C.F., et al., *A packaged optical slot-waveguide ring resonator sensor array for multiplex label-free assays in labs-on-chips*. Lab on a Chip, 2010. **10**(3): p. 281-290.
48. Wang, X., et al., *A silicon photonic biosensor using phase-shifted Bragg gratings in slot waveguide*. Journal of biophotonics, 2013. **6**(10): p. 821-828.
49. Yuan, D., et al., *Mach-zehnder interferometer biochemical sensor based on silicon-on-insulator rib waveguide with large cross section*. Sensors, 2015. **15**(9): p. 21500-21517.
50. Sepulveda, B., et al., *Optical biosensor microsystems based on the integration of highly sensitive Mach-Zehnder interferometer devices*. Journal of Optics A: Pure and Applied Optics, 2006. **8**(7): p. S561.
51. Jágerská, J., et al., *Refractive index sensing with an air-slot photonic crystal nanocavity*. Optics letters, 2010. **35**(15): p. 2523-2525.
52. Fard, S.T., et al. *Label-free silicon photonic biosensors for use in clinical diagnostics*. in *SPIE OPTO*. 2013. International Society for Optics and Photonics.
53. Gandolfi, D., et al. *Sensitivity and Limit of detection of biosensors based on ring resonators*. in *AISEM Annual Conference, 2015 XVIII*. 2015. IEEE.
54. De Vos, K., et al., *Multiplexed antibody detection with an array of silicon-on-insulator microring resonators*. IEEE Photonics Journal, 2009. **1**(4): p. 225-235.
55. Densmore, A., et al., *A silicon-on-insulator photonic wire based evanescent field sensor*. IEEE Photonics Technology Letters, 2006. **18**(23): p. 2520-2522.
56. Mohan, S., V. Arjunan, and S.P. Jose, *Fiber Optics and Optoelectronic Devices*. 2014: MJP Publisher.
57. Spichiger-Keller, U.E., *Chemical sensors and biosensors for medical and biological applications*. 2008: John Wiley & Sons.
58. Wieduwilt, T., et al., *Reflectivity enhanced refractive index sensor based on a fiber-integrated Fabry-Perot microresonator*. Optics express, 2014. **22**(21): p. 25333-25346.

59. Yebo, N.A., et al., *Silicon-on-insulator (SOI) ring resonator-based integrated optical hydrogen sensor*. IEEE Photonics Technology Letters, 2009. **21**(14): p. 960-962.
60. Cho, H.K. and J. Han, *Numerical study of opto-fluidic ring resonators for biosensor applications*. Sensors, 2012. **12**(10): p. 14144-14157.
61. Wang, L., et al., *Nanosensor device for breath acetone detection*. Sensor Letters, 2010. **8**(5): p. 709-712.
62. Ratnawati, R., *Exhaled Nitric Oxide in Asthmatic Airway Inflammation*, 2006, University of New South Wales.
63. Robroeks, C., et al., *Exhaled nitric oxide and biomarkers in exhaled breath condensate indicate the presence, severity and control of childhood asthma*. Clinical & Experimental Allergy, 2007. **37**(9): p. 1303-1311.
64. Narasimhan, L., W. Goodman, and C.K.N. Patel, *Correlation of breath ammonia with blood urea nitrogen and creatinine during hemodialysis*. Proceedings of the National Academy of Sciences, 2001. **98**(8): p. 4617-4621.
65. Deng, C., et al., *Determination of acetone in human breath by gas chromatography–mass spectrometry and solid-phase microextraction with on-fiber derivatization*. Journal of Chromatography B, 2004. **810**(2): p. 269-275.
66. Solga, S., et al., *Breath biomarkers and non-alcoholic fatty liver disease: preliminary observations*. Biomarkers, 2006. **11**(2): p. 174-183.
67. Sobotka, P.A., et al., *Breath pentane is a marker of acute cardiac allograft rejection*. The Journal of heart and lung transplantation: the official publication of the International Society for Heart Transplantation, 1994. **13**(2): p. 224-229.
68. Matindoust, S., et al., *Food quality and safety monitoring using gas sensor array in intelligent packaging*. Sensor Review, 2016. **36**(2): p. 169-183.
69. Puligundla, P., J. Jung, and S. Ko, *Carbon dioxide sensors for intelligent food packaging applications*. Food Control, 2012. **25**(1): p. 328-333.
70. Fine, G.F., et al., *Metal oxide semi-conductor gas sensors in environmental monitoring*. Sensors, 2010. **10**(6): p. 5469-5502.



## **Chapter 2: Evanescent field based bio- and gas/vapour sensing with SOI micro-ring resonators**

### **2.1. Introduction**

Research in optical sensors has resulted in many different types of optical sensing mechanisms with a variety of possible signal transduction pathways. These include fluorescence [1-3], Raman spectroscopy [4], optical absorption [5,6] and evanescent field sensing [7]. Among these, evanescent field sensing is widely used in biomedical, environmental and industrial sensing applications.

Evanescent field sensing with silicon nano-photonic devices has been applied to bio and gas sensing and a number of reports have demonstrated detection of ultra-small concentrations (femtoliters (fl) to nanoliters(nm)) of analyte[7-9]. Chemical surface functionalization is typically incorporated with the device structures to accomplish sensitivities to bio-molecular relevant concentrations or low gas concentrations on the interaction area [10-14]. Typically, these films are selected so that analyte specific response is achieved.

In recent years, research has focussed on optical cavity micro-ring resonators (MRRs). This is due to their attractive features of compactness and high Q-factor (leading to high sensitivity) combined with the fact that there exists a plethora of background knowledge on their design and optimisation from their mainstay application in optical communications. Optical MRRs are wavelength selective devices due to their resonant structure. The precise resonance wavelength of these devices depends, amongst other factors, on the effective refractive index of the surrounding media; therefore, the sensing using MRRs will be based on tracking the spectral change of the resonances induced by small changes in refractive index variations at the surface of the device structure due to molecular binding [15-17].

In the following sections, a more detailed overview into the evanescent field/refractive index based sensing mechanism is presented, with a focus on the silicon photonics platform. A rigorous overview of the concept of silicon photonic MRRs as sensing devices and their properties is presented including the optical design and background theory of operation and performance metrics.

## 2.2. Evanescent wave sensing

In most types of optical bio or gas sensors, a solid medium partially confines the electromagnetic field in such a manner that the evanescent portion of the propagating mode interacts with surface molecular analytes bound to an immobilized sensing element [18]. Depending on the sensor architecture in which the sensing waveguide is embedded, the electromagnetic field might be in the form of a standing or traveling wave. For a light wave to be guided by the optical sensor configuration but interact with the external medium, the structure must be judiciously designed so that the guided evanescent field extends sufficiently into the functionalised surface [19]. This can be accomplished by the correct choice of substrate, material, wavelength and waveguide dimensions. With such a device it is possible to probe extremely small biochemical changes in the very near (typically sub-100nm) surface region by the effect those changes have on the evanescent field of the propagating mode [20,21]. Typically, these changes are measured, e.g. by spectral wavelength shift (i.e. of a resonant cavity mode) or optical intensity change, indirectly through a change in the effective refractive index,  $n_{\text{eff}}$  [20,22-24]. This may be interpreted under certain controlled changes such as occurs during surface antigen-antibody interaction. This has an effect on the guided light producing a phase shift (e.g. relative to a reference beam) [20,21]. Fig 2.1 exhibits an evanescent wave biosensor where the bound molecular interaction occurs near the waveguide surface within the evanescent field, producing a change in  $n_{\text{eff}}$  of the optical waveguide mode [22]. When target analytes bind to the receptor in the sensor window, the change in  $n_{\text{eff}}$  is sensed by the evanescent field of the propagating mode and shifts the phase velocity of the guided light [19,20].

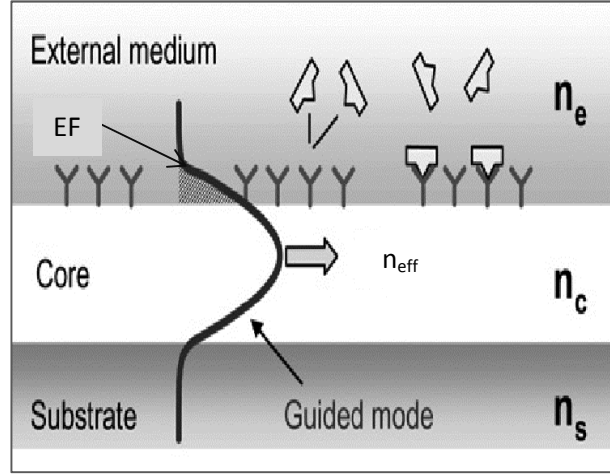


**Figure2.1: Schematic representation of evanescent field (EF) sensing. The bio-molecular interaction takes place on the waveguide surface (at the core-external medium interface) within the evanescent field, which influences  $n_{eff}$  of the propagating mode [20]**

The evanescent wave decays exponentially with distance from the waveguide core into the surrounding (lower index) medium with a decay constant,  $d$  of approximately[25].

$$d = \frac{\lambda_0}{2\pi} \left[ \frac{1}{\left( \sqrt{(n_{core})^2 - (n_{eff})^2} \right)} \right]$$

Where  $\lambda_0$  is the wavelength,  $n_{eff}$  is the effective refractive index and  $n_{core}$  is the refractive index of the substrate core.

Considering a propagating mode at 1550nm in a silicon ( $n_{core}= 3.5$ ) waveguide with a typical width of ~500nm ( $n_{eff} \sim 2.3$ )[26], then the evanescent wave decay constant,  $d < 100$ nm. Since the distance over which the evanescent field decays is very short, the biosensor preferentially interacts with those analytes at or very near to the waveguide surface.

Several optical bio-chemical sensors are based on changes of effective refractive index caused by the interaction between (near) surface bound molecules and the evanescent field. For example, the optical surface plasmon resonance sensor uses the evanescent field of a surface plasmon mode propagating at the interfaces of metal-dielectric waveguides [9,27] and the effect was demonstrated using fibre optic sensors [28,29] as

well as those demonstrated on silicon platforms; including planar waveguides [30], silicon photonic nanowires [9] and slot-waveguide based MRRs [31,32]. These typically use transducers based on spectroscopy of the guided modes of dielectric waveguides.

### 2.3. Theory and operation principle of micro-ring resonators

A ring resonator (or allowing for oval shaped waveguides the term racetrack resonator is sometimes used) is a type of optical device demonstrating periodic resonances when light traversing the ring obtains a phase shift equivalent to a multiple of  $2\pi$ . Generally, it describes a planar geometry in which a bus waveguide is coupled (spatially proximate) to a ring waveguide to form a resonant cavity. The structure of a simple all pass ring resonator which is coupled to one bus waveguide (throughput waveguide) is shown in Fig 2.2.

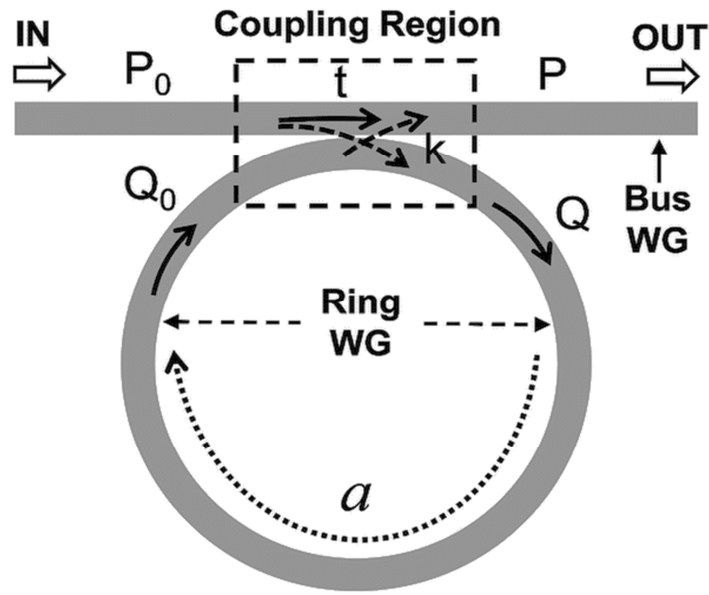
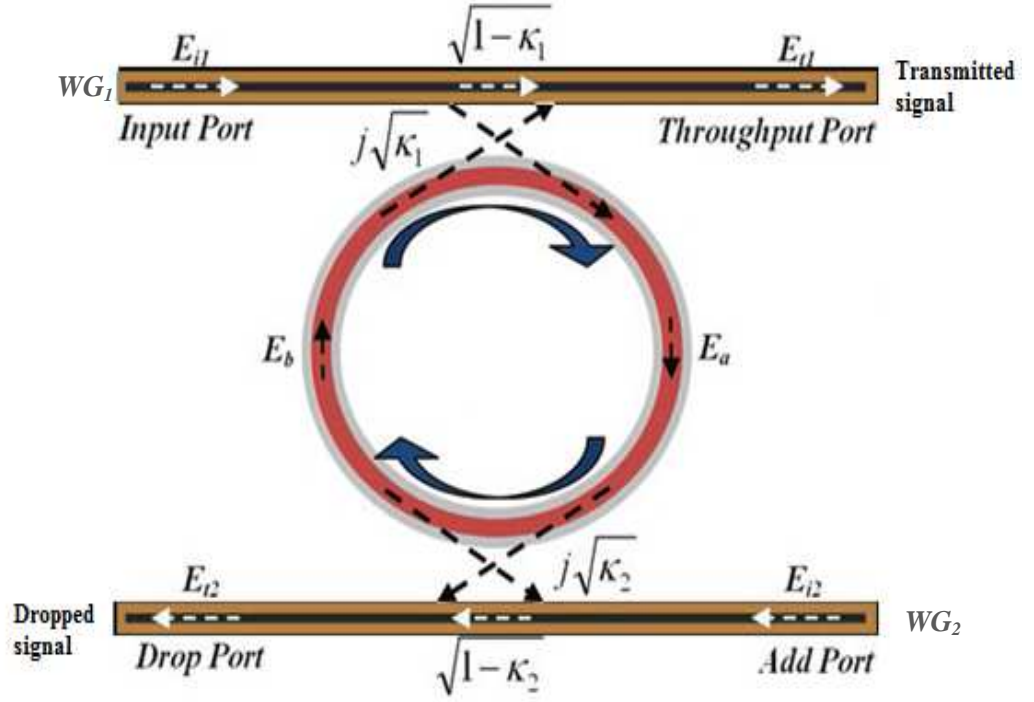


Figure 2.2 Schematic of a regular all pass ring resonator [33]

Such waveguide coupled ring resonators can also be formed with an additional (add/drop) waveguide, as illustrated in Fig.2.3. The input light in  $WG_1$  is efficiently coupled (according to the coupling factor,  $\kappa$ ) to the ring waveguide through evanescent field interaction along a section (where the spatial separation/gap is on the order of 200-300nm) at wavelengths corresponding to integer multiples of the round-trip geometry, leading to equally spaced 'notches' in the transmission spectrum. The spectral purity (width) and depth of these 'notches' is related to the photon lifetime in

the ring waveguide and so represents a measure of the cavity loss. A portion of this circulating resonant mode (the direction of the light propagation is displayed by the arrows) confined to the ring waveguide can be coupled to the add/drop guide (WG<sub>2</sub>), producing a series of spectral ‘peaks’ at the drop port [34-36].



**Figure 2.3 Schematic of an add/drop ring resonator. The input field amplitude is denoted by  $E_{i1}$ , the transmitted field by  $E_{t1}$  and the dropped field by  $E_{i2}$ , with field coupling factors,  $\kappa_1$  and  $\kappa_2$**

The cavity is on resonance when the phase-shift of the propagating mode,  $\phi$  is a multiple of  $2\pi$ , after a full round trip in the ring. This is the condition for wavelengths to be in-phase and can constructively interfere with the incident light (in the bus waveguide). Light that doesn't satisfy this resonant condition does not couple with the cavity resonator and is transmitted directly to the bus output.

The wavelength of the resonant mode in the cavity can be acquired by the following basic equation of a cavity resonator [37].



$$\lambda = \frac{L \cdot n_{eff}}{m} \quad (2.1)$$

Where  $\lambda$  is the resonant wavelength,  $L$  is the length of the cavity, equal to  $2\pi r$  for a ring ( $r$  is the radius),  $n_{eff}$  is the effective refractive index of the guide and  $m$  is an integer describing the resonance order.

In an all-pass cavity resonator shown in Fig 2.2, we can relate the incoming signal (electrical field) coupled to the cavity through the input port and the transmitted signal employing the following scattering matrix model [36, 38-40]

$$\begin{pmatrix} E_{t1} \\ E_{t2} \end{pmatrix} = \begin{pmatrix} t & k \\ -k^* & t^* \end{pmatrix} \begin{pmatrix} E_{i1} \\ E_{i2} \end{pmatrix} \quad (2.2)$$

Where  $t$  is the electric field transmission coefficient and  $k$  is the coupling coefficient for the electric field and  $*$  implies the conjugate of the values. Owing to the exchange of the structure, the matrix in Eq. (2.2) is symmetric, inducing a relation between the transmissions and coupling coefficients:

$$|t|^2 + |k|^2 = 1 \quad (2.3)$$

For simplification, we assume that  $E_{i1}$  is equal to 1, therefore the circulation condition in the ring is defined by:

$$E_{i2} = E_{t2} \cdot \alpha \cdot e^{j\phi} \quad (2.4)$$

$$\phi = \beta \cdot L \quad (2.5)$$

Where  $\alpha$  is the loss,  $\phi$  is the phase shift per round trip,  $L$  is the physical round trip length of the cavity and  $\beta$  is the waveguide propagation constant corresponding to:

$$\beta = \frac{2\pi \cdot n_{eff}}{\lambda} \quad (2.6)$$

We can calculate the input and the output signal as well as the transmitted signal in the cavity resonator by combining Eq.s 2.2-2.6 resulting in:

$$E_{t1} = \frac{-\alpha + t e^{-j\phi}}{\alpha t^* + e^{-j\phi}} \quad (2.7)$$

$$E_{i2} = \frac{-\alpha \kappa^*}{\alpha t^* + e^{-j\phi}} \quad (2.8)$$

$$E_{t2} = \frac{-\kappa^*}{1 - \alpha t^* e^{-j\phi}} \quad (2.9)$$

Finally, the relative intensities or output power at the through port is given by Eq. 2.10 [41] and plotted in Fig. 2.4, where the transmission spectra are plotted at different loss values:

$$|E_{t1}|^2 = \frac{-\tau^2 + t^2 - 2.t.\tau.\cos(\phi)}{1 + t.\tau - 2.t.\tau.\cos(\phi)} \quad (2.10)$$

Where  $t = \sqrt{1 - \kappa}$  the coupling parameter,  $\tau$  is a parameterisation of the losses and  $\phi = \left[ \frac{(4\pi^2 r n)}{\lambda} \right]$  is the phase change due to the coupler.

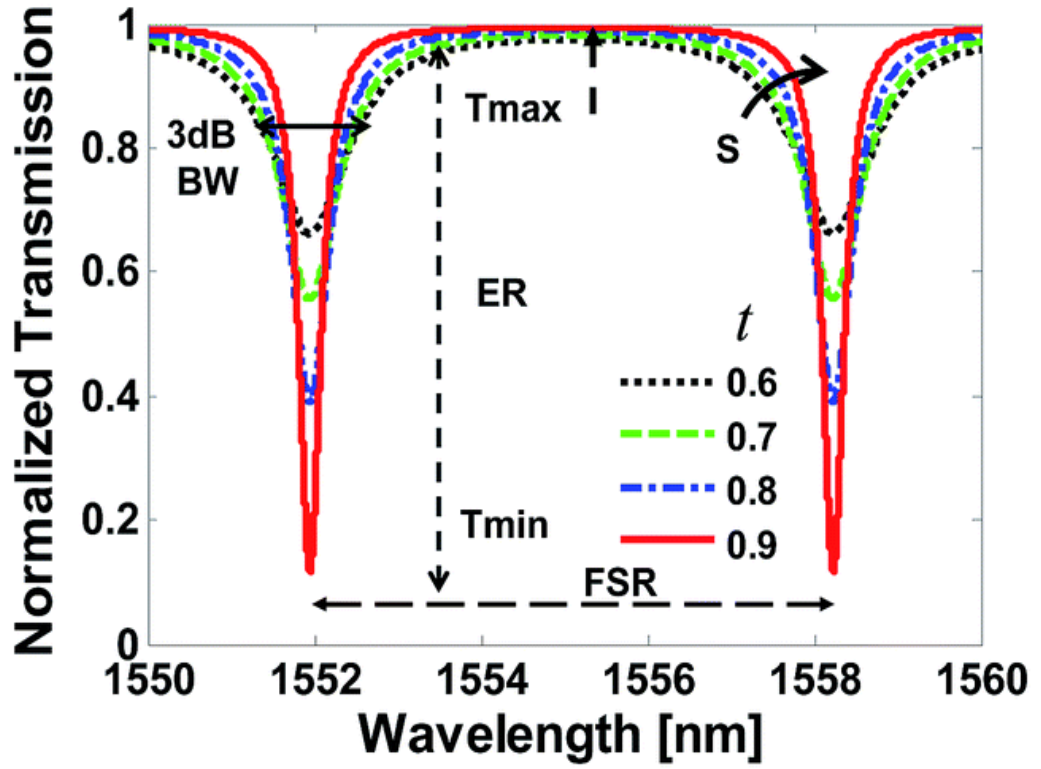


Figure 2.4 Through port transmission spectra of a ring resonator for different coupling factors [33]

In the case of the add/drop waveguide coupled to the ring as shown in Fig 2.2, the transmitted signal in the through port will be given by Eq 2.11 [35, 36, 42]:

$$|E_{t1}|^2 = \frac{-t_1^2 + t_2^2 \cdot \tau - 2 \cdot t_1 \cdot t_2 \cdot \tau \cdot \cos(\phi)}{1 + t_1^2 \cdot t_2^2 \cdot \tau - 2 t_1 \cdot t_2 \cdot \tau \cdot \cos(\phi)} \quad (2.11)$$

The through port and drop port transmission spectra are shown in Fig 2.5. The relative intensity or output power at the drop port is given by Eq 2.12 [42]:

$$|E_{t2}|^2 = \frac{k_1^2 \cdot k_2^2 \cdot \tau}{1 + t_1^2 \cdot t_2^2 \cdot \tau - 2 t_1 \cdot t_2 \cdot \tau \cdot \cos(\phi)} \quad (2.12)$$

Where  $t_1 = \sqrt{1 - K_1^2}$ ,  $t_2 = \sqrt{1 - K_2^2}$ , and  $\phi = \frac{(4 \cdot \pi^2 \cdot r \cdot n)}{\lambda}$

With  $t_1$  and  $t_2$  the field transmission factors and  $K_1$  and  $K_2$  the field coupling factors to the waveguides, which depends on the coupling efficiency of the ring resonator

structure,  $\tau$  is the attenuation of the field per round trip for a cavity with attenuation constant  $\alpha$  [36].

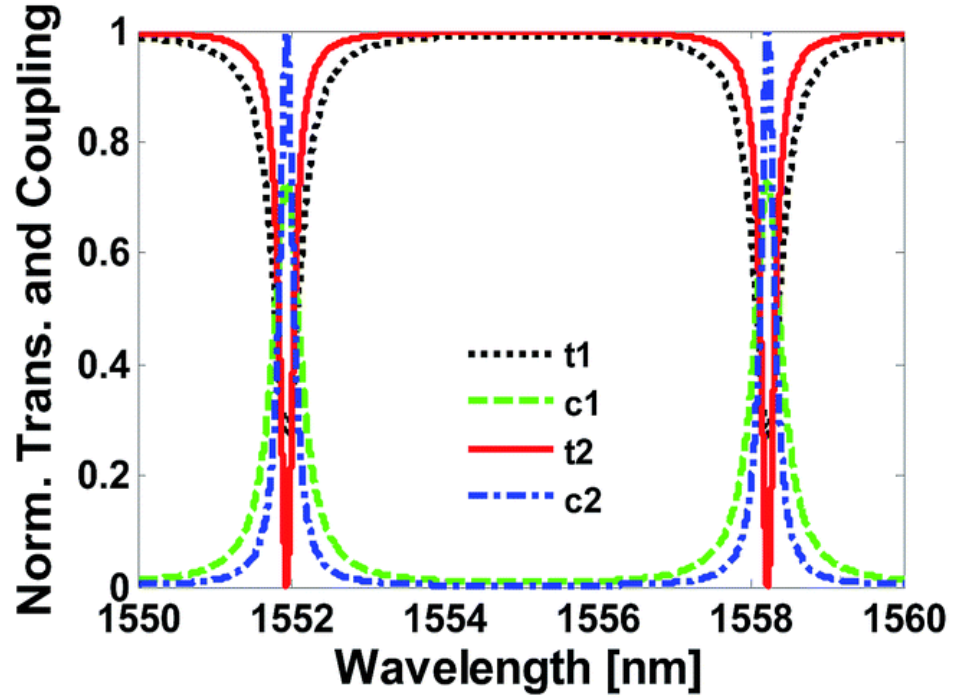


**Figure 2.5** Through and drop port transmission spectra of the add/drop ring resonator, where red and black spectra represent intensity of through port and blue and green spectra the drop port for different coupling and transmission factors [33].

## 2.4 Spectral characteristics

The ‘quality’ of the resonator for optical bio-sensors can be characterized by several factors. For a high performance sensor, the relevant criteria are high quality factor  $Q$ , wide free spectral range (FSR) (spectral separation of resonances), large finesse and large extinction ratio (ER). The major physical characteristics are the size of the ring, the propagation loss, and the input and output coupling ratios [34,43].

### 2.4.1. Quality factor $Q$

The quality factor is the most significant parameter that affects the performance of SOI ring resonator. The quality factor characterizes wavelength selectivity of the resonator; it is defined by the ratio of the central resonant wavelength to the resonator 3dB bandwidth, or full width at half maximum (FWHM). It is a dimensionless parameter that refers to how under-damped a resonator is. Another way of stating the relevance of the  $Q$ -factor is that it is equal to the number of round trips made by the energy in the

ring resonator before being completely dissipated through losses [35,44]. In biochemical applications, high quality factor MRRs allow for the determination of extremely small resonance shifts, which translates to a high sensitivity to changes in effective refractive index. Theoretical and experimental analysis have shown the high sensing performance of MRRs in label-free detection of several chemical and biological analytes, such as RI detection of nucleic acid sequences [45] and proteins [41,42]. The MRRs used in such sensors typically exhibit Q-factors in the range  $10^4$  to  $10^6$ , owing to very low surface roughness (reduced scattering losses) achievable with CMOS foundry manufacture [37,43,46].

#### 2.4.2. Free spectral range (FSR)

The free spectral range is the wavelength spacing between two adjacent resonances and is expressed as:

$$FSR = \frac{\lambda^2}{L * n_g} \quad (2.13)$$

Where  $n_g$  is the group index and  $L$  is the length of the ring resonator round trip. The strong confinement in SOI waveguides permits very sharp bends, offering small features by reducing the ring radius (even down to  $3\mu\text{m}$ ) with still relatively low bend losses. This permits practical increases in the FSR of SOI ring resonators as compared to conventional optical (e.g. fibre) resonators [34].

#### 2.4.3. Finesse (F)

The finesse is the ratio of free spectral range to the width of the resonance. Hence, it is a measure of the resonance ‘sharpness’ relative to their spacing [34].

$$F = \frac{FSR}{FWHM} \quad (2.14)$$

#### 2.4.4. Extinction ratio (ER)

The extinction ratio is defined as the ratio of the transmitted signal intensity ON and OFF resonance [34]:

$$ER = \frac{E_{Max}}{E_{Min}} \quad (2.15)$$

## 2.5. Losses in a silicon ring resonators

In a silicon ring resonator, the losses are due mainly to two effects: waveguide propagation/scattering, bend losses, and the losses incurred at the coupling sections. Waveguide propagation losses arise from different sources, and recent advances in process technology have reduced these in silicon strip waveguides down to below 3dB/cm. Generally, the loss in silicon ring resonators limits their performance [34].

## 2.6. Waveguide geometry of ring resonator based biosensors

Photonic bio-chemical sensors based on MRRs must be configured to achieve the maximum sensitivity. As such, different types of waveguide have been employed by research groups active in the field; these are wire, rib and slot waveguides as described below.

### 2.6.1. Photonic wire waveguides

This structure is commonly employed to construct functional photonic cavity resonators due to simplicity, compatibility with the silicon electronics, and high performance in most materials. The wire waveguide cross section is illustrated by a rectangular geometrical shape as shown in Fig 2.6 [47]. It is constructed in a high refractive index core to confine the optical field. For the case when a high contrast material is used such as SOI platform, light will be strongly confined inside the core layer and the light can be guided with very little propagation/bend losses (even for very small bend radii). As such, one can fabricate ultra-small geometrical designs (typically on the order of  $100\mu\text{m}^2$ )[48].

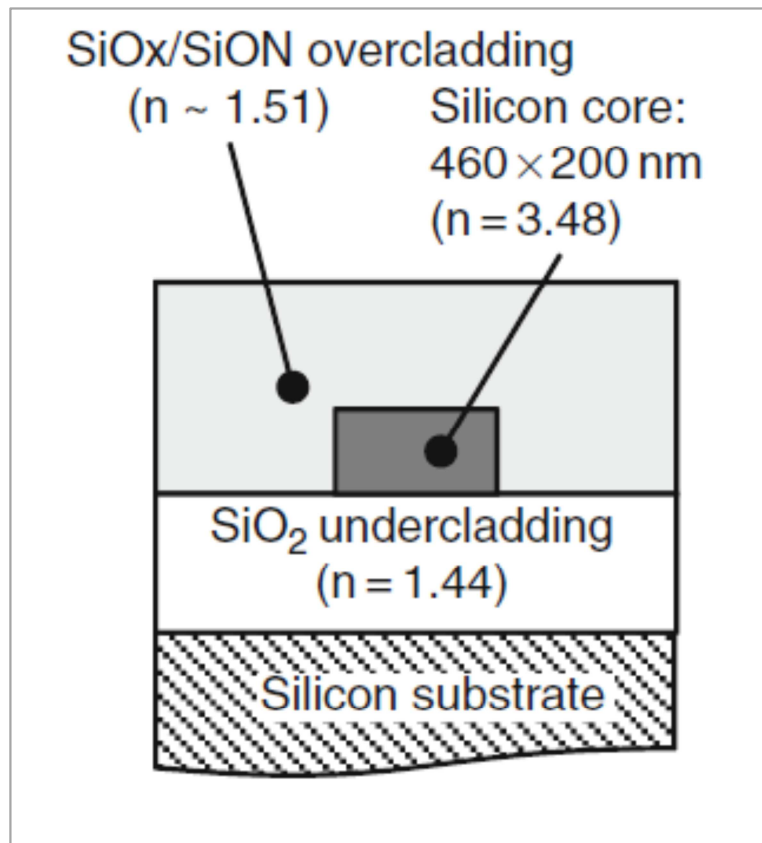


**Figure 2.6 Schematic of the cross-section of a wire waveguide [47]**

De Vos et al [49] reported the use of wire waveguide based racetrack resonators for measuring the refractive index of saline with different salt concentrations. They achieved a bulk sensitivity, from calculations using the parameters  $r = 5\mu\text{m}$ ,  $\lambda = 1550\text{nm}$  of approximately  $70\text{ nm/RIU}$  with a detection limit of  $10^{-5}\text{ RIU}$ . Additionally, they used strong affinity avidin/biotin receptors to demonstrate bio-sensing experiments with an estimated protein concentration down to  $10\text{ng/ml}$ .

### **2.6.2. Photonic Rib waveguides**

The second important waveguide structure is the rib waveguide, sometimes called the stripe or ridge waveguide as shown in Fig 2.7. In this architecture, the optical path is defined by partially etching into the core part of the waveguide, leaving beneath it a planar layer of the high index medium. In this waveguide structure the large fraction of the electromagnetic wave is distributed in the planar layer, beneath the waveguide, which increases losses. As the light-matter interaction for the rib waveguide is lower compared to wire waveguides they are generally not well suitable for biological sensing.

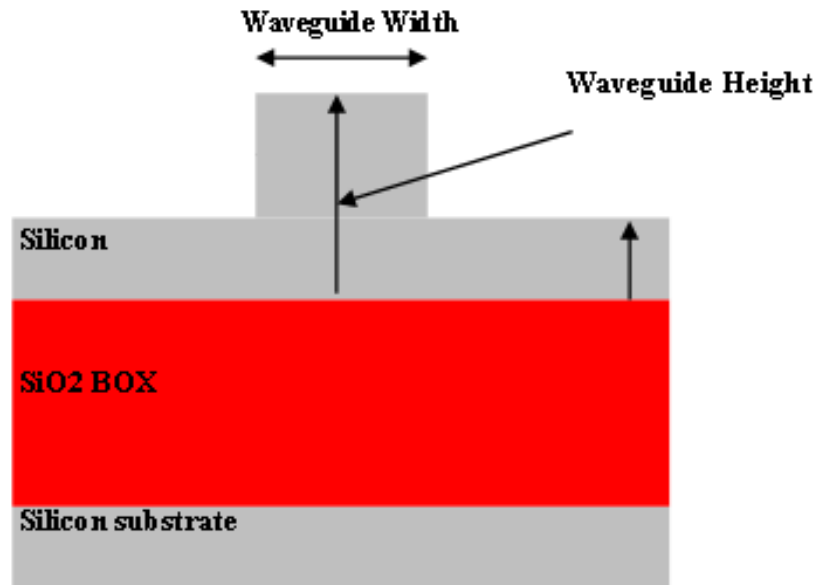


**Figure 2.7 Shows cross section of rib waveguide type**

Whilst very few experimental results for rib waveguide based sensing can be found in the literature, one modelled example was reported by Passaro et al [50], based on simulation of a dye doped PMMA coated waveguide for ammonia sensing, with predicted minimum measurable refractive index change as low as  $8 \times 10^{-5}$ .

### **2.6.3. Photonic Slot waveguides**

The Slot-waveguide is a strip waveguide, modified by introducing a narrow slot between along the central axis of the core as shown in figure 2.8 [51,52]. It differs from the two previous waveguides in that, for the wire and rib configurations, light is confined in the high refractive index layer by means of total internal reflection, while for the slot waveguide the light is confined exceptionally in the narrow, low index, slot region. An advantage of this configuration is that a strong light-analyte interaction in the slot region can be obtained. However, because of the small size of the slot section (generally sub-100nm); a high tolerance in the fabrication is required for repeatable structures. Furthermore, the high optical wave intensity in the slot section makes this waveguide more sensitive to surface roughness, which can result in higher propagation/scattering losses that affect the device performance.



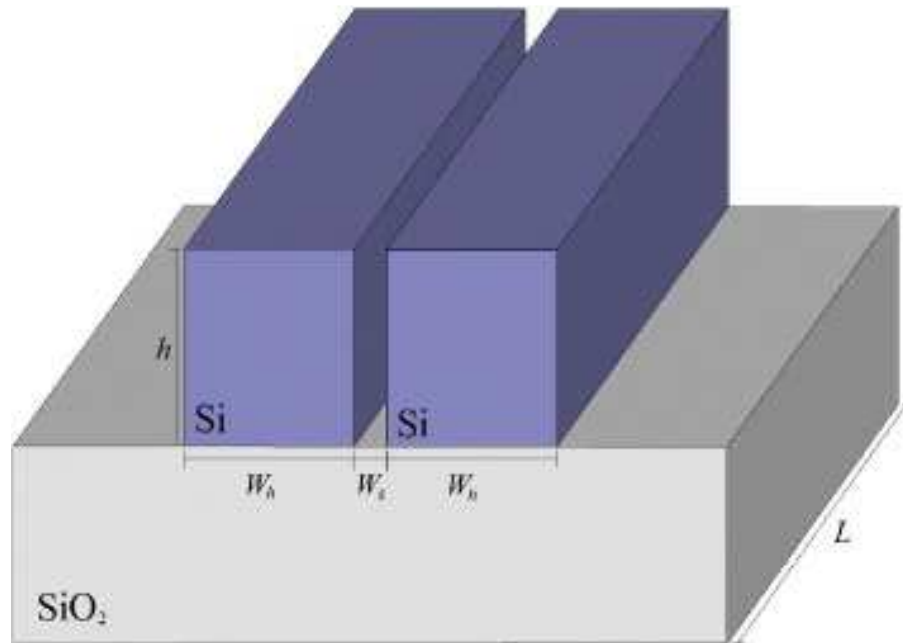


**Figure 2.8 Schematic of a slot waveguide [51,52]**

Silicon slot waveguides have emerged as an attractive solution for sensitive optical biosensors and there have been several reports demonstrating their advantages in biochemical sensing applications [31,32,53]. For example, in [31] a sensing device based on a silicon nitride ( $Si_3N_4$ ) asymmetrical slot waveguide was described as shown in Fig 2.9. For this device configured as a sensor, they reported a value of 212nm/RIU and a detection limit of  $2.3 \times 10^{-4}$  RIU. More recently authors in [53] presented a slot waveguide based ring resonator in (SOI) with sensitivity and detection limit 298nm/RIU and  $4.2 \times 10^{-5}$  RIU, respectively for top cladding refractive index changes. The surface chemistry used for selective label-free sensing of proteins applied inside the slot section reportedly increased the sensitivity by a factor of 3.5 [53]. Further work has also been conducted by Barrios et al [32] in which they showed sensitivity and mass detection limit of 1.8nm/(ng/mm<sup>2</sup>) and 28pg, respectively for anti-BSA detection, whilst the sensitivity and detection limit for BSA was 3.2nm/(ng/mm<sup>2</sup>) and 16pg, respectively.

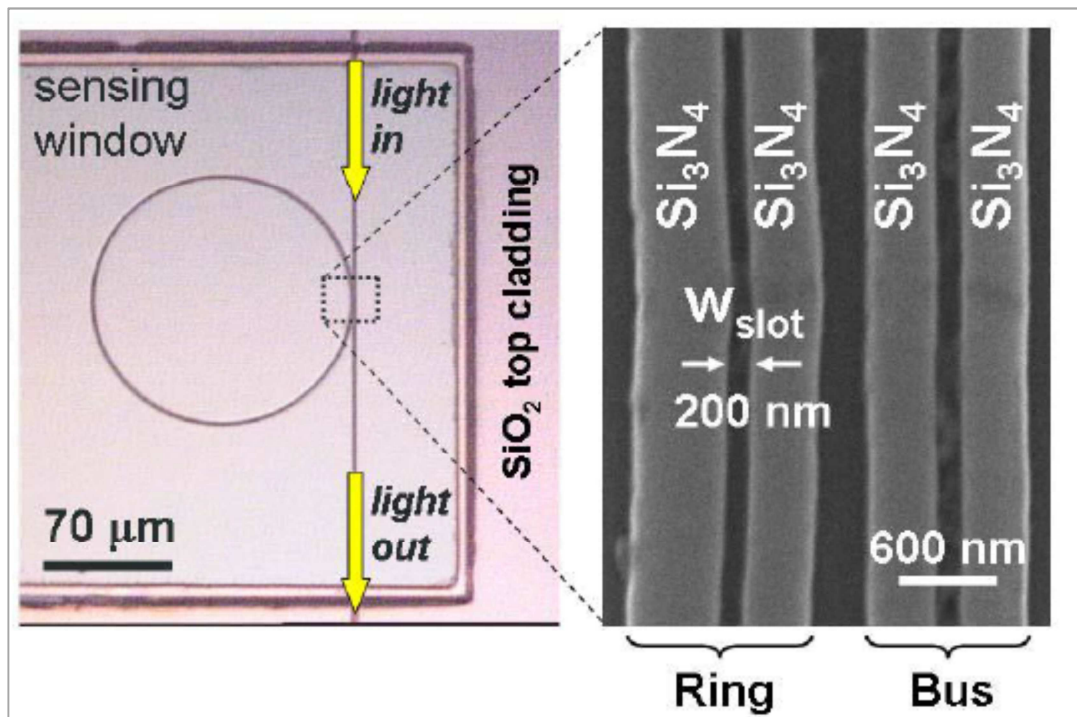


Figure 2.9 Shows image of a slot-based MRR in  $\text{Si}_3\text{N}_4$  used by Barrios et al for the biochemical sensing [28]

From this performance summary, we can conclude that:-

- The wire waveguide based cavity resonator has good general characteristics, ease of fabrication and reasonably high sensitivity with acceptable propagation losses making them the preferred choice for waveguide based bio-chemical sensing.
- The rib waveguide configuration provides for ultimately lower propagation losses than the wire waveguide, although their sensitivity may be significantly overtaken by other two waveguide structures.
- The slot waveguides show high performance achieved by the strong light interaction with the presence of the target analytes sited in the slot region, although this can lead to relatively high propagation loss and fabrication precision required is challenging.

## 2.7. Coupling light into/out of the waveguide

Owing to the large refractive index contrast between the top silicon layer and its buried oxide layer, propagation modes of light can be highly confined within the waveguide structure, with cross-section dimensions on the order of a few hundred nanometres. However, the small cross section of the waveguide raises the problem of huge mode mismatch when coupling light from e.g. single mode fibre to the sub-micron silicon waveguide core.

One of the earliest methods was to use prism coupling, as commonly used to couple light to optical microsphere resonators [54]. Also tapered fibres are used to achieve the required phase matching between a fibre and a cavity mode [55].

The two common approaches that are used to address the mode mismatch problem for coupling to waveguides and MRRs are horizontal (butt) coupling and vertical coupling (via gratings) [56-58], both having distinct advantages and disadvantages. The butt coupling technique has the advantages of being able to couple a larger bandwidth (hundreds of nm) with low coupling loss [58] and fewer fabrication steps. On the other hand, it suffers from low fabrication tolerance errors in defining gap separation as well as complexity in aligning specialised (lensed) input/output fibres.

The vertical coupling technique offers a much simplified alignment tolerance (i.e. appropriate for fast measurement) and does not require the use of lensed or high numerical aperture fibres for delivery/collection of the light. However, whilst coupling efficiency is typically better than 30%, grating couplers have only a limited bandwidth (tens of nm), as well as a high polarization selectivity. The latter is the result of the raised birefringence of high index contrast grating structures, the effective index of the periodic modulation is significantly different for each polarization, leading to a different Bragg condition for TE and TM [56-58].

## 2.8. Waveguide sensing materials

Besides silicon, silicon nitride ( $\text{Si}_3\text{N}_4$ ) based platforms are another material with great potential for the development of bio-chemical sensing based on waveguide structures such as MRRs. In this case the lower refractive index contrast permits more of the evanescent wave to interact with the analyte to be detected, although this is traded with larger device footprints, they can have lower losses and operation can be

extended to shorter (visible) wavelengths. Generally,  $\text{Si}_3\text{N}_4$  has higher sensitivity than SOI technology. Stutius et al [59] have shown that the  $\text{Si}_3\text{N}_4$  with a buried oxide layer fabricated on silicon wafers provide waveguides with very low attenuation, less than 0.1dB/cm for TE mode at 632.8 nm wavelength. However, one of the main drawbacks is the higher losses to the silicon substrate from bending; limiting the smallest radii of cavities structure and potential device feature density as a result.

Polymer waveguide based MRRs have also been considered for bio-chemical sensing. Sun et al [60] reported an integrated optical sensor based on multi-slot waveguides fabricated in polymer, exhibiting improved sensitivity. Mancuso et al [61] reported an integrated porous polymer MRR based biosensor showing an enhancement of the polymer device sensitivity by 40% which they attributed to the interactions of the specific bio-analyte with the optical field. However, whilst these are simple (and inexpensive) to fabricate as well as being bio-compatible, they tend to exhibit very high optical losses and can only be realised as much larger size structures (large bending radii) due to poor index contrast between the polymer waveguide core and cladding, making them ultimately uncompetitive in most performance metrics.

## **2.9. Optical ring resonator based sensor performance metrics**

To compare different kinds of optical MRR based sensors, it is necessary to define some performance metrics. The suitability of optical sensors for a particular application will depend on their performance across number of sensor requirements. Some metrics such as sensitivity, and cost, can be defined numerically (either by means of experimental or theoretical calculations). Other metrics such as portability is more subjective or simply comparable but can have a significant influence on the commercial success of the methods. In this section a number of metrics that are typically considered to determine the performance of SOI MRR based bio-chemical sensors are briefly discussed.

### **2.9.1. Sensitivity**

In sensor development, sensitivity ( $S$ ) represents a fundamental parameter for quantifying the sensor performance. In particular, sensitivity is determined by the strength of the light-matter interaction; therefore, the sensitivity of an optical sensor is

governed by the magnitude of the sensor output signal change in response to a variation of analyte coverage on the sensor surface [62]. The sensitivity of optical sensors depends on many factors such as the recognition layer or penetration depth of evanescent field, the fluidic structure, the affinity of the molecules, device thickness, length and the diameter of the core.

The design goal for achieving high sensitivity is to produce a structure that allows as much of the evanescent field as possible to reside outside the transducer and within the surrounding media, without trading too much propagation loss. Sensitivity is defined as the ratio of the change in transducing optical parameters ( $\Delta\lambda$  in the resonant wavelength interrogation shift scheme or  $\Delta I$  in the intensity interrogation scheme) induced by the change of the background effective refractive index ( $\Delta n_{eff}$ ), caused by the analyte binding, as given in units of nm/RIU (refractive index unit), as:

$$S = \frac{\Delta\lambda}{\Delta n_{eff}} \quad (2.16)$$

And for intensity interrogation schemes this becomes:

$$S = \frac{\Delta I}{\Delta n_{eff}} \quad (2.17)$$

Sensitivity can be divided into two types; device sensitivity and waveguide sensitivity. In practice, the sensitivity of the device is defined by the wavelength shift per unit concentration of an analyte, being higher the larger the induced wavelength shift for a given effective refractive index change. For cavity resonator devices operating at different wavelengths, we can define a normalized sensitivity to enable comparisons:

$$S' = \frac{S}{\lambda} = \frac{\Delta\lambda}{\lambda \Delta n_{eff}} \quad (2.18)$$

Waveguide sensitivity is determined by the effective index change that yielded either by a refractive index variation of the cover medium or by thickness variation of sensing layer which the is bound to the waveguide surface [29,63,64]. It differs with the sensing mechanism whether homogeneous or surface sensing and expressed as[64].

$$S_H = \frac{\Delta\lambda}{\Delta n_c}$$

$$S_S = \frac{\Delta\lambda}{\Delta t_s}$$

$S_H$  represents homogeneous and  $S_S$  is surface sensing,  $\Delta n_c$  is change in cladding index,  $\Delta t_s$  change in add layer and  $\Delta\lambda$  change in resonance wavelength

### 2.9.2. Selectivity

Selectivity is a measure of how specific the response of a sensor is to the target molecule. This typically relies on having an appropriate surface coating of the transducer, which can selectively bind to the target analyte, thus reducing the background (false) signals. However, the use of certain generic functional layers, for example those for which it is possible to control porosity (pore size and network) may offer a simpler route to selectivity based on molecular size. Alternatively, materials of a specific pH (say, more acid) may be used for selective detection of materials, including gases, that are less acidic[50].

### 2.9.3. Resolution

Resolution defines the smallest change in output signal or lowest target analyte concentration that can be detected. It depends on many factors such as transducer type, noise level, read-out system, and data processing. The resolution of a sensor platform is determined by characterization of the sensor noise when operated with its sensing system. An estimate of the noise can be characterized by allowing the sensor to reach some steady-state before exposure to the target. This allows quantitative assessment of e.g. temperature variation or effects of carrier gas or liquid to be accounted for.

### 2.9.4. Limit of Detection (LOD)

The LOD is another figure of merit for a sensor platform, defined as the minimum detectable analyte concentration e.g. amount by mass of the analyte detectable by the sensor. It depends on many factors such as surface chemistry, affinity of the analyte, and sample delivery etc. It can be expressed in different units; typically RIU for bulk

refractive index change, or in ng/ml for analyte concentration, or g for total molecular mass. The LOD as defined by the smallest resolvable signal is given by[65]:

$$LOD = \frac{3.3 \cdot \sigma}{S} \quad (2.19)$$

Where  $\sigma$  is the output uncertainty and  $S$  is the sensitivity, indicating improvement in the LOD can be achieved either by increasing the sensitivity or decreasing the system noise (or both). The LOD of MRR based photonic biosensors refers to the smallest change of the refractive index analyte leading to a detectable shift of the cavity resonance wavelength. The lowest detectable shift is governed by the line-width of the laser used to generate the optical signal as well as detector resolution although the MRR Q-factor generally translates to smaller (better) LOD.

#### **2.9.5. Dynamic range**

The dynamic range is defined as the ratio of the largest measurable concentration of sensing events to the LOD. In cavity resonator based sensing it is determined by the free spectral range (FSR) of the cavity, and also by the signal transduction mechanism employed. The FSR is the largest measurable shift that can be measured and thus a maximum detectable concentration for a sensing event. Therefore, cavities with smaller radii, which have larger FSR, offer the largest dynamic range. Other factors can limit the practical dynamic range of such sensors though, such as chemical functionalization of the sensor surface, i.e. absolute concentration of binding sites available, which if small may be saturated for wavelength shifts smaller than the FSR [62].

#### **2.9.6. System noise**

In any measurement system, noise is defined as signal variation in a static measurement. The signal noise is characterized as the standard deviation ( $\sigma$ ) of the steady state signal. In addition to instrumental [66] and laser noise sources (relative intensity noise, RIN [67]), MRR based sensors are especially susceptible to thermal variations as a result of the temperature dependent refractive index as well as any contaminants in ambient conditions such as water molecules in the air. Therefore, it is necessary to make assessment of these when determining figures of merit such as the

LOD and sensitivity. The thermal induced wavelength noise can be reduced to some extent by employing a temperature control such as a thermoelectric cooler to achieve thermal stabilization of the sensor device or by balancing the thermo-optic coefficient by combining the MRR with a material having opposite thermal response to that of silicon and this is the subject of on-going research[68].

### **2.9.7. Cost**

The cost of the sensor system is comprised of the silicon photonics platform itself plus any ancillary costs e.g. the light source and instrumentation costs. Typically, the source (laser) and detector costs are relatively expensive owing to their complexity and much of the current research is looking at ways in which these may be integrated with the silicon photonics platform. On the detector side, this should be achievable in a mass-scalable approach combining the photonics sensor with silicon CMOS, either via single channel detector integration (e.g. using Si, Ge, SiGe photodiodes) [69,70] or via dispersive detection of signals (e.g. using arrayed waveguide grating (AWG) technologies)[71,72]. Again these are the subject of on-going research. Integration of the light source is more complicated (and therefore likely the most costly aspect for scale-up), as this will likely require post Si process integration of III-V laser chips. Whilst efforts are underway to realise this in a cost effective way, either by bonding of III-V chips to Si [73,74] or direct growth of III-V on Si[73,75], no single solution has yet emerged. The sensors themselves however can be fabricated for parallel analysis of different samples on the same platform using mass-scaled Si-based materials and process, such that costs can be acceptably low so as to make them disposable [62].

Reusable sensors are beneficial in applications where detailed sensor calibration is required with extreme precision, particularly in areas relating continuous monitoring. Whereas one shot sensors type are useful in applications where disposable and cost-effective are required. Reusable sensor chip technology holds the key to more accurate sensing, and diagnosis of diseases. However, some target analyte such as antibodies-antigens presents some limitations such as no catalytic effect is seen, so they can be used only one-time before disposal, like labelled samples [62]. Optical silicon MRR sensors technology could be easily modified to monitor a several type of biomarkers. It is possible to detect chemical concentration levels by immobilizing bio-receptors target on the surface such as creatinine and glucose, in a re-usable way, or any specific



biomolecules functionalised on the surface can be targeted as a one time-use type testing.

### **2.9.8. Portability**

Portability is a subjective characteristic for sensing platforms that determine the possibility to transport the sensing sample to wide range of locations to perform in-situ measurements, and in time restricted settings where a rapid response is required for chemicals sensing applications [62]. Deployment on aircraft might be an example of where lightweight, miniaturised samples could be of benefit, e.g. for atmospheric gas sensing, or even deployment as a health-care monitoring platform to inaccessible geographical locations.

### **2.8.9. Response time/Recovery time**

Response time is defined as time to reach 90% of steady state response of e.g. resonance shift in MRR based sensor when exposed to a target liquid/analyte/vapour/gas. Fast detection is normally considered an important performance metric in sensing applications as it enables large throughput. Response time may be limited by chemical reaction rates and sensor device coverage area. Functional porous films with large surface area will generally provide improved response rates although there can be hysteresis in the rates of adsorption-desorption.

### **2.10. Surface functionalization of silicon photonic chips for bio-chemical sensing**

As was presented in the previous sections, evanescent field biological, and gas sensors have the ability to measure refractive index changes in the sensing region as result of small shifts in resonant wavelength or intensity variation at a specific wavelength. Optical chemical sensors employ this kind of mechanism in order to detect the presence of target molecules on the surface of device. However, these devices cannot often distinguish between the adsorption of particular molecules from contaminants in the background carrier gas or ambient. To provide such a characteristic to an optical photonic sensor, surface chemical functionalization is typically used to attach ‘proper’ receptors to the surface, which exhibit preferential binding to the target molecules to be detected [76].

One of the main challenges in developing a silicon biosensor device is modifying the surface reactivity. To date, numerous studies have been conducted on the functionalization of silicon MRRs. For instance, Park et al [46] demonstrated the detection of single-stranded DNA by peptide nucleic acid functionalization. Ciminelli et al [77] demonstrated glucose oxidase functionalization on SOI MRRs for glucose detection and Ramachandran et al [15] reported MRR surface functionalization using antibodies for whole cell/antigen detection and nucleic acid probes for nucleic acid hybridized detection. Iqbal et al [78] reported biotin functionalization on silicon MRRs for streptavidin detection and Yeh Chen et al [79] proposed a route to surface modification based on functionalized poly-p-xylylene coatings, to improve reactivity more generally. These surface functional layers tend to be relatively thick, however (on the mm-scale) which may not be ideal for evanescent field based detection methods. Rather, for improved field interaction, it is essential that the analytes be located as near to the Si MRR sensing surface as possible and therefore relatively thick coatings are undesirable.

Beyond bio-sensing, novel surface chemistry has also been developed for vapour/gas sensing applications, e.g. by integrating large surface area porous structures [80]; ZnO functionalization for ethanol sensing [81], WO<sub>3</sub> functionalization [14] and nonporous alumina-silicate functionalization for discriminating between ammonia and CO<sub>2</sub> in exhaled breath [82] have all been reported. Polymer surface coating on a fused silica resonator for vapour sensing [48], a poly(ethylene glycol) (PEG)-1000 coating of an opto-fluidic MRR for detection of explosive DNT vapours [83] and a silicon nitride MRR functionalized with a triphenylene-ketal receptor/cladding layer for reversible and selective TNT vapour detection [84], were also described.

## 2.10. References

1. Cunningham, B.T., *Label-free optical biosensors: An introduction*. Label-Free Biosensors: Techniques and Applications, 2009. **1**.
2. Blair, S. and Y. Chen, *Resonant-enhanced evanescent-wave fluorescence biosensing with cylindrical optical cavities*. Applied Optics, 2001. **40**(4): p. 570-582.
3. Aparicio, F., et al., *Silicon oxynitride waveguides as evanescent-field-based fluorescent biosensors*. Journal of Physics D: Applied Physics, 2014. **47**(40): p. 405401.
4. Kneipp, K., et al., *Ultrasensitive chemical analysis by Raman spectroscopy*. Chemical reviews, 1999. **99**(10): p. 2957-2976.
5. Liu, K., et al., *Wavelength sweep of intracavity fiber laser for low concentration gas detection*. IEEE Photonics Technology Letters, 2008. **20**(18): p. 1515-1517.
6. Cui, X., et al., *Photonic sensing of the atmosphere by absorption spectroscopy*. Journal of Quantitative Spectroscopy and Radiative Transfer, 2012. **113**(11): p. 1300-1316.
7. Densmore, A., et al., *A silicon-on-insulator photonic wire based evanescent field sensor*. IEEE Photonics Technology Letters, 2006. **18**(23): p. 2520-2522.
8. Zhang, Y. *Silicon on Insulator photonic wire based evanescent field multi-channelled biosensor array "Lab on a Chip" devices*. in *Functional Optical Imaging (FOI)*, 2011. 2011. IEEE.
9. Fan, X., et al., *Sensitive optical biosensors for unlabeled targets: A review*. analytica chimica acta, 2008. **620**(1): p. 8-26.
10. Guo, Q., et al., *Silicon-on-glass graphene-functionalized leaky cavity mode nanophotonic biosensor*. Acs Photonics, 2014. **1**(3): p. 221-227.
11. Georgakilas, V., et al., *Functionalization of graphene: covalent and non-covalent approaches, derivatives and applications*. Chem. Rev, 2012. **112**(11): p. 6156-6214.
12. De Vos, K., et al., *Multiplexed antibody detection with an array of silicon-on-insulator microring resonators*. IEEE Photonics journal, 2009. **1**(4): p. 225-235.
13. De Vosa, K., et al. *Multiplexed protein detection with an array of silicon-on-insulator microring resonators*. in *LEOS Annual Meeting Conference Proceedings, 2009. LEOS'09. IEEE*. 2009. IEEE.
14. Yebo, N.A., et al., *Silicon-on-insulator (SOI) ring resonator-based integrated optical hydrogen sensor*. IEEE Photonics Technology Letters, 2009. **21**(14): p. 960-962.
15. Ramachandran, A., et al., *A universal biosensing platform based on optical micro-ring resonators*. Biosensors and Bioelectronics, 2008. **23**(7): p. 939-944.
16. Cho, H.K. and J. Han, *Numerical study of opto-fluidic ring resonators for biosensor applications*. Sensors, 2012. **12**(10): p. 14144-14157.
17. Passaro, V., et al., *Recent advances in integrated photonic sensors*. Sensors, 2012. **12**(11): p. 15558-15598.
18. Wikipedia, t.f.e. *Evanescent field*. 2016 [cited 2016 05/08]; Available from: [https://en.wikipedia.org/wiki/Main\\_Page](https://en.wikipedia.org/wiki/Main_Page).
19. Janz, S., *Food and Water Safety-Silicon photonic wire waveguide sensors detect the presence of pathogens and chemicals*. Photonics Spectra, 2008. **42**(3): p. 55.

20. Fan, X., *Advanced photonic structures for biological and chemical detection*. 2009: Springer.
21. Xhoxhi, M., A. Dudia, and A. Ymeti, *Interferometric Evanescent Wave Biosensor Principles and Parameters*.
22. Lechuga, L.M., et al., *Biosensing microsystems: fast, label-free, real-time clinical testing*. 2008.
23. Luchansky, M.S., et al., *Characterization of the evanescent field profile and bound mass sensitivity of a label-free silicon photonic microring resonator biosensing platform*. *Biosensors and Bioelectronics*, 2010. **26**(4): p. 1283-1291.
24. Yin, S.S. and P. Ruffin, *Fiber optic sensors*. 2002: Wiley Online Library.
25. Zourob, M., et al., *Integrated deep-probe optical waveguides for label free bacterial detection*, in *Principles of Bacterial Detection: Biosensors, Recognition Receptors and Microsystems*. 2008, Springer. p. 139-168.
26. Dattner, Y. and O. Yadid-Pecht, *Analysis of the effective refractive index of silicon waveguides through the constructive and destructive interference in a Mach–Zehnder interferometer*. *IEEE Photonics journal*, 2011. **3**(6): p. 1123-1132.
27. Liedberg, B., C. Nylander, and I. Lunström, *Surface plasmon resonance for gas detection and biosensing*. *Sensors and actuators*, 1983. **4**: p. 299-304.
28. Chao, C.-Y. and L.J. Guo, *Design and optimization of microring resonators in biochemical sensing applications*. *Journal of Lightwave Technology*, 2006. **24**(3): p. 1395.
29. Dell’Olio, F. and V.M. Passaro, *Optical sensing by optimized silicon slot waveguides*. *Optics express*, 2007. **15**(8): p. 4977-4993.
30. White, I.M., et al., *Refractometric sensors for lab-on-a-chip based on optical ring resonators*. *IEEE Sensors Journal*, 2007. **7**(1): p. 28-35.
31. Barrios, C.A., et al., *Slot-waveguide biochemical sensor*. *Optics letters*, 2007. **32**(21): p. 3080-3082.
32. Barrios, C.A., et al., *Label-free optical biosensing with slot-waveguides*. *Optics letters*, 2008. **33**(7): p. 708-710.
33. Ahmed, R., et al., *Optical microring resonator based corrosion sensing*. *Rsc Advances*, 2016. **6**(61): p. 56127-56133.
34. Bogaerts, W., et al., *Silicon microring resonators*. *Laser & Photonics Reviews*, 2012. **6**(1): p. 47-73.
35. Rabus, D.G., *Integrated ring resonators*. 2007: Springer.
36. Rabus, D.G., *Ring resonators: Theory and modeling*. *Integrated Ring Resonators: The Compendium*, 2007: p. 3-40.
37. Sun, Y. and X. Fan, *Optical ring resonators for biochemical and chemical sensing*. *Analytical and bioanalytical chemistry*, 2011. **399**(1): p. 205-211.
38. Yariv, A., *Critical coupling and its control in optical waveguide-ring resonator systems*. *IEEE Photonics Technology Letters*, 2002. **14**(4): p. 483-485.
39. Yariv, A., *Universal relations for coupling of optical power between microresonators and dielectric waveguides*. *Electronics letters*, 2000. **36**(4): p. 321-322.
40. Choi, J.M., R.K. Lee, and A. Yariv, *Control of critical coupling in a ring resonator–fiber configuration: application to wavelength-selective switching, modulation, amplification, and oscillation*. *Optics letters*, 2001. **26**(16): p. 1236-1238.
41. Boyd, R.W. and J.E. Heebner, *Sensitive disk resonator photonic biosensor*. *Applied Optics*, 2001. **40**(31): p. 5742-5747.

42. Vorckel, A., et al., *Asymmetrically coupled silicon-on-insulator microring resonators for compact add-drop multiplexers*. IEEE Photonics Technology Letters, 2003. **15**(7): p. 921-923.
43. Xue, C., et al. *Quality factor of silicon-on-insulator Integrated Optical Ring Resonator*. in *SPIE Photonic Devices+ Applications*. 2011. International Society for Optics and Photonics.
44. De Vos, K., et al., *Optical biosensor based on silicon-on-insulator microring cavities for specific protein binding detection-art. no. 64470K*. Nanoscale Imaging, Spectroscopy, Sensing, and Actuation for Biomedical Applications IV, 2007. **6447**: p. 4470.
45. Qavi, A.J., et al., *Anti-DNA: RNA antibodies and silicon photonic microring resonators: increased sensitivity for multiplexed microRNA detection*. Analytical chemistry, 2011. **83**(15): p. 5949-5956.
46. Park, M.K., et al., *Label-free aptamer sensor based on silicon microring resonators*. Sensors and Actuators B: Chemical, 2013. **176**: p. 552-559.
47. Yamada, K., et al. *Silicon photonics based on photonic wire waveguides*. in *OptoElectronics and Communications Conference, 2009. OECC 2009. 14th*. 2009. IEEE.
48. Sun, Y. and X. Fan, *Analysis of ring resonators for chemical vapor sensor development*. Optics express, 2008. **16**(14): p. 10254-10268.
49. De Vos, K., et al., *Silicon-on-Insulator microring resonator for sensitive and label-free biosensing*. Optics express, 2007. **15**(12): p. 7610-7615.
50. Passaro, V., F. Dell'Olio, and F. De Leonadis, *Ammonia optical sensing by microring resonators*. Sensors, 2007. **7**(11): p. 2741-2749.
51. Wikipedia. *Slot-waveguide* 2017 [cited 2017 20/03]; Available from: <https://en.wikipedia.org/wiki/Slot-waveguide>.
52. Radjenović, B., B. Milanović, and M. Radmilović-Radjenović, *Electric field enhancement in silicon slotted optical strip waveguides and microring resonators*. Physica Scripta, 2012. **2012**(T149): p. 014027.
53. Claes, T., et al., *Label-free biosensing with a slot-waveguide-based ring resonator in silicon on insulator*. IEEE Photonics journal, 2009. **1**(3): p. 197-204.
54. Gorodetsky, M. and V. Ilchenko, *High-Q optical whispering-gallery microresonators: precession approach for spherical mode analysis and emission patterns with prism couplers*. Optics Communications, 1994. **113**(1-3): p. 133-143.
55. Gorodetsky, M.L. and V.S. Ilchenko, *Optical microsphere resonators: optimal coupling to high-Q whispering-gallery modes*. JOSA B, 1999. **16**(1): p. 147-154.
56. Melloni, A., *Synthesis of a parallel-coupled ring-resonator filter*. Optics letters, 2001. **26**(12): p. 917-919.
57. Chin, M. and S. Ho, *Design and modeling of waveguide-coupled single-mode microring resonators*. Journal of Lightwave Technology, 1998. **16**(8): p. 1433.
58. Grover, R., et al., *Laterally coupled InP-based single-mode microracetrack notch filter*. IEEE Photonics Technology Letters, 2003. **15**(8): p. 1082-1084.
59. Stutius, W. and W. Streifer, *Silicon nitride films on silicon for optical waveguides*. Applied Optics, 1977. **16**(12): p. 3218-3222.
60. Sun, H., A. Chen, and L.R. Dalton, *Enhanced evanescent confinement in multiple-slot waveguides and its application in biochemical sensing*. IEEE Photonics journal, 2009. **1**(1): p. 48-57.

61. Mancuso, M., J.M. Goddard, and D. Erickson, *Nanoporous polymer ring resonators for biosensing*. Optics express, 2012. **20**(1): p. 245-255.
62. De Vos, K., *Label-Free Silicon Photonics Biosensor Platform with Microring Resonators*, 2010, Ghent University.
63. Schmitt, K. and C. Hoffmann, *High-refractive-index waveguide platforms for chemical and biosensing*, in *Optical Guided-wave Chemical and Biosensors I*. 2010, Springer. p. 21-54.
64. Prieto, F., et al., *Design and analysis of silicon antiresonant reflecting optical waveguides for evanescent field sensor*. Journal of Lightwave Technology, 2000. **18**(7): p. 966.
65. Desimoni, E. and B. Brunetti, *About estimating the limit of detection by the signal to noise approach*. PHARMACEUTICA ANALYTICA ACTA, 2015. **6**(3): p. 1-4.
66. White, I.M. and X. Fan, *On the performance quantification of resonant refractive index sensors*. Optics express, 2008. **16**(2): p. 1020-1028.
67. Zhou, X., L. Zhang, and W. Pang, *Performance and noise analysis of optical microresonator-based biochemical sensors using intensity detection*. Optics express, 2016. **24**(16): p. 18197-18208.
68. Gylfason, K.B., et al., *On-chip temperature compensation in an integrated slot-waveguide ring resonator refractive index sensor array*. Optics express, 2010. **18**(4): p. 3226-3237.
69. Pandraud, G., et al. *Integrated SiGe Detectors for Si Photonic Sensor Platforms*. in *Multidisciplinary Digital Publishing Institute Proceedings*. 2017.
70. Colace, L. and G. Assanto, *Germanium on silicon for near-infrared light sensing*. IEEE Photonics journal, 2009. **1**(2): p. 69-79.
71. Dumon, P., et al. *Compact arrayed waveguide grating devices in Silicon-on-insulator*. in *Proceedings Symposium IEEE/LEOS Benelux Chapter*. 2005.
72. Martens, D., et al., *Compact silicon nitride arrayed waveguide gratings for very near-infrared wavelengths*. IEEE Photon. Technol. Lett, 2015. **27**(2): p. 137-140.
73. Roelkens, G., et al. *III-V-on-silicon photonic devices for optical communication and sensing*. in *Photonics*. 2015. Multidisciplinary Digital Publishing Institute.
74. Wang, R., et al., *III-V-on-Silicon Photonic Integrated Circuits for Spectroscopic Sensing in the 2–4  $\mu\text{m}$  Wavelength Range*. Sensors, 2017. **17**(8): p. 1788.
75. Komljenovic, T., et al., *Heterogeneous silicon photonic integrated circuits*. Journal of Lightwave Technology, 2016. **34**(1): p. 20-35.
76. Rogers, K.R., *Principles of affinity-based biosensors*. Molecular biotechnology, 2000. **14**(2): p. 109-129.
77. Ciminelli, C., et al., *High performance SOI microring resonator for biochemical sensing*. Optics & laser technology, 2014. **59**: p. 60-67.
78. Iqbal, M., et al., *Label-free biosensor arrays based on silicon ring resonators and high-speed optical scanning instrumentation*. IEEE Journal of Selected Topics in Quantum Electronics, 2010. **16**(3): p. 654-661.
79. Chen, H.-Y., et al., *Substrate-independent dip-pen nanolithography based on reactive coatings*. Journal of the American Chemical Society, 2010. **132**(51): p. 18023-18025.
80. Wang, H., et al., *Optical microresonator based on hollow sphere with porous wall for chemical sensing*. Optics letters, 2012. **37**(1): p. 94-96.

81. Yebo, N.A., et al., *An integrated optic ethanol vapor sensor based on a silicon-on-insulator microring resonator coated with a porous ZnO film*. Optics express, 2010. **18**(11): p. 11859-11866.
82. Yebo, N.A., et al., *Selective and reversible ammonia gas detection with nanoporous film functionalized silicon photonic micro-ring resonator*. Optics express, 2012. **20**(11): p. 11855-11862.
83. Sun, Y., et al., *Optofluidic ring resonator sensors for rapid DNT vapor detection*. Analyst, 2009. **134**(7): p. 1386-1391.
84. Orghici, R., et al., *A microring resonator sensor for sensitive detection of 1, 3, 5-trinitrotoluene (TNT)*. Sensors, 2010. **10**(7): p. 6788-6795.





## Chapter 3: Experimental Methods

The different experimental techniques employed in this project are discussed in this chapter. This includes the preparation and deposition methods of sensitization/functional layers (graphene and graphene oxide), and the imaging characterization techniques used to evaluate and assess the uniformity of these deposited layers. Optical spectroscopic techniques employed to probe the transmission spectra of MRR devices under test as well as typical optical techniques such as Raman scattering are described. Also, the development of a bespoke optical and gas handling setup, as employed for characterization of the sensor exposed to some typical organic solvents.

The deposition of graphene and its chemically derived variant, graphene oxide (GO) on silicon were prepared using two different synthesis methodologies. Monolayer graphene was prepared via chemical vapour deposition (CVD), fabricated by Bluestone[4], and transferred to the wafer by a previous research student [1]. For GO, a solution process was prepared and deposited using a spin coating method. The graphene and GO coatings were characterized by scanning electron microscopy (SEM) for morphology, atomic force microscopy (AFM) for film thickness analysis and micro-Raman scattering spectroscopy for determination of the film properties.

### 3.1. Sample details

Before we present the experimental techniques we will give an overview of the silicon photonic circuits used in this thesis, one is based on strip waveguide based racetrack resonators and the other one is slot waveguide based ring resonators as now described:-

#### 3.1.1. Strip waveguide based racetrack resonators

The integrated strip-waveguide racetrack resonator arrays presented in this work were designed by the silicon photonics group at the optics research centre (ORC) at Southampton University and fabricated from commercial 220nm SOI with a 2 $\mu$ m thick buried oxide layer via deep UV (193nm) lithography in a commercial silicon foundry (CEA-LETI, France) [2]. The layout of the photonic chip consists of several racetrack-type MRRs with a fixed waveguide width,  $w=350\text{nm}$  and ring-to-bus coupling gap,  $g=0.3\mu\text{m}$

to ensure good modal overlap with the integrated graphene/GO. The chip contains MRRs with a range of radii of curvature,  $r = 10, 20, 30$  and  $40\mu\text{m}$  and a range of racetrack coupling lengths,  $L_c = 4, 6, 10$  and  $13\mu\text{m}$ .

### **3.1.2. Slot waveguide based ring resonators**

An integrated slot-waveguide cavity resonator array presented in this work was designed by a previous research student in the group, Joseph Lydiate [3]. These were also fabricated from commercial 220nm SOI on a  $2\mu\text{m}$  buried oxide. In this case the waveguides were rib-type with an etch depth of 130nm and slab thickness of 90nm with a waveguide width of 320 nm and a range of ring-to-bus coupling gaps,  $g = 0.2, 0.25$  and  $0.3\mu\text{m}$ . Several circular MRR structures were fabricated with two different radii;  $25\mu\text{m}$  and  $50\mu\text{m}$  and this chip was capped with a  $1.6\mu\text{m}$  oxide layer. For a selection of the MRRs, a window was opened up over part of the ring (using a selective HF etch) to provide access for GO deposition and vapour penetration. Additionally, integrated Titanium Nitride (TiN) heater elements with a thickness of  $0.15\mu\text{m}$  were provided with these devices to enable thermal tuning of the cavity resonances. These are positioned on the top oxide cladding over the ring-bus coupling region with appropriate electrical contact pads.

## **3.2 Synthesis methods**

### **3.2.1 Chemical vapour deposition (CVD)**

Recent developments in the growth of graphene by CVD on copper substrates provides a standard technique for obtaining reasonably high quality material [4]. The graphene can be transferred from the copper onto a silicon test substrate using a wet, polymer mediated process followed by selective removal of the copper and polymer transfer materials. CVD grown graphene was supplied by Gratome-R-Cu, Bluestone Global Tech, as described elsewhere [4]. The procedure used to transfer graphene to the wafer is similar to that developed in references [5,6]. The basic idea is summarised below:-

- The copper foil/CVD graphene is cut to size and flattened by careful pressing
- Next a thick layer of polymer (PMMA 950 8%) is deposited onto the copper foil by spin coating at 3000rpm for 60 seconds.

- The copper is then etched away with dilute ammonium persulfate (APS) (25g in 1000ml of deionized (DI) water). After etching the copper, PMMA/graphene is rinsed with deionized water using a drip and drain setup (10ml/min for 3 hrs.).
- The film is transferred to the sample and dried in air for 1 hour; the sample is then placed in an acetone bath for 10 minutes.
- Finally, the graphene was patterned, to ensure selective coverage of the race-track ring resonators, using raster-scan photolithography and oxygen plasma etching.

### **3.2.2. Spin coating**

The spin coating method provides an easy means to deposit graphene related materials. This technique was adopted for the deposition of sheets of graphene using graphene dispersion in water with a weight concentration of 4mg/ml.

This simple method presents some fundamental advantages in contrast to other coating method such as drop cast ones, the advantages of this method include:

- The synthetic process can be carried out at room conditions and a cheaply synthetic process, for the case of the GO film coating technology.
- Homogeneous coatings on suitable substrates can be made, which can provide improved sensing performance compared with drop cast method.
- The coating thickness of the film can also be easily and precisely controlled

The spin-coating speed and the time used here were 1000 revs/min for 40s; spin coating the GO dispersion solution onto the waveguide substrate can give a uniform structure. The proposed synthesis route in preparing GO films coating waveguide based ring resonators that carried out in this project can be outlined to three stages:

- We prepared different GO concentrations by dissolving commercial GO solution in suitable amounts of deionized water, and the resulting mixtures were sonicated in an ultrasonic bath for 30 min.
- The GO solution was then drop-cast onto the chip using a micropipette and was spin-coated at a substrate speed of 1000 rpm for 30s on the entire chip for each

coating step to cover not only the ring resonators but also the waveguide and grating coupler regions.

- Subsequently, about half an hour of thermal drying time for the GO coatings to obtain the final coating.

### 3.3. Structural characterization techniques

#### 3.3.1. Raman spectroscopy

Raman spectroscopy was used to measure the vibrational, rotational and low frequency modes in molecules and crystal structures via a frequency shift of the scattered photons. Raman spectroscopy inelastically scattered light from matter, this is a process called the Raman effect which was discovered in 1928 by the Indian physicist C. V. Raman [7-9]. The Raman effect arises when a light beam is scattered by molecule and interacts with the electron cloud and the bonds of that molecule: the incident photon excites the molecule into a virtual energy state.

Raman effect can be described by incident radiation interaction of electric field  $E$  with a molecule. The incident electromagnetic field induces a polarization  $P$ , in the material is defined as [28]:

$$P = \alpha \cdot E \quad (3.1)$$

Where,  $\alpha$  is the molecule electric polarization and  $E$  is the electric field corresponding to the incident electromagnetic wave.

A simple description of the Raman scattering phenomenon can be understood using the classical mechanics theory. An electromagnetic wave defined by:

$$E = E_0 \cos(2\pi\nu_0 t) \quad (3.2)$$

Where,  $E_0$  is the complex amplitude and  $\nu_0$  is the frequency of light. Putting  $E$  value in the eq. 3.1, the time dependent induced electric polarization will be:

$$P = \alpha E_0 \cos(2\pi\nu_0 t) \quad (3.3)$$

If a molecule is free to vibrate, and it is not rotate. This molecule is fixed in its equilibrium position, so any disorder in the electronic cloud caused by the electromagnetic wave will cause fluctuation in the molecule polarizability due to

motion of nuclei in the molecules. Thus  $\alpha$  can be expressed by the first order Taylor expansion on the coordinates  $x_i$  of vibration, which is the normal modes of atomic vibrations permitted in a crystalline semiconductor [28]:

$$\alpha = \alpha_0 + \frac{\partial \mu}{\partial x_i} x_i \quad (3.4)$$

$$x_i = x_i^0 \cos(2\pi \nu_i t) \quad (3.5)$$

The combination of the equations 3.4 and 3.5 yields:

$$\alpha = \alpha_0 + \alpha_1 x_i^0 \cos(2\pi \nu_i t) \quad (3.6)$$

Where,  $\alpha_1 = \frac{\partial \mu}{\partial x_i}$ , thus the total polarization of the medium can be expressed as:

$$P = \alpha E_0 \cos(2\pi \nu_0 t) + \alpha_1 E_0 \cos(2\pi \nu_0 t) \cos(2\pi \nu_i t) \quad (3.7)$$

By using the product to sum trigonometric identity,

$$\cos(\theta) \cos(\varphi) = 1/2 \cos(\theta + \varphi) + 1/2 \cos(\theta - \varphi)$$

$$P = \alpha E_0 \cos(2\pi \nu_0 t) + \frac{\alpha_1 x_i^0 E_0}{2} [\cos(\nu_0 + \nu_i) t + \cos(\nu_0 - \nu_i) t] \quad (3.8)$$

As can be seen in equation (3.8), the wave will be scattered by the molecule at three shifted frequencies. The first term is referred to as Rayleigh scattering. The term containing an increase in frequency ( $\nu_0 + \nu_i$ ) is known as anti-Stokes shifted, and the term containing a decrease in frequency of the resulting scattered photon ( $\nu_0 - \nu_i$ ) is known as Stokes shifted.

The diagram has shown in figure 3.1 shows the three different potential outcomes results from this. The first case is when the molecules relax back down to ground state, and the photons scatter elastically, this process is referred to as Rayleigh scattering. The second diagram shows stokes scattering which occurs when the molecules relax to a real phonon state and the scattered radiation loses energy in the process, this occurs very small fraction energy (around 1 in  $10^7$  of incident photons)[10]. The third case is that the molecule is already in an excited vibrational state, it is excited to an upper virtual state, and then relaxes back to the ground state releasing scattering the incident

photon. Here the energy of the scattered photon is higher than the incident one this is called anti-stokes Raman scattering [8-13].

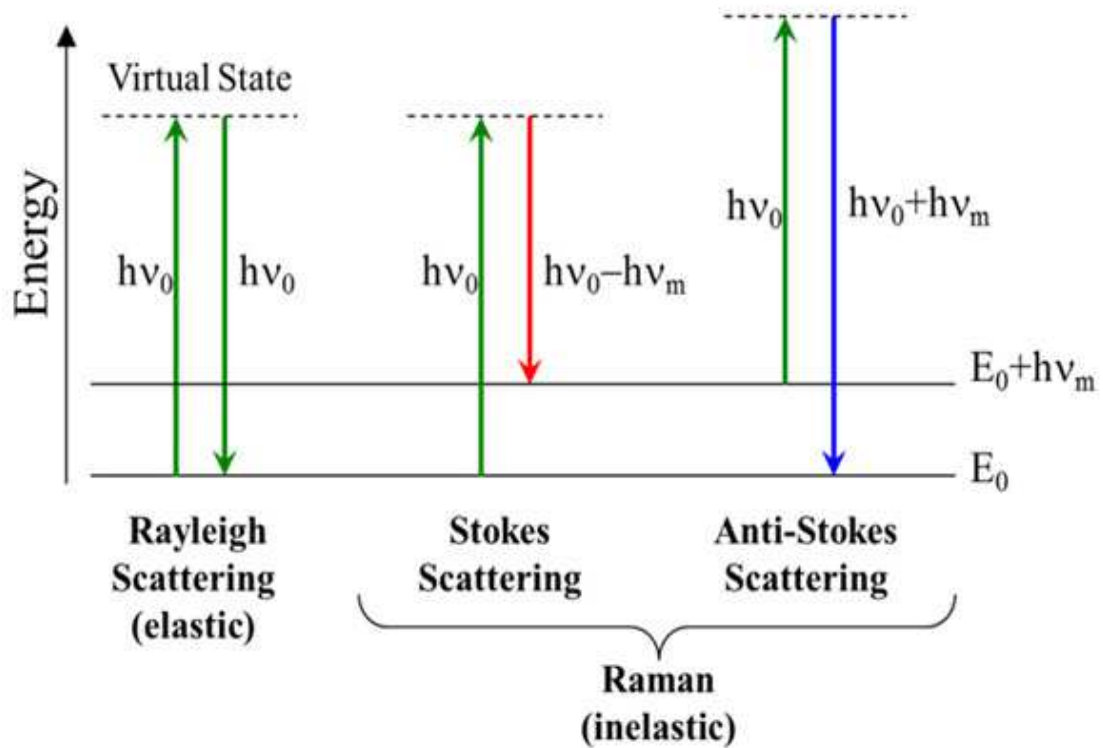


**Figure 3.1** Energy level diagrams showing the states involved in the Raman Effect [13].

Raman spectroscopy is based on the principle of Raman effect using a standard optical microscope/spectrometer to excite the sample and collect the light, a high sensitivity collection system is employed usually using a charge-coupled device (CCD), or photomultiplier tube (PMT)[7]. In this thesis, the instruments used for Raman spectroscopy were a Renishaw in-Via Raman spectrometer and a Horiba Labram spectrometer with different wavelengths of excitation. Both systems collect the light using a microscope and so can detect the Raman scattering from a diffraction limited laser focus. We measured the Raman shift for the CVD graphene coated silicon racetrack resonators and graphene oxide film coated silicon cavity resonators. The data output is collected through the computer using the provided instrument software; all the measurements were performed at room temperature.

The phonon dispersion of the material that we used (silicon and graphene) is important to understand the Raman spectra of both silicon and graphene. Silicon has only one active longitudinal phonon mode LO in first order Raman scattering located at the  $\Gamma$  point in the Brillouin zone centre. The first order Raman spectrum consists of one strong peak position appears at  $520\text{cm}^{-1}$  for silicon/ $\text{SiO}_2$  wafer arising from the triply degenerate optical transverse phonon mode (1LO, 2TO)[30]. Fig.3.2 shows typical Raman spectrum with peak for  $\text{SiO}_2$  /Si wafer.

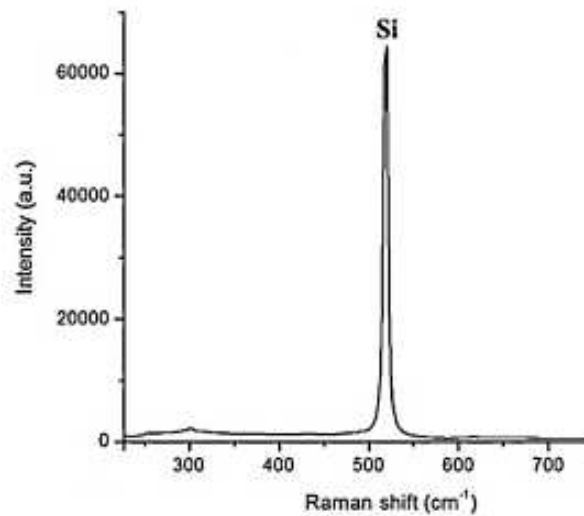


**Figure3.2 a Raman spectrum with peak for Si /  $\text{SiO}_2$  wafer**

As the CVD graphene unit cell contains two carbon atoms, A and B, there are six phonon dispersion curves as shown in Figure.3.3 [28]. Three optical (O) branches and

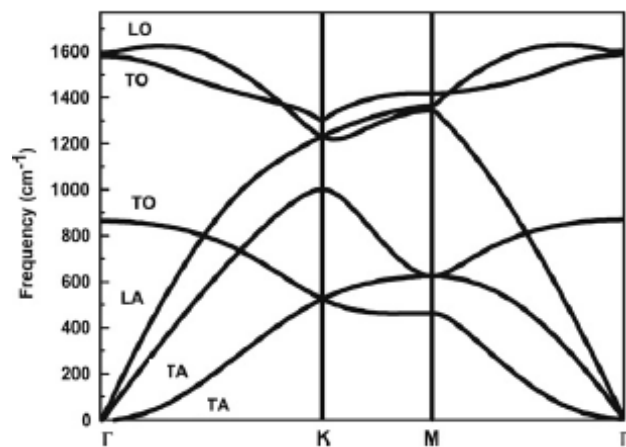


**Figure3.3 Calculated phonon dispersion of graphene showing six phonon branches [29]**

Other three are acoustic (A) branches. For both group one branch, corresponds to the out-of plane (o) phonon modes. The other two branches for each group are one longitudinal (L) and other one is transverse (T), which describe in plane vibration modes. The LO and TO modes near the Brillouin zone centre  $\Gamma$  are degenerate and correspond to the  $E_{2g}$  phonon mode. At the K point, the exact position of the branches is still in debate, especially when it comes to the degeneracy of the LO and TO branches. The Raman active vibration at the K point has  $A_{1g}$  symmetry. Both vibrations will give rise to the 2D peak. The G peak originates from Stokes Raman scattering with one  $E_{2g}$  phonon emission. The D peak is active by double resonance DR, and it associated with graphene defects. It comes from TO branch around the K point of the Brillouin zone, and is strongly dispersive with excitation energy due to a Kohn Anomaly at K point [28, 29]. Fig 3.4 shows typical Raman spectra with peaks for single layer graphene on Si/SiO<sub>2</sub> waveguide.

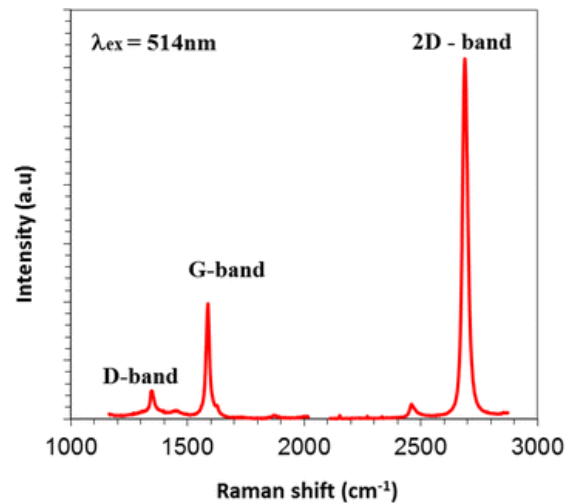


**Figure 3.4 Raman spectra with peaks for single layer graphene on Si waveguide**

### 3.3.2. Atomic force microscopy (AFM)

The most powerful tool for measuring the surface topography at the nanoscale is Atomic force microscopy (AFM). In this study an Atomic force microscopy (AFM) was used to measure the height profile of graphene film surfaces coating samples. AFM works by measuring the interaction forces between the sample surface and fine tipped probe located very close to it. It uses cantilever with the probe on its end that is scanned over the sample surface. As the tip comes close to the sample surface, an



attractive force between the tip and the surface leads the cantilever to deflect towards the sample surface. The cantilever's deflections towards or away from the surface are detected by a photodetector via an incident laser beam that is reflected off the cantilever top. Surface features (high and low points of the surface), cause alterations in the tip-surface interaction which are measured as shifts in frequency, phase and height (in tapping mode) [14-18]. The equipment used here was a Bruker Dimension FastScan using a FastScan-A (Bruker) probe used in tapping mode. The films investigated in this thesis are graphene and graphene oxide coating cavity resonators.

### **3.3.3. Scanning Electron Microscopy (SEM)**

In the course of this study scanning electron microscopy (SEM) was performed to observe the structural morphology of the samples. The working principle of conventional SEM is based on the high energy electrons that are used to generate a variety of signals at the surface of the solid samples[19]. These signals consist of secondary electrons (to produce the SEM image), back scattered electrons and diffracted back-scattered electrons. The secondary electrons are used to image the sample; they are valuable for showing the morphology of the sample. The diffracted back-scattered electrons illustrate contrast in the multiphase of the sample. In most of the experiments data is collected over a selected area of the specimen and two dimensional images are then generated that display spatial variations of the specimen [19-22]. The equipment used was an SEM FEI Quanta 200. Fig 3.5 (a), shows image of a 25 $\mu$ m radius silicon ring resonator with a 0.25 $\mu$ m coupling gap, (b) clearly depicts SEM cross section view of layered structure of a GO film on a cavity resonator. The GO layer easily observed from the wrinkles in the layer.

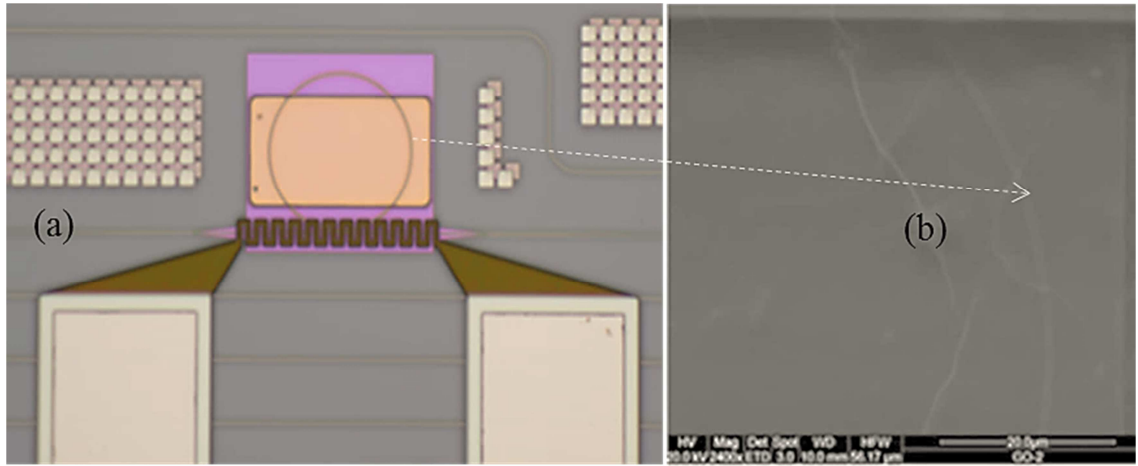


**Figure 3.5** An optical image showing SOI ring resonator of 25μm radius (b) SEM image cross section view of a GO film on an SOI waveguide.

### 3.4. Waveguide optical transmission

The standard method to characterize an integrated optical photonic device includes measuring the device's performance (spectrum response). The level of spectral detail required defines which setup technique is employed. One of these setups is based on measuring the wavelength response using a tunable laser with a detector. This setting system has been designed previously by members of the Manchester group to perform high resolution and rapid wavelength measurements with accurate fiber alignment; the other setup system is based on using a broadband light source and optical spectrum analyser (OSA) coupled into the input of the optical photonic device. This measurement system has limitations of measurements due to the resolution of the OSA spectrometer, which is around 50pm, so if the cavity resonator has very narrow full-width-at-half-maximum the resolution will be not sufficient. On the other hand, the speed and its ability to refresh the output signal every 10s make it suitable for real time sensing measurements. Here we introduce each setup as well as the system operation of this setup.

#### 3.4.1. Free-space spectroscopic (tuneable laser with InGaAs array)

For optical characterization, the sample was positioned on a holder placed in a 3-axis stage from Thorlabs. In order to visualize the position of the grating coupler during the alignment process a CCD camera connected to a large field of view microscope objective (Thorlabs LMS03- BB). All these elements were placed in an optical

breadboard in order to reduce the vibrations that can interfere in the measurement, as shown in Fig. 3.6.

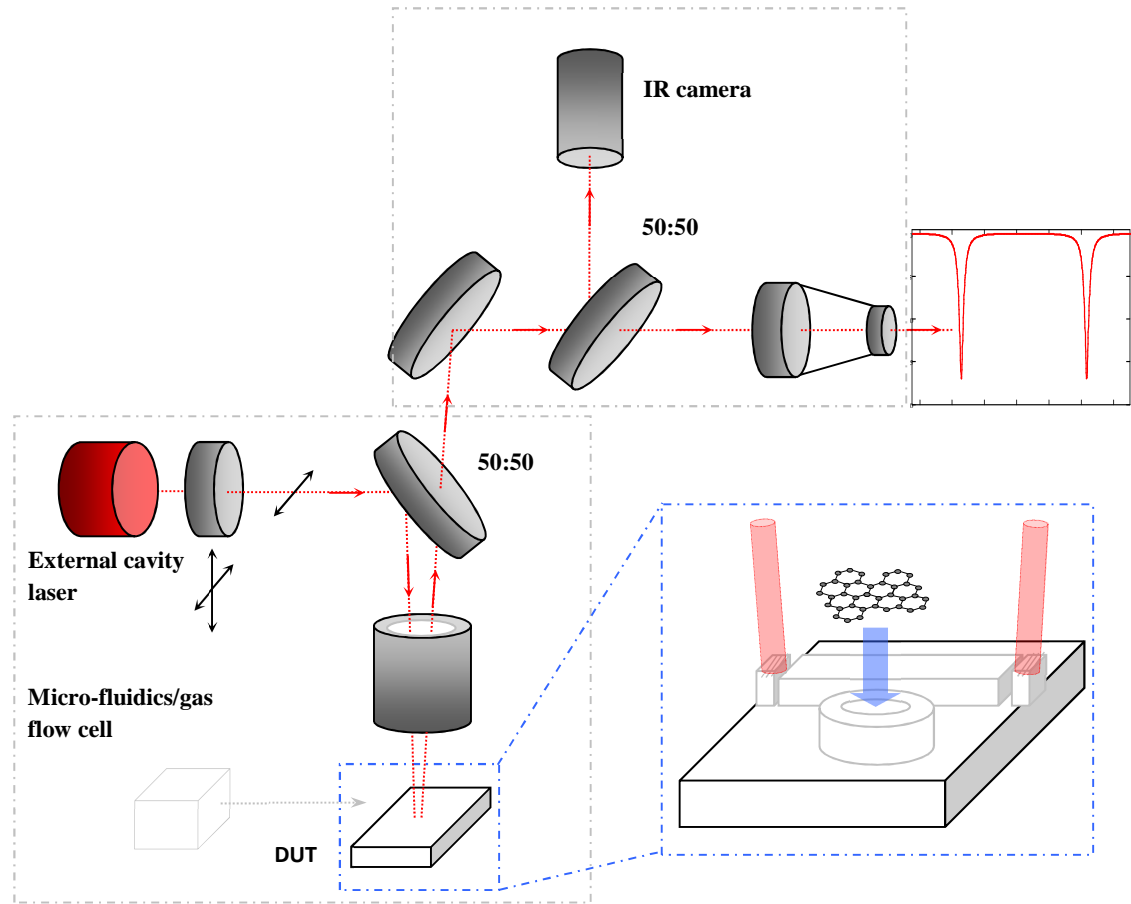


**Figure 3.6 Schematic representation of optical set-up testing platform [23]**

When the chip is located on the optical setup and it have been aligned with it, light from an external cavity tuneable laser (Thorlabs TLK-L1550R), used as a light source with an output wavelength range from 1480nm to 1610nm. In details, the laser beams is delivered through single mode fibre to a 50:50 beam-splitter where it is reflected at about  $\sim 11^\circ$  normal incidence into a large field of view microscope objective (Thorlabs LMS03-BB). The reflected downward laser beam is directly focused on the photonic device, where light is coupled into waveguide through a single input grating coupler located at one end of the waveguide, which tapers  $\sim 2\text{mm}$  to achieve single-guided mode operation. After light passing through the wave-guide with length  $\sim 3\text{mm}$ , light is coupled out through another grating coupler at a the same angle off the normal inclined in the opposite direction to the first. The light is collected via the same

objective lens back onto the beam splitter, and then it is reflected from a rotatable mirror onto a second 50:50 beam splitter, dividing the collected output light between the aperture of an infrared camera, which is used to image the waveguide input and output for alignment, and a fibre coupler, which focuses the light onto the end of a fibre where it is delivered to a benchtop, BayspecSuperGamut© spectrometer with thermo-electrically cooled InGaAs array detector. The measured transmission spectra were recorded as function of wavelength and collected by the provided data instrumentation software.

### **3.4.2. Free-space spectroscopic (broadband SLED and detection via OSA)**

The coupling system is the same as before except the source used is a broad band superluminescent LED centred on 1550nm. The transmitted light is then fed into an optical spectrum analyser. The measured transmission spectra were recorded as function of wavelength and collected by the provided data instrumentation software (a LabVIEW customized program), in which we set the range of wavelength and the OSA's resolution in order to perform the measurements. Simply the LabVIEW program accepts the information from the OSA and we save it in the computer, which will be analysed in order to determine the evolution of the ring resonators response.

## **3.5. Vapour sensing characterization**

### **3.5.1. Vapour sensing system**

Fig 3.7 schematically shows vapour handling sensing system used to generate different vapour concentrations of volatile compounds. A homemade bubbler contains a liquid solvent compound of interest. A small gas cell test system that was designed by the author was glued on the sensing silicon photonic chip and is used to achieve compatibility with the fibre-to infrared setup. The gas cell, made of black aluminium (CFRP), is 7mm wide, 3mm long and about 5mm high which accommodates a certain amount of gases to be detected in a fixed volume. The top side of the cell is sealed with a transparent (5mm thick, UVFS) quartz window in order to light can be coupled vertically through it. There are two holes in the cell: one for gas injection; and the one for gas releases. Glue (Norad -NEA121) is used to fix the silicon photonic chips inside cell. First the glue is coated on a clean substrate and transferred to the cell by press-stamping. Finally, we aligned the cell on the sensor chip.

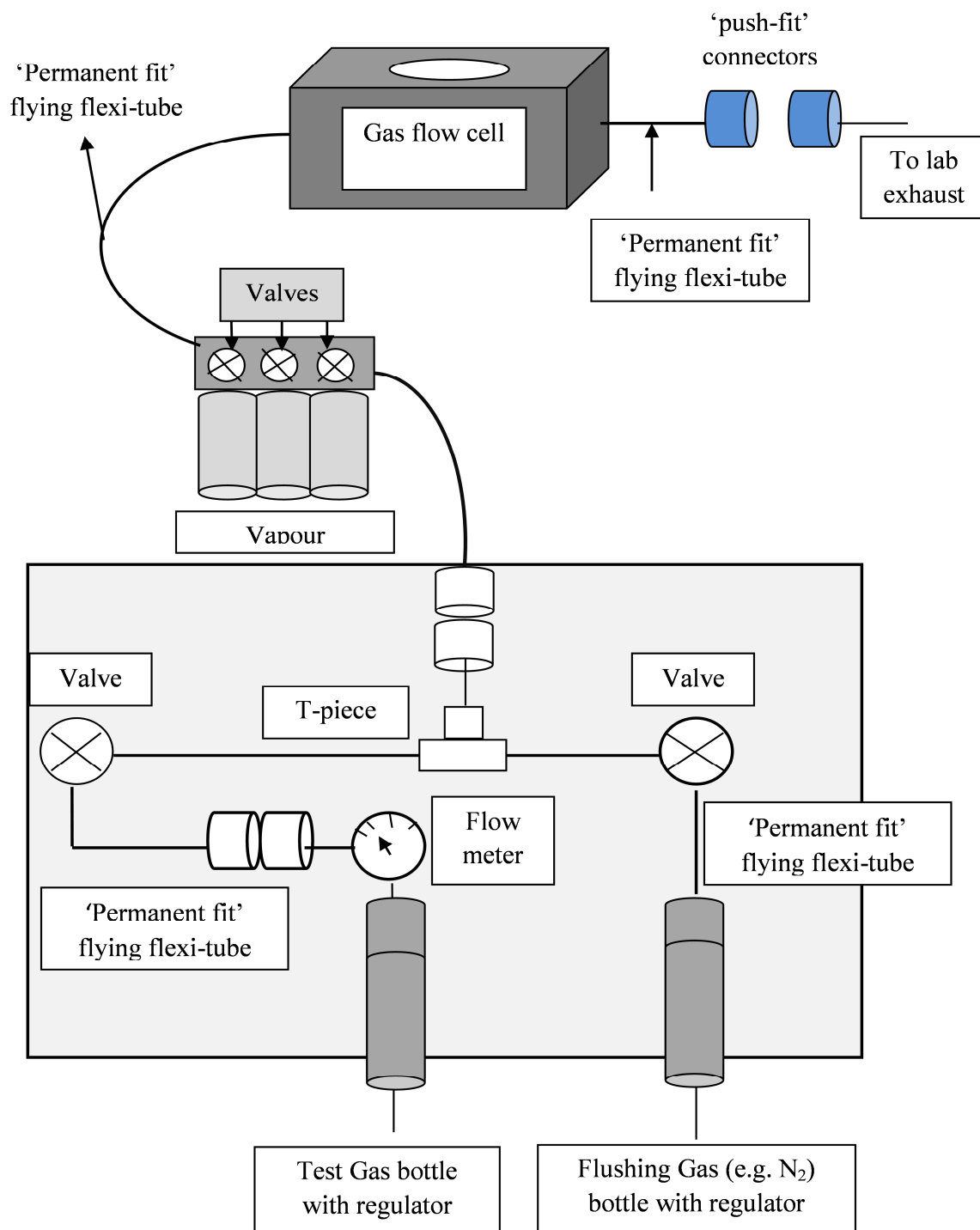


**Figure 3.7 Shows gas circuit diagram**

### **3.5.2. Optical gas sensing measurements**

A schematic of the optical setup used in conjunction with a gas cell which holds the chip under test is shown in Fig 3.6. The gas cell is connected to the gas supply (gas cylinders, and vapour source), and it is kept at atmospheric pressure. The gas flow into the cell is controlled with flow controllers. The exhaust valve on the other side of the chamber ensures continuous gas flow, the exhaust gas removed from the room. Low permeability, high chemical resistance, and high purity tubing were used in the vapour/gas flows system of the sensing setup experiments. Before any characterization, the gas cell is purged with a continuous carrier gas flow of nitrogen for 30 minutes. This step ensures that the cell and the tubes are cleaned of remaining vapour traces from previous experiments. Typically, a flow rate of 2-3 l/min was used for this step. The nitrogen flow is maintained after loading the sample, and the sensor output is monitored until a stable transmission spectrum is attained. For instance, for a ring resonator based sensor, the stability of the resonance wavelength is checked with continuous wavelength scan over a period of 10-20 minutes under nitrogen flow at room temperature. A steady state resonance within an accuracy of  $\pm 10$  pm is typically achieved with this procedure. This steady state condition is taken as a reference to the following experiments under gas exposure. The response of a sensor to different vapour/gas concentrations is measured with respect to the reference condition by varying the nitrogen gas flow while keeping a constant flow of vapour.

## **3.6. Measurement instruments**

### **3.6.1. Tunable laser**

For the tunable laser system, a high tuning resolution laser (Thorlabs TLK-L1550R)[24], and (TSL-510) [25] broadband source were used as a light source in most of the sensing experiments conducted in this thesis. The Thorlabs TLK-L1550R tunable laser covered the output wavelength range from 1480 nm to 1610 nm, and provided a narrow spectral line width of 0.1MHz with a high resolution. Input powers used in most characterization were typically below 2mW.

### **3.6.2. BayspecSuperGamut© spectrometer**

It covers spectral range from 900–1700 nm, and provided a spatial resolution of 5 – 20 nm depending on slot length[26].

### **3.6.3. Broadband source**

A superluminescent diode (SLD) is a broadband source with emission centred on 1550 nm with an optical bandwidth of 50 nm.

### **3.6.4. Optical Spectrum Analyzers (OSAs)**

The OSA203B Thorlabs[27] is a benchtop optical Spectrum Analyzers performs highly accurate spectral measurements, high performance optical resolution and high speed. It covers the spectral range of 600–1700 nm. It is compatible with both free-space light sources and fiber-coupled.

### **3.6.5. Monitoring System**

A monitoring system, including microscope and an infrared camera read-out, was predominantly used to simultaneously view the input/output alignment during the characterization of ring resonators based sensors in this thesis. The camera, which was attached to the microscope, was connected to the TV and the image is displayed on the TV monitor.

### 3.7. References

1. Clark, N., University of Manchester 2014.
2. Milan and F.Y.G. M Milosevic, Goran Z Mashanovich, *Optoelectronics Research Centre, University of Southampton*. 2013.
3. Lydiate, J., *University of Manchester, 2016*. 2016.
4. Li, X., et al., *Large-area synthesis of high-quality and uniform graphene films on copper foils*. Science, 2009. 324(5932): p. 1312-1314.
5. Song, L., et al., *Fast and controllable fabrication of suspended graphene nanopore devices*. Nanotechnology, 2012. 23(8): p. 085301.
6. Jeong, H.J., et al., *One-Step Transfer and Integration of Multifunctionality in CVD Graphene by TiO<sub>2</sub>/Graphene Oxide Hybrid Layer*. Small, 2014: p. n/a-n/a.
7. *Raman spectroscopy*. /2017 [cited 2017 5 May]; Available from: [https://en.wikipedia.org/wiki/Raman\\_spectroscopy](https://en.wikipedia.org/wiki/Raman_spectroscopy).
8. Bumbrah, G.S. and R.M. Sharma, *Raman spectroscopy–Basic principle, instrumentation and selected applications for the characterization of drugs of abuse*. Egyptian Journal of Forensic Sciences, 2016. 6(3): p. 209-215.
9. Raman, C.V. and K.S. Krishnan, *A new type of secondary radiation*. Nature, 1928. 121(3048): p. 501-502.
10. Zhang, Z., *Surface temperature measurement using optical techniques*. Annual Review of Heat Transfer, 2000. 11(11).
11. Larkin, P., *Infrared and Raman spectroscopy: principles and spectral interpretation*. 2011: Elsevier.
12. Long, D.A. and D. Long, *Raman spectroscopy*. Vol. 206. 1977: McGraw-Hill New York.
13. Ismail, K., *FABRICATION AND CHARACTERIZATION OF SURFACE-ENHANCED RAMAN SCATTERING SUBSTRATES THROUGH PHOTO-DEPOSITION OF GOLD NANOPARTICLES*. 2015.
14. Binnig, G.K., *Atomic force microscope and method for imaging surfaces with atomic resolution*, 1988, Google Patents.
15. *How AFM Works*. 2017.
16. Geisse, N.A., *AFM and combined optical techniques*. Materials today, 2009. 12(7): p. 40-45.
17. Binnig, G., C.F. Quate, and C. Gerber, *Atomic force microscope*. Physical review letters, 1986. 56(9): p. 930.
18. Seo, Y. and W. Jhe, *Atomic force microscopy and spectroscopy*. Reports on Progress in Physics, 2007. 71(1): p. 016101.
19. *Scanning electron microscope*. 2017.
20. Education, I.R.a. *Scanning Electron Microscopy (SEM)*. Integrating Research and Education MAY 2017 May 2017]; Available from: [https://serc.carleton.edu/research\\_education/geochemsheets/techniques/SEM.html](https://serc.carleton.edu/research_education/geochemsheets/techniques/SEM.html).
21. Wikipedia. *Scanning electron microscope*. 2017 [cited 2017 May]; Available from: [https://en.wikipedia.org/wiki/Scanning\\_electron\\_microscope](https://en.wikipedia.org/wiki/Scanning_electron_microscope).
22. Oatley, C., W. Nixon, and R. Pease, *Scanning electron microscopy*. Advances in Electronics and Electron Physics, 1966. 21: p. 181-247.



23. Crowe, I.F., et al., *Determination of the quasi-TE mode (in-plane) graphene linear absorption coefficient via integration with silicon-on-insulator racetrack cavity resonators*. Optics express, 2014. 22(15): p. 18625-18632.
24. THORLABS. *Tunable Lasers: Prealigned Littrow and Littman Kits*. [cited 2017 03/08/2017]; Available from: [https://www.thorlabs.com/newgrouppage9.cfm?objectgroup\\_id=4757&pn=TLK-L1550M](https://www.thorlabs.com/newgrouppage9.cfm?objectgroup_id=4757&pn=TLK-L1550M),
25. THORLABS. *Benchtop SLD Light Sources*,. [cited 2017 03/08/2017]; Available from: [https://www.thorlabs.com/newgrouppage9.cfm?objectgroup\\_id=4285](https://www.thorlabs.com/newgrouppage9.cfm?objectgroup_id=4285)
26. BaySpec, S.N.-S. *BaySpec, SuperGamut™ NIR-SWIR*,. [cited 2017 03/08/2017]; Available from: <http://www.bayspec.com/spectroscopy/nir-swir/>.
27. THORLABS and 04/09/2017. OSA203B - Fourier Transform Optical Spectrum Analyzer, 1.0 - 2.6  $\mu\text{m}$ , [cited 2017 03/08]; Available from: <https://www.thorlabs.com/thorproduct.cfm?partnumber=OSA203B>
28. J. R. Ferraro, K. Nakamoto and C. W. Brown, *Introductory Raman Spectroscopy*, 2nd ed. (Elsevier, San Diego, 2003).
29. L.M. Malarda , M.A. Pimenta a , G. Dresselhaus b , M.S. Dresselhaus, *Raman spectroscopy in graphene*, (Elsevier, San Diego, 2009).
30. Nastaran Kazemi-Zanjani, Erwan Kergrene, Lijia Liu, Tsun-Kong Sham and François, *Tip-Enhanced Raman Imaging and Nano Spectroscopy of Etched Silicon Nanowires*, Sensors 2013, 13, 12744-12759. L.M. Malarda , M.A. Pimenta a , G. Dresselhaus b , M.S. Dresselhaus, *Raman spectroscopy in graphene*, (Elsevier, San Diego, 2009).



## **Chapter 4: Experimental and theoretical study of monolayer graphene coated silicon MRRs**

Chemical functionalization of the silicon surface is necessary for optical sensing applications and the main challenge in this respect is silicon's relatively poor reactivity. Therefore, it is desirable to incorporate novel materials with silicon to provide a sensitization layer. Graphene, which is a thin two-dimensional material based on monolayer of carbon atoms, is expected to be a good candidate for this due to the unique properties of graphene[6]. Our approach is to coat cavity resonator surfaces with monolayer graphene, which offer the potential for enhancement in both the sensitivity and selectivity of miniature, chip-based devices for bio-/chemical sensing applications. In this chapter we discuss the characterization undertaken of graphene deposited on silicon photonics devices.

### **4.1. Determination of the quasi-TE mode (in-plane) graphene linear absorption coefficient via integration with silicon-on-insulator cavity ring resonators**

#### **4.1.1. Introduction**

Graphene is a thin two-dimensional material composed of a monolayer of carbon atoms, which has drawn considerable attention in recent years with research on it in many fields ranging from fundamental science to technological areas, since it was discovered in 2004 [6]. Graphene still represents a very attractive technology for applications in photonics and many graphene based photonic devices have been reported, such as optical modulators [7,8], high-speed photo-detectors [9-12], and optical polarizers [13]. The growing interest of graphene is due to its out-standing optical and electro-chemical properties such as high conductivity, high charge carrier mobility, wavelength independence, very high optical nonlinearity [6,14,15], ability to absorb light from visible to infrared wavelength regions [9,16], and its ability to intimately interact with various biomolecules such as proteins, and nucleic acid by virtue of  $\pi$ - $\pi$  interaction [17]. In addition, graphene has a very large specific surface

area of  $2630 \text{ m}^2\text{g}^{-1}$  [18], which integrates high chemical purity, reactivity, and easiness of functionalization by all means of chemical doping and electric and magnetic fields [15,18,19]. These superior properties make it possible for the introduction of high sensitive graphene based devices for optical bio, and gas sensing applications in various areas such as, medical diagnostics, healthcare, pharmaceuticals, and environment protection. On the other hand, graphene itself possesses zero energy gaps hence it has a poor “on/off” current ratio when incorporated onto electronic devices [20]. Similarly to silicon, it has an inertness to reaction [15]. However, the chemistry of graphene is well advanced and it still represents a good route to achieve enhanced sensitivities and selectivity from chip based sensors. The most often argument made in favour of graphene for these applications is its high compatibility with CMOS devices and the fabrication processes. Many technological advantages can be gained by the combination of the graphene and the silicon photonic devices. For instance, large operating bandwidth, weak optical absorption coefficient ( $\pi\alpha \approx 2.3\%$ ) at normal incident, and the small effective detection area of graphene limits its photo-responsivity that required for a commercial photo-detector [20]. However, integrating graphene with a silicon waveguide can greatly improve its responsivity and speed [20,22], because the light matter (graphene) interaction length and optical absorption can be increased significantly [20,23]. For example integrating graphene with a silicon waveguide, such as the Mach-Zehnder interferometer (MZI), and the cavity resonator, which are used to encode transmission data for optical interconnects, offers the potentials to improve responsivity of device precisely because of graphene’s an ultra-fast response across a broad spectrum [20]. Li *et al.* [24] have demonstrated the integration of single layer graphene onto a silicon MZI to determine the optical absorption coefficient ( $\alpha$ ) in graphene/waveguide, and the dependency of  $\alpha$  on the graphene/waveguide height. They reported a value for  $\alpha = 0.106 \text{ dB}/\mu\text{m}$  with the graphene deposited on the top of silicon waveguide. Kou *et al* [25] proposed incorporation of single layer graphene on a silicon wire waveguide to obtain the absorption efficiencies of the graphene on a silicon wire waveguide, by measuring different lengths of the graphene from 2.5 to  $200 \mu\text{m}$  light, they reported a 0.09 and 0.05  $\text{dB}/\mu\text{m}$  loss for TE- and TM-polarized respectively. In addition, the same workers in [25] have studied the influence on quality factor of varying the length of graphene

partially integrated into a single silicon MRR. They showed the Q factor sharply declines from nearly 8000 to approximately 1000 as the length of graphene integration on the ring increases from 0 to 20 $\mu\text{m}$ . Also they derived numerical results, which revealed an exponentially decreasing Q factor with increasing graphene length taking into account optical absorption of graphene and they compared this with their experimental results finding reasonable agreement. Also, Heng Cai and co-workers have studied linear absorption coefficient of monolayer graphene by the optical transmission spectra of a graphene layer with only several micrometers in length coated add-drop silicon micro ring resonator, they found a value of the loss to be around 0.23 dB/ $\mu\text{m}$  in their devices [26].

In this work, we discuss a device based on graphene integrated onto silicon racetrack cavity resonators, in an attempt to understand the effect of graphene on the optical properties of such a device, prior to demonstrating surface functionalization for bio-/chemical sensing applications. As a first step in this process, we report measurement of the optical response of graphene coated cavities and in so doing determine both the real part of the effective refractive index and the quasi-TE (in-plane) linear absorption coefficient for single layer graphene then combining this with a theoretical model of the coupling variation strengths with height  $h$  to recommend ideal conditions for graphene coated devices to serve as a sensitization layer.

#### **4.1.2. Sample preparation and characterization**

##### **4.1.2.1 Sample layout and cleaning**

Racetrack resonators, with equivalent racetrack-to-wire coupling lengths,  $L_c = 6, 10, 13\mu\text{m}$  and coupling gap,  $g = 0.3\mu\text{m}$  but different radii of curvature,  $r = 10, 20$  and  $40\mu\text{m}$  were used for this study. Before we performed graphene transfer the sample was cleaned to remove any contamination or particles. The sample was washed with acetone, isopropyl alcohol (IPA), and de-ionized (DI) water. This was followed by an oxygen plasma etch for 40s.

The graphene was grown by chemical vapour deposition (CVD) on copper foils (Gratome- RCu, Bluestone Global Tech) and transferred on to the SOI wafer containing the devices using a polymer-mediated wet transfer procedure described elsewhere [27]. The graphene was patterned, to ensure selective coverage of the race-track ring resonators, using raster-scan photolithography and oxygen plasma etching. In order to

ensure no residual photo-resist contamination remained on the sample, the sample was washed with acetone and heated at 270°C in a reducing atmosphere. Fig 4.1 shows a very thin layer of graphene coated on different racetrack rings of the same chip with slight variations in graphene coverage from device to device.

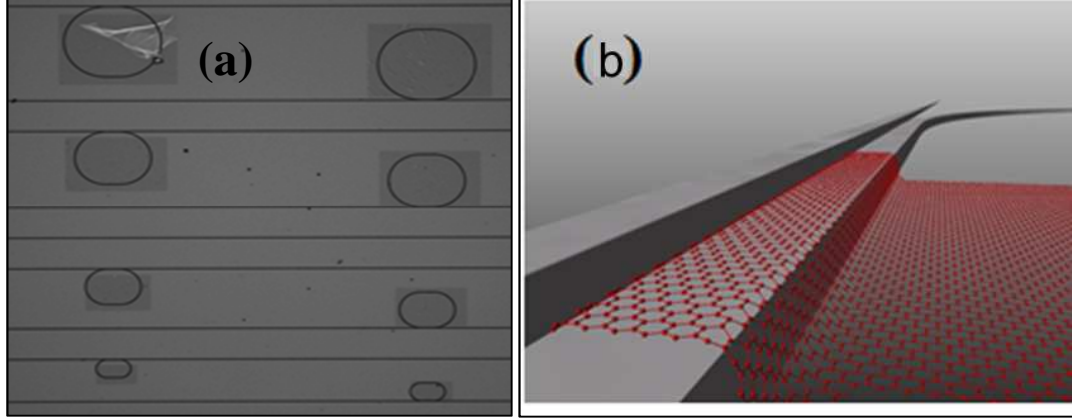


**Figure 4.1** Microscope image for the top view of the fabricated SOI nanowires with graphene on the top (b) Schematic of the graphene integrated race-track resonator; the image illustrates the selective (partial) coverage of the racetrack at the coupling section with the uncoated [20]

#### 4.1.2.2 Raman Spectroscopy characterization

Raman spectroscopy was carried out to assess the uniformity of the graphene on the sample. The samples were excited with a 514nm (Cobolt Fandango solid state diode) laser via a 50x microscope objective lens and the Raman spectra collected in a back-scattering geometry, dispersed in a Renishaw 1000 micro-Raman system. Fig 4.2 exhibits the measured Raman spectra with G and a 2D peak for the graphene covered region. The number of graphene layers (single layer,  $n = 1$  or multi layers,  $n = 2, 3...$ ) can be derived from Raman spectra in the following way; firstly the frequency of the G-peak,  $w_G(n) = 1581 + 11/(1 + n^{1.6})$ , the shape (width  $w_{2D}$ , and symmetry) of the 2D band is also characteristic for single layer graphene, finally the 2D/G peak intensity ratio [20, 28]. From Lorentzian fits to our measured G and 2D scattering peaks on the waveguide, we obtain  $w_G(n = 1) = 1587.2 \pm 0.1 \text{ cm}^{-1}$ , a symmetric 2D peak with a full width at half-maximum (FWHM) of,  $w_{2D} = 28 \text{ cm}^{-1}$  and the intensity ratio  $I_{2D}/I_G$  is approximately  $\sim 6$ , all of which suggest that the graphene is single atomic layer.

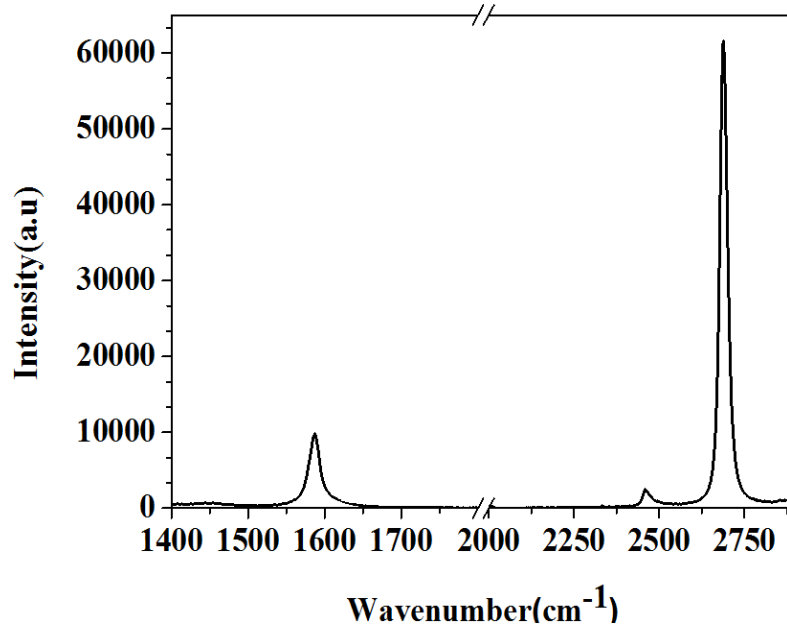


**Figure 4.2 Raman spectra with peaks for single layer graphene**

#### **4.1.2.3. AFM scanning characterization**

AFM was carried out on a Bruker Dimension to obtain the height profile of the monolayer graphene on the waveguide. Probe in tapping mode was used at a scan rate of 1.5Hz. The target sheet could be found by comparing images from the confocal microscope with images from the optical microscope in the AFM. The average value was taken between two levels. One level from no graphene point ( $OFF_{\text{graphene}}$ ) as reference and other points from graphene coated racetrack resonator. The distance between each two measured points ( $OFF_{\text{graphene}} - ON_{\text{graphene}}$ ) and the angle of the substrate profile was measured in software (Gwydion and data Analysis 2.1.15) and the height adjustment was calculated based on these values. Fig.4.3(a) shows AFM topographic image of CVD graphene coated cavity resonator, (b) respective height profile. The thickness of CVD graphene measured as  $1.18 \pm 0.2$  nm.

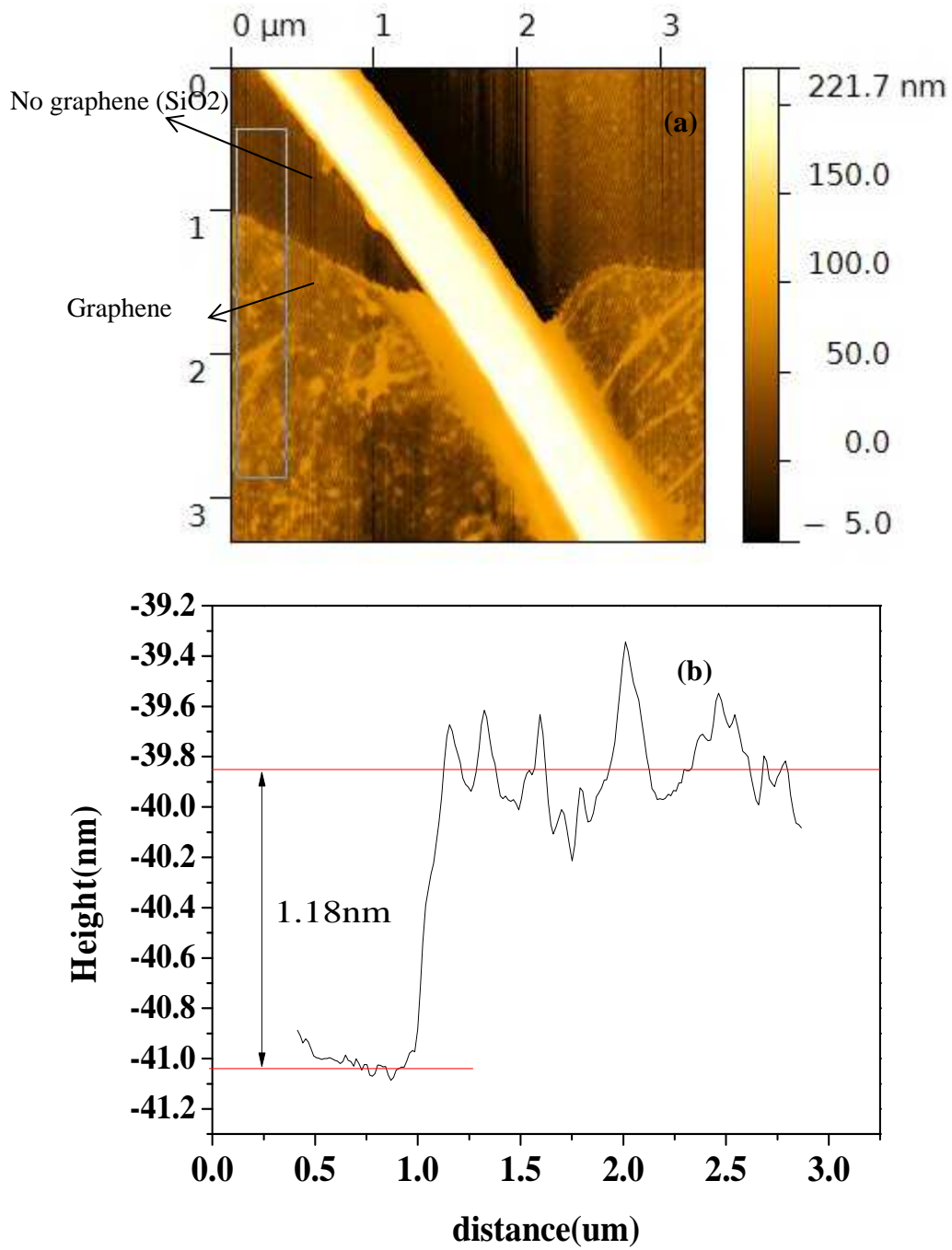


**Figure 4.3 AFM topographic image of CVD graphene coated cavity resonator (b) AFM thickness measurement of graphene using height profile between ON and OFF graphene sample**

#### **4.1.3. Results and dissuasion**

The waveguide transmissions before and after graphene deposition was studied using the measurement method described in section 3.3.2.1. In order to determine how much light was absorbed by the graphene when it coats the silicon waveguide, several



different sizes and parameters of racetrack ring resonators were used and modelling was performed assuming the following equation for the transmission of the output intensity of racetrack resonator given by [29]:

$$T(\lambda, L, n_{eff}, \alpha) = (1 - \gamma) \left[ \frac{(\sqrt{1-k}) - (\sqrt{1-\gamma}) e^{-\alpha \frac{(Ln_{eff})}{2} - i \left( 2\pi n_{eff}^2 \frac{L}{\lambda} \right)}}{1 - (\sqrt{1-\gamma})(\sqrt{1-k}) e^{-\alpha \frac{(Ln_{eff})}{2} - i \left( 2\pi n_{eff}^2 \frac{L}{\lambda} \right)}} \right]^2 \quad (4.1)$$

Where  $\alpha$  is the loss coefficient in the waveguide, which includes contributions from both scattering and absorption loss,  $\gamma$ : intensity loss factor,  $k$  is the coupling efficiency between the bus and the adjacent bent waveguide in a coupling region.  $L_c$  is the coupling length and  $(C = 2\pi r + 2L_c)$  is the circumference of the racetrack ring resonator.

#### 4.1.3.1 Optical transmission measurements of cavity resonator's before coating with graphene

A measured transmission spectrum (the red curve) for racetrack ring resonator device with,  $r=40\mu\text{m}$  without graphene shown in Fig 4.4. The quality factor ( $Q = \lambda_0/\Delta\lambda$ ) of each peak can be achieved directly from the graph with an accurate ruler to obtain  $\lambda_0$ , and FWHM, or by applying a symmetric Lorentzian function fit to each peak for reliable reading. Three peaks Q-factor measurements were made from Lorentzian fit and find an average with an associated standard deviation. The device discussed here exhibits a relatively high quality factor ( $Q = \lambda_0/\text{FWHM}$ ) of  $27540 \pm 1400$ . The high  $Q$  factor is desired to detect small shifts of resonance wavelength.

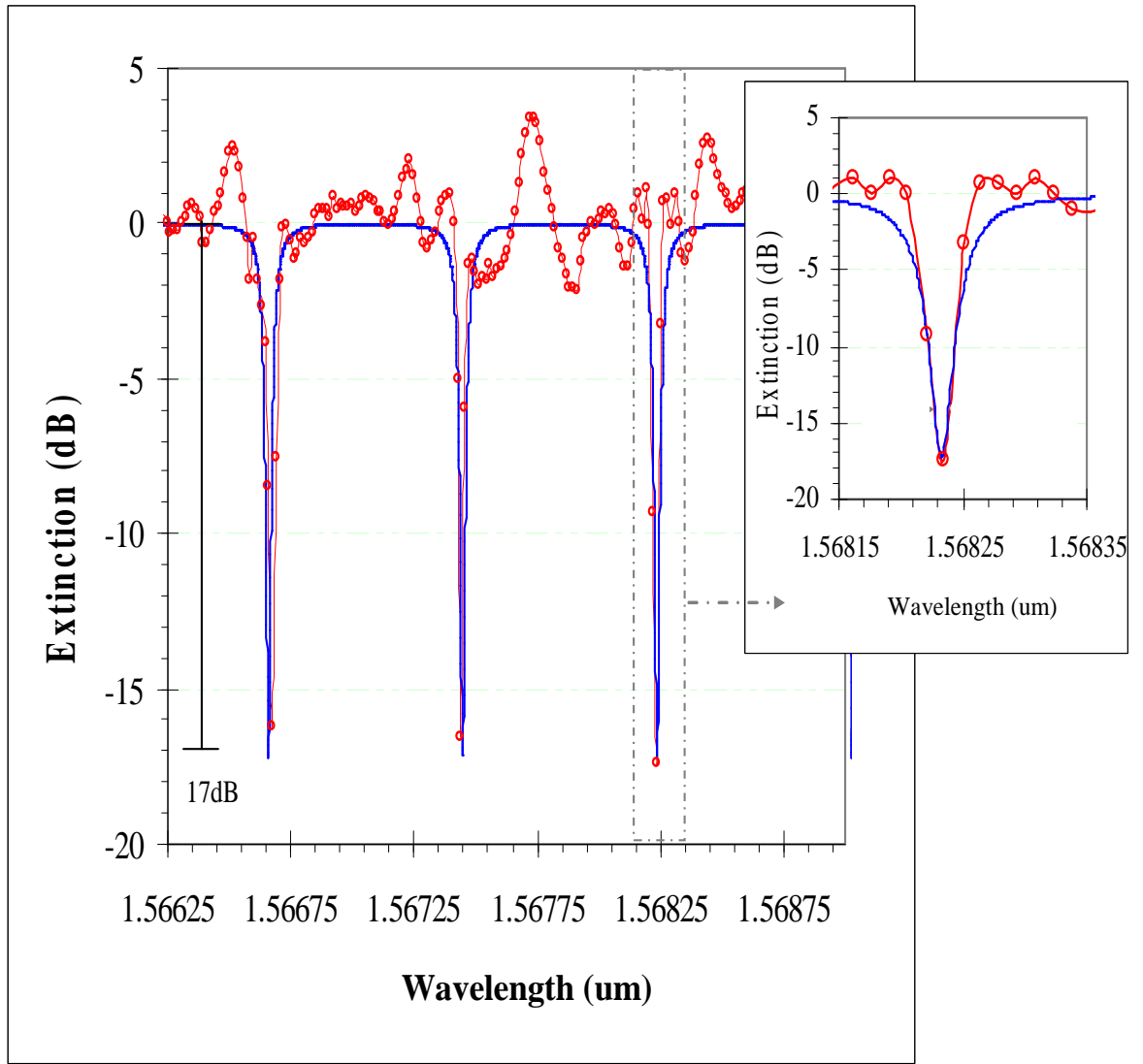


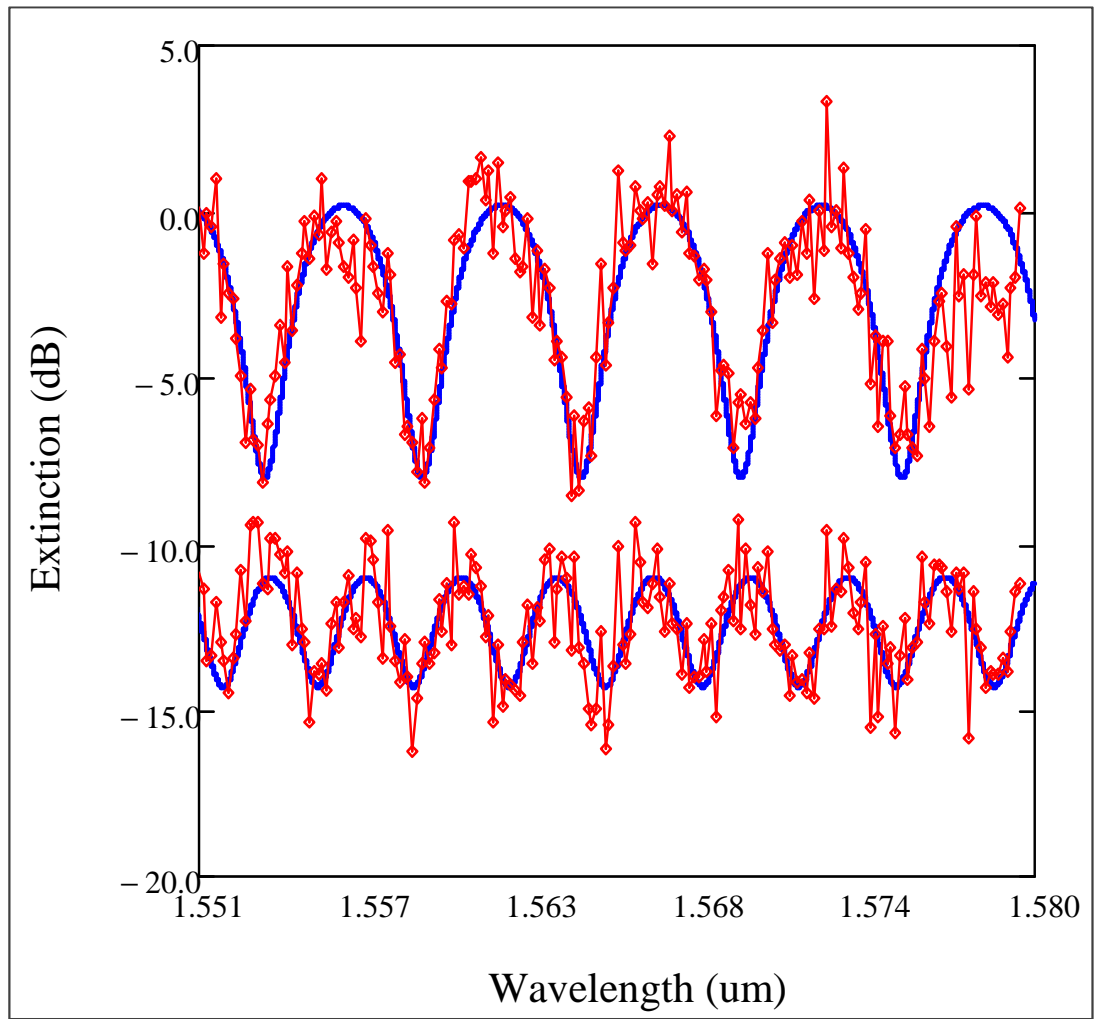
**Figure 4.4** Measured transmission spectrum at the throughput port of the silicon racetrack resonator with no graphene (physical dimensions,  $r = 40\mu\text{m}$  and  $L_c = 13\mu\text{m}$ ). The blue line is a calculation following the theory described in the text. Inset: close-up of the resonance peak wavelength is  $1.56823\mu\text{m}$  and the  $\Delta\lambda$  is  $0.00005694\mu\text{m}$ . The Q-factor calculated with these numbers is 27546.6.

The theoretical fit (blue curve) to the experimental data shown in Fig.4.4 was obtained using the following parameters,  $r = 42.5\mu\text{m}$ ,  $CL = 14\mu\text{m}$ ,  $k = 0.1$ ,  $g = 0.19$ , the effective index of the waveguide  $n_{\text{eff}} \sim 3.249 \pm 0.0005$ . The values of radius and coupling length that derived from the theoretical fit closely match the design values. From Fig.4.4, the fit to peak extinction using Eq.4.1 revealed that the extinction ratio for the no-graphene resonator is ER~17dB on resonance. From the theoretical modelling, the loss coefficient

in the no-graphene ring,  $=1.737 \pm 0.0002 \text{ dBcm}^{-1}$ , which is in an excellent agreement with the literature value [30].

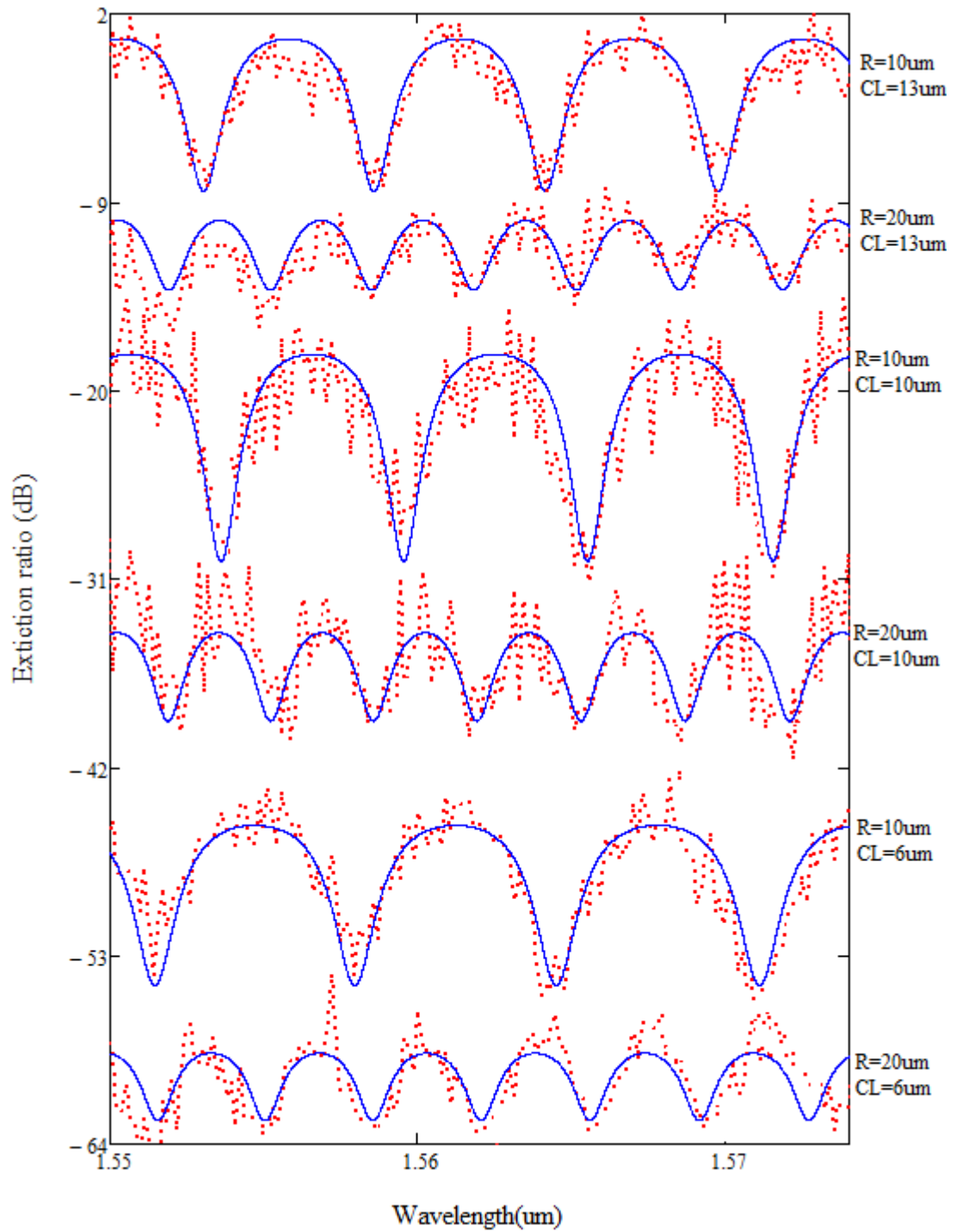
#### 4.1.3.2. Optical transmission measurements of the RR's after coating with Graphene

The racetrack ring resonators with graphene integrated were tested experimentally for their spectral response via the through port of the devices. For entirely coated devices with ( $r = 30$ , and  $40 \mu\text{m}$ ) and  $L_c = 13 \mu\text{m}$  ( $L_g > 152 \mu\text{m}$ ) there is no discernible spectral resonance.



**Figure 4.5** Measured (red) and modelled (Eq. (4.1) blue line,) transmission spectra of two corresponding graphene integrated silicon racetrack resonators with (top)  $r = 10 \mu\text{m}$  and (bottom)  $r = 20 \mu\text{m}$ .

The typical transmission spectra obtained for rings of different radii ( $r=10$  and  $20\mu\text{m}$ ) are shown in Fig.4.5 (a), a theoretical fit is shown (red curve) using Eq. 4.1 for both rings with corrected of graphene coverage,  $n (= L_g/L; 0 < n < 1)$ . The effective refractive index evaluated from model is  $n_{\text{eff}}=2.23\pm0.02$ , in good agreement with values in the literature for single-layer graphene [24], and, as expected, lower than that of bulk graphite [23]. The variation we obtain in  $n_{\text{eff}}$ , going from un-coated to graphene coated cavities indicates an altered modal propagation in our system and suggests that the optical properties, including the index of refraction are modified substantially by the graphene. The model also yields the linear absorption coefficient of *in-plane* monolayer graphene,  $\alpha=0.104\text{dB}\mu\text{m}^{-1}$ , which agrees with the published values [24,25]. From Fig.4.5, there is an observed broadening of the resonance, and the change in extinction ratio for the ring  $r = 10\mu\text{m}$  ( $L_g = 53 \mu\text{m}$ ) is larger than that for the ring with radius  $20\mu\text{m}$  ( $L_g = 106\mu\text{m}$ ), where ER for ring 1 achieves 8dB and for ring 2 this value is only, ER  $\sim 4.25\text{dB}$ . So we observe extinction ratio decreasing with the increasing ring size. This reduction of the extinction ratio and broadening of the resonance probably occur as a result of increased absorption (propagation loss) induced by the graphene layer deposited at the cavity surfaces, as variations in the scattering losses due to tighter bend radii are negligible in the as delivered samples. These losses are a strong function of the graphene length, thus we undertook measurements to determine the absorption coefficient for graphene, by measuring the transmission spectra of all six different graphene integrated rings (three with  $r = 10\mu\text{m}$  and three with  $r = 20\mu\text{m}$ ) with different coupling length to determine the extinction ratio values.



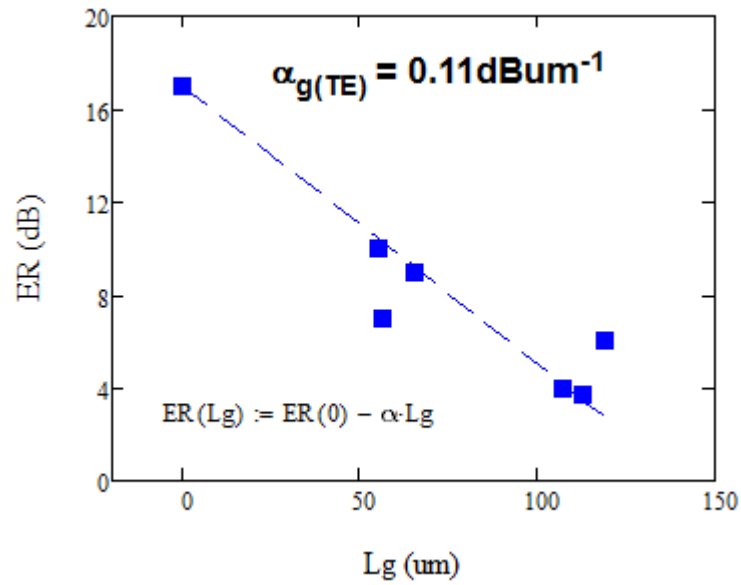
**Figure 4.6 Measured (red) and modelled (Eq. (4.1) blue line) transmission spectra of six different sizes racetrack ring resonator with varying radii and coupling lengths**

Fig. 4.6 shows representative measured transmission spectra for samples with varying radii and coupling length. The transmitted spectra are fitted with Eq.4.1, and the extinction ratio of each device is plotted as a function of  $L_g$  along with the extinction

ratio for the no graphene ring as shown in Fig.4.7 using a linear regression fit of the following equation:

$$ER(L_g)dB = ER(0)dB - \alpha * L_g \quad (4.2)$$

This indicates a linear in-plane absorption coefficient of monolayer graphene in this geometry, of  $\alpha_g = 0.11 \pm 0.01 \text{dB}\mu\text{m}^{-1}$ , which is comparable (within experimental error) to the value obtained from the fitting to the transmission spectra of Eq.4.1 in Fig.4.5. We note this value is in excellent agreement with the literature values, which were reported in references [21,30].



**Figure 4.7** Measured peak extinction as a function of graphene length,  $L_g$  with linear regression fit of the form  $ER(L_g) \text{ dB} = ER(0) \text{ dB} - \alpha L_g$ , with slope  $\alpha_g = 0.11 \pm 0.01 \text{dB}\mu\text{m}^{-1}$ .

## 4.2. Model of the graphene optical losses (based on the height-length parameters) for racetrack resonators and discussion

In order to investigate the spacing between the waveguide and graphene, our model has been extended to calculate signal attenuation as function of graphene length and graphene height over the waveguide. In reference [24], hydrogen silsesquioxane (HSQ) cladding layers were deposited on photonic substrates and then single layer graphene was integrated onto the planar HSQ at varying heights above the waveguides. In this case the absorption coefficient depends on height,  $h$  above the waveguide, for evanescent coupling we can write:

$$\alpha(h) = \alpha_0 e^{-2\gamma h} \quad (4.3)$$

Where  $\gamma$  is the waveguide field decay constant and  $h$  is the height over the waveguide, in our case  $\gamma = 8.5\mu\text{m}^{-1}$  is the waveguide evanescent field decay constant determined from a fit to the data of Fig.4(d) in reference [21] and  $\alpha_0 = 0.11\text{dB}\mu\text{m}^{-1}$ , the experimental value we have determined for the TE-mode graphene linear absorption coefficient for zero distance  $h = 0$  (on the surface of the waveguide). To include Eq. (4.3), we can write an expression for the resonant signal attenuation  $A_g(L_g, h)$ , induced by the graphene as:

$$A_g(L_g, h)_{dB} = [ER(0) - ER(L_g)]_{dB} = \alpha_0 e^{-2\gamma h} L_g \quad (4.4)$$

This gives us a contour map of calculated signal attenuation  $A_g$  as function of graphene length,  $L_g$  and height,  $h$  over the waveguide shown in Fig.4.8 (a).

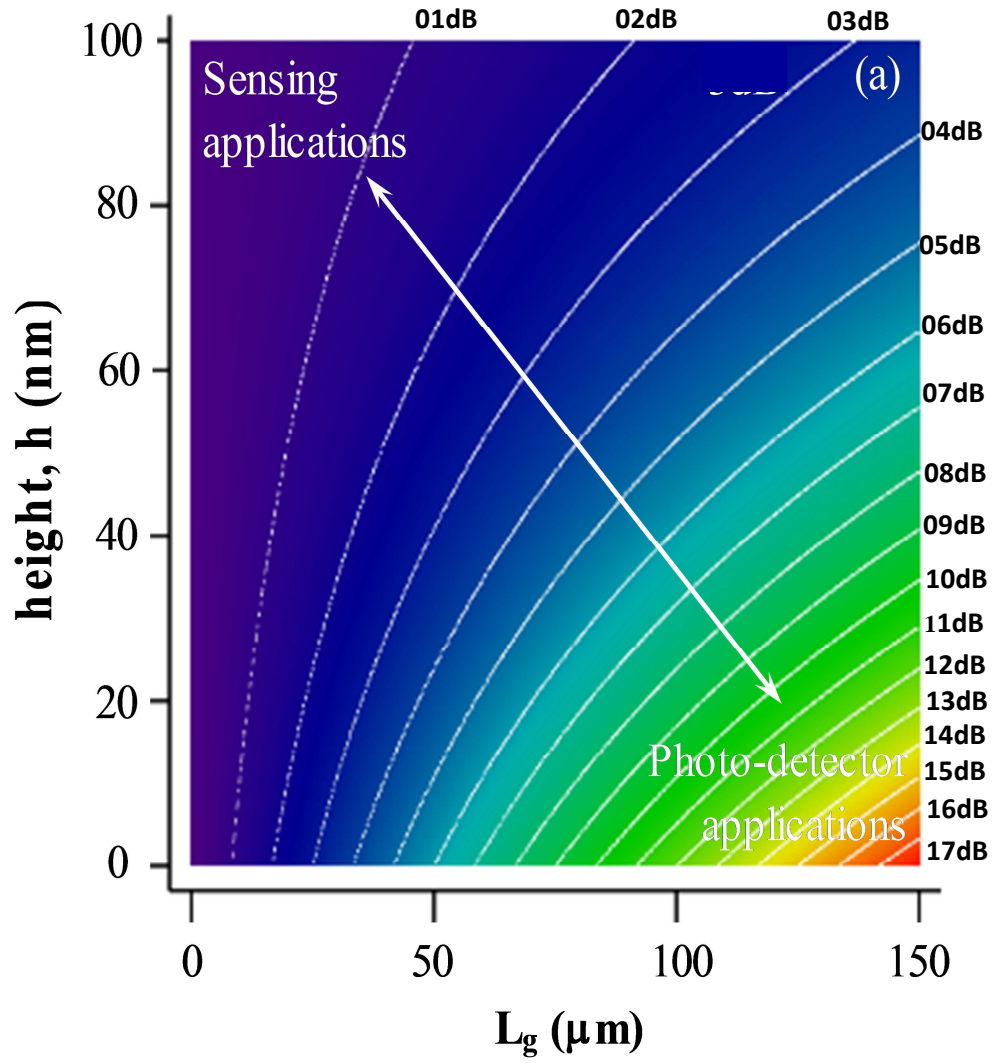
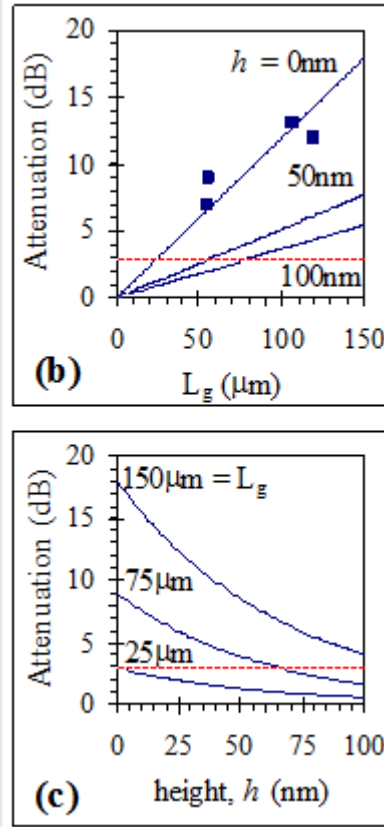


Figure 4.8 (a) contour plot of the calculated signal attenuation,  $A_g$  (blue – low, orange – high, contour lines–1dB increment) as a function of length,  $L_g$  and height,  $h$  of graphene over the silicon cavity ring resonator.





**Figure 4.8: (b) Calculated  $A_g$  as a function of  $L_g$  for specific heights ( $h = 0, 50, 100\text{nm}$ ) along with our real measured data (blue squares) (all plotted data is normalised to the point for  $L_g = 0$ , i.e. attenuation due to graphene is defined relative to the device without graphene as per equation  $A_g(L_g, h) = ER(0) - ER(L_g)$ , where  $ER(0)$  real our measured point for no-graphene resonator  $ER(0) \sim 17\text{dB}$ , and  $ER(L_g)$  our real measured data at different graphene length), and (b) calculated  $A_g$  as a function of height for specific lengths ( $L_g = 25, 75, 150\mu\text{m}$ ). The red dashed lines in both indicate where the cavity resonance  $ER = 3\text{dB}$  (as a notional limit of detection).**

Figs 4.8(b) and 4.8(c), indicate that for shorter lengths of graphene or when graphene layer is placed at larger height, the cavity resonance signal loss is negligible. For instance, for  $\leq 25\mu\text{m}$  of graphene, the cavity resonance signal attenuation induced is insignificant. However, for longer lengths of graphene, signal loss becomes more significant or when graphene resides at zero distance above the waveguide. For example, for  $L_g = 150\mu\text{m}$ , a cavity resonance with  $ER(0) \sim 17\text{dB}$  which is the same value obtained in Fig. 4.4, and for the same length of graphene and the height,  $h \sim 120\text{nm}$ , the cavity loss diminished to half its original value. This matches well with our results for entirely coated cavity resonators with  $r > 20\mu\text{m}$ , for which the experiment data yields no spectra responses. In order to confirm that graphene was placed directly on

the top of waveguide surface, we conducted an analysis using atomic force microscopy (AFM) of a step caused by plasma etching of the graphene, which indicates a height,  $1 < h \leq 1.5 \text{ nm}$ . This is typical for graphene on an intrinsic silicon dioxide surface, particularly under normal conditions and indicates that graphene layer is located on the silicon surface. The result of our model provides important rules for future design of graphene and silicon photonic devices for different application. For instance, graphene based sensing application, where it depends on being able to measure small resonant wavelength shifts in the cavity, and the role of graphene is sensitization layer, only want partial absorption in graphene, i.e. need small and/or large  $h$  to ensure graphene does not quench resonances in transmission spectra. Whereas for photo-detector applications, want complete absorption of the light, i.e. need small  $h$  and/or long  $L_g$ .

### 4.3. Summary

In summary, a single layer of graphene has been applied onto racetrack resonators based on (SOI) strip waveguides in order to modify the surface reactivity for biomolecular and /or gas sensing applications. The analysis of the transmission spectra for no graphene and graphene integrated racetrack resonators reveals, for first time using in-plane (light travels along the graphene layer) technique, the effective refractive index for graphene of  $n_{\text{eff}} = 2.23 \pm 0.02$ , and the quasi-TE mode (in-plane) absorption coefficient value in graphene of  $\alpha_g \text{ TE} = 0.11 \pm 0.01 \text{ dB}\mu\text{m}^{-1}$ . This result agrees well with the reported literature values of  $\alpha = 0.106 \text{ dB}/\mu\text{m}$  for the integration of CVD graphene onto silicon Machzehnder interferometer (MZI)[24], and  $\alpha=0.09 \text{ dB}/\mu\text{m}$  for CVD graphene on a silicon wire waveguide for TE-polarized[25]. The analysis of the modelling of the cavity signal loss for different length and height of the graphene over the cavity devices gives an insight into the design requirement of graphene integrated silicon photonic devices according to the required application. For e.g. photo-detector applications, one requires maximum absorption in the graphene layer and therefore designs should aim for large  $L_g$  and/or small  $h$ . However, for refractive index sensing applications, these design rules dictate that small  $L_g$  and/or large  $h$  should be employed to improve the reactivity of the silicon surface without sacrificing the cavity resonance signal. For future work, the researchers in photonics and optoelectronic, which are using such a parallel arrangement of graphene and a waveguide, would take these results into consideration during designing devices for different applications such as photo-detectors, bio/or gas sensors, modulators, and polarizations.

#### 4.4. References

1. Kou, R., et al., Influence of graphene on quality factor variation in a silicon ring resonator, in *Applied Physics Letters* 2014. p. 091122.
2. Park, M.K., et al., Label-free aptamer sensor based on silicon microring resonators. *Sensors and Actuators B: Chemical*, 2013. **176**: p. 552-559.
3. Passaro, V., et al., Recent advances in integrated photonic sensors. *Sensors*, 2012. **12**(11): p. 15558-15598.
4. Cho, H.K. and J. Han, Numerical study of opto-fluidic ring resonators for biosensor applications. *Sensors*, 2012. **12**(10): p. 14144-14157.
5. Ramachandran, A., et al., A universal biosensing platform based on optical micro-ring resonators. *Biosensors and Bioelectronics*, 2008. **23**(7): p. 939-944.
6. Wang, H., et al., Vibrational properties of graphene and graphene layers. *Journal of Raman Spectroscopy*, 2009. **40**(12): p. 1791-1796.
7. Liu, M., et al., A graphene-based broadband optical modulator. *Nature*, 2011. **474**(7349): p. 64.
8. Bao, Q. and K.P. Loh, Graphene photonics, plasmonics, and broadband optoelectronic devices. *ACS nano*, 2012. **6**(5): p. 3677-3694.
9. Xia, F., et al., Ultrafast graphene photodetector. *Nature nanotechnology*, 2009. **4**(12): p. 839-843.
10. Furchi, M., et al., Microcavity-integrated graphene photodetector. *Nano letters*, 2012. **12**(6): p. 2773-2777.
11. Mueller, T., F. Xia, and P. Avouris, Graphene photodetectors for high-speed optical communications. *Nature photonics*, 2010. **4**(5): p. 297-301.
12. Wang, X., et al., High-responsivity graphene/silicon-heterostructure waveguide photodetectors. *Nature photonics*, 2013. **7**(11): p. 888-891.
13. Bao, Q., et al., Broadband graphene polarizer. *Nature Photonics*, 2011. **5**(7): p. 411-415.
14. Kou, R., et al., Characterization of optical absorption and polarization dependence of single-layer graphene integrated on a silicon wire waveguide. *Japanese Journal of Applied Physics*, 2013. **52**(6R): p. 060203.
15. Georgakilas, V., et al., Functionalization of graphene: covalent and non-covalent approaches, derivatives and applications. *Chem. Rev*, 2012. **112**(11): p. 6156-6214.
16. Luchansky, M.S. and R.C. Bailey, High-Q optical sensors for chemical and biological analysis. *Analytical chemistry*, 2011. **84**(2): p. 793-821.
17. Guo, Q., et al., Silicon-on-glass graphene-functionalized leaky cavity mode nanophotonic biosensor. *Acs Photonics*, 2014. **1**(3): p. 221-227.
18. Matte, H.R., K. Subrahmanyam, and C. Rao, Synthetic aspects and selected properties of graphene. *Nanomaterials and Nanotechnology*, 2011. **1**: p. 5.
19. Wang, S., et al., Distorted Graphene Sheet Structure-Derived Latent Nanoporosity. *Langmuir*, 2016. **32**(22): p. 5617-5622.
20. Crowe, I.F., et al., Determination of the quasi-TE mode (in-plane) graphene linear absorption coefficient via integration with silicon-on-insulator racetrack cavity resonators. *Optics express*, 2014. **22**(15): p. 18625-18632.
21. Claes, T., W. Bogaerts, and P. Bienstman, Experimental characterization of a silicon photonic biosensor consisting of two cascaded ring resonators based on the Vernier-effect and introduction of a curve fitting method for an improved detection limit. *Optics express*, 2010. **18**(22): p. 22747-22761.

22. Novoselov, K.S., et al., A roadmap for graphene. *Nature*, 2012. **490**(7419): p. 192-200.
23. Kim, K., et al., A role for graphene in silicon-based semiconductor devices. *Nature*, 2011. **479**(7373): p. 338.
24. Li, H., et al., Optical absorption in graphene integrated on silicon waveguides. *Applied Physics Letters*, 2012. **101**(11): p. 111110.
25. Kou, R., et al., Influence of graphene on quality factor variation in a silicon ring resonator. *Applied Physics Letters*, 2014. **104**(9): p. 091122.
26. Cai, H., et al., Enhanced linear absorption coefficient of in-plane monolayer graphene on a silicon microring resonator. *Optics express*, 2016. **24**(21): p. 24105-24116.
27. Li, X., et al., Large-area synthesis of high-quality and uniform graphene films on copper foils. *Science*, 2009. **324**(5932): p. 1312-1314.
28. Kim, K., et al., Raman spectroscopy study of rotated double-layer graphene: misorientation-angle dependence of electronic structure. *Physical review letters*, 2012. **108**(24): p. 246103.
29. Menon, V., W. Tong, and S. Forrest, Control of quality factor and critical coupling in microring resonators through integration of a semiconductor optical amplifier. *IEEE Photonics Technology Letters*, 2004. **16**(5): p. 1343-1345.
30. Niehusmann, J., et al., Ultrahigh-quality-factor silicon-on-insulator microring resonator. *Optics letters*, 2004. **29**(24): p. 2861-2863.



## Chapter 5: Raman mapping analysis of graphene integrated silicon micro-ring resonators

### 5.1. Introduction

Raman spectroscopy has been widely used as a sensitive tool to evaluate graphene's electronic and vibrational properties [4] including strain [5], doping level [6], defect density [7], and edge structure[8] , although the effects of these can be difficult to separate from those influenced by the substrate. The Raman intensity, shift rate, width, and splitting of the graphene Raman peaks with strain and p- n-type doping has already been reported [5, 9-11]. The effect of both top and back gating on the graphene G peak position was also reported to lead to an upshift in the peak frequency for both n and p-type doping [12].

Graphene has three main Raman spectral bands, each with a distinct physical origin: the doubly resonant disorder related D peak usually associated with graphene defects appears around  $1350\text{cm}^{-1}$ [13] and is related to disorder, meaning that its appearance and relative intensity are often used as a measure of transferred material quality (i.e. it is weak or absent in high quality material). The other two main peaks are the G peak, which give rise from in-plane scattering of zone centre phonons, and located around  $1580\text{cm}^{-1}$  [8,13] and the 2D peak, around  $2700\text{cm}^{-1}$  is second order of the D peak [14] [14,15-17]. The shape, intensity and positions of the G and 2D peaks allow determination of the number of graphene layers as well as any strain and the presence of the carrier concentration in the material [8,14] .

Graphene incorporation with the silicon photonics platform is very interesting from a number of device applications perspectives; e.g. for demonstrating enhanced biochemical sensors in which the graphene acts as a sensitization layer in the underlying silicon photonics device for adsorbed species that may be probed by evanescent optical fields. The two dimensional nature of graphene also leads to a band structure for which electron filling can be tuned by very low power electrostatic gating to adjust the linear and non-linear optical properties. In particular, the 'Pauli blocking' effect can be used to change the opacity of the material to incoming photons, providing the possibility of very fast (GHz) optical modulation or switching for telecoms applications. Previous

studies [18-21] of the in-plane linear absorption coefficient of graphene by incorporation with silicon photonics waveguide based devices have determined quite different results, suggesting that the specific transfer process and substrate interface quality in these studies may play some role in the variations observed. In this chapter, the spatial characterization of the Raman G and 2D peaks across a graphene coated silicon photonic racetrack resonators using a mapping technique is demonstrated. Our approach is to investigate both the G and 2D peak frequencies and their relative integrated intensities and correlate these with spatial position to provide detailed information on the effect of the underlying silicon waveguide structure on graphene's structural and optoelectronic properties at this interface.

## **5.2. Experimental details**

### **5.2.1. Sample layout**

The devices reported in this study are racetrack resonator with radii 10,20 $\mu\text{m}$  and coupling gap 0.3 $\mu\text{m}$ . The synthesis process of graphene and the sample cleaning film followed the procedure detailed in section 4.1.2.1 (chapter 4)

### **5.2.2. Raman mapping characterisation**

The Raman maps were performed at room temperature in back scattering configuration, using a Horiba LabRAM HR Evolution Spectrometer. The samples were excited by 633 nm Helium Neon laser light and mechanical movement of the sample during mapping was provided by a Marzhauser motorized microscope XYZ stage. The incident laser light was focused on the sample surface using a 50x objective lens with numerical aperture of 0.75. Before doing any measurements on our devices, the Raman system was calibrated using a silicon sample which shows a sharp peak due to the silicon LO phonon at 520 $\text{cm}^{-1}$ . After the focus point was observed on the silicon surface, The Raman laser power on the samples was set to 2mW in order to reduce any damage induced heating of the graphene surface[23].

Raman maps were obtained for two different graphene integrated silicon micro-ring resonator devices, with radii of curvature,  $r = 10$  and  $20\mu\text{m}$ . The maps were obtained from a  $120 \times 120$  point array with a step size between each point of  $0.25\mu\text{m}$  and the precise position and intensity of the Raman G and 2D peaks were determined by fitting Lorentzian line-shapes to the spectral peaks.



### 5.3. Results and discussion

Prior to the Raman mapping study, we measured single point Raman scattering signal after transfer using a 514-nm as shown in Fig 5.1. The transferred graphene exhibits a very weak Raman D peak indicating a relatively low defect density, and an intense (relative to the G peak), symmetric 2D peak and the frequency of the G-peak of  $1587\text{cm}^{-1}$ , confirm that the graphene is single layer [24].

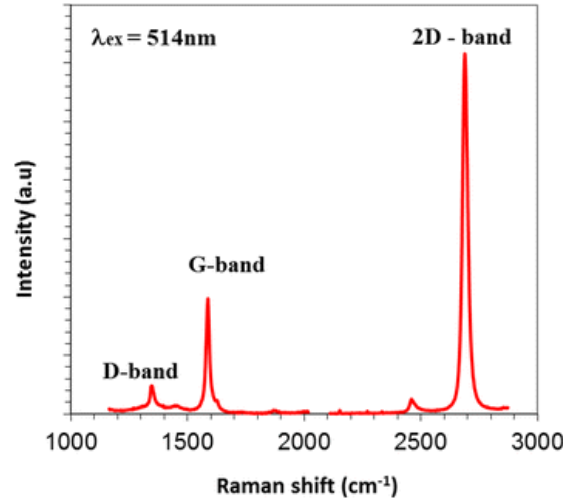


**Figure 5.1 Raman spectra with peaks for CVD graphene on Si waveguide**

#### 5.3.1. Raman line scan mapping

Spatial line scans of the graphene Raman G and 2D modes were made across the middle of the micro-ring resonators for both 10μm and 20μm radius devices. The spectra were taken using 100x objective lens, and the spatial measurements were obtained with a step size of 0.1μm along horizontal.

Typical Raman spectra at ON, and OFF of the waveguide are shown in Fig.5.2 for G peak and Fig 5.3 for 2D peak position, respectively. These clearly reveal the up-shift in peak frequency where the graphene sits on the underlying silicon waveguide structure.

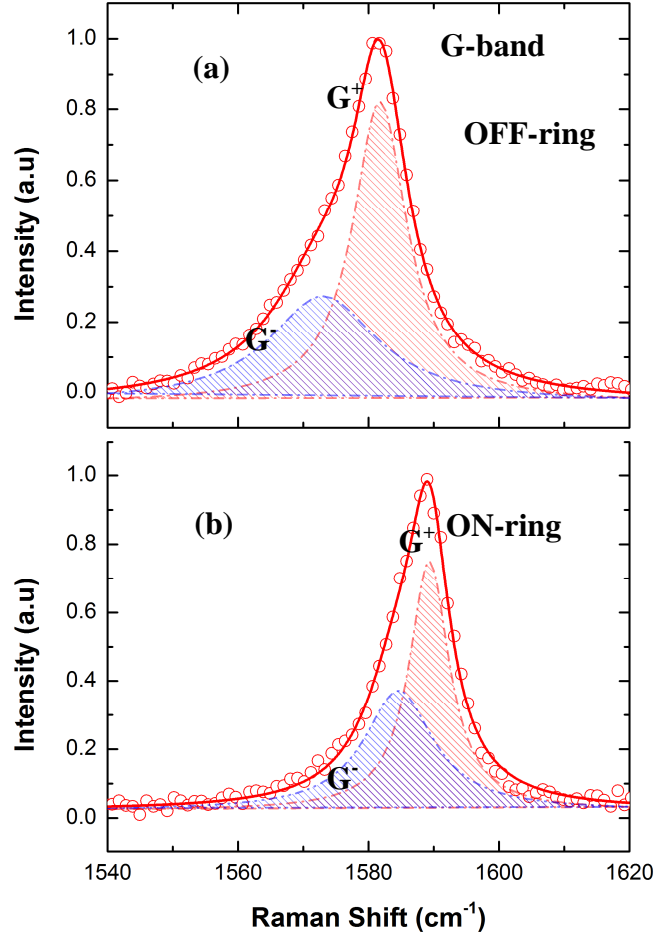
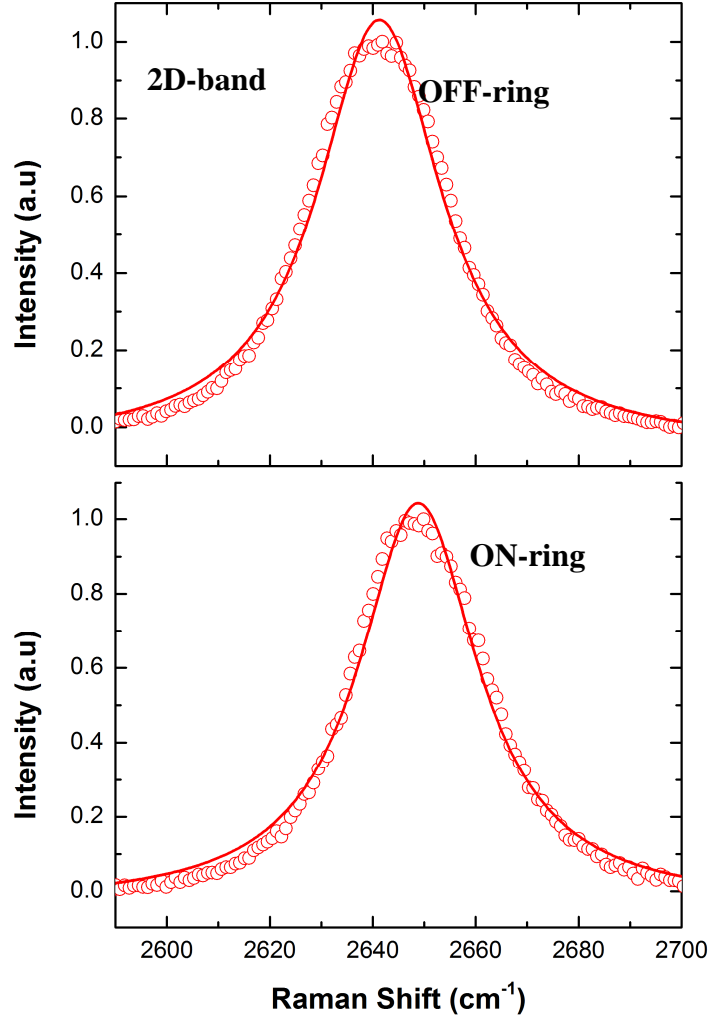


Figure 5.2 Typical Graphene G Raman peaks the underlying silicon MRR waveguide structure (a) OFF ring, and (b) ON ring. Lines represent double Lorentzian fits to the measured data. The asymmetry in the G-peak as a result of the lowering of the degeneracy of the in-plane  $E_{2g}$  optical phonon and these distinct scattering modes are labelled  $G^+$  and  $G^-$ .



**Figure 5.3 Typical 2D Raman peaks the underlying silicon ring waveguide structure (a) OFF-ring, and (b) ON-ring. Red lines represent single Lorentzian fits to the measured data.**

The 2D-peak is generally well described by a symmetric Lorentzian function, a signature of single layer graphene[8]. Rather we found here that the fit to the 2D peak was slightly better described by a pseudo-Voigt function, which suggests a small contribution to broadening from the instrument. No measurable change (beyond the standard error) in the FWHM of the 2D peak ( $\Gamma_{2D} \sim 32\text{cm}^{-1}$ ) was observed between ON- and OFF-ring data indicating an insensitivity of this to carrier concentration, consistent with previous observations [26].

On the other hand, the G peak is rather asymmetric for both OFF- and ON-ring spectra and, as a result, is not well described by a symmetric single Lorentzian function. It was

found that best described ( $R^2 > 0.995$ ) by a *double* Lorentzian line-shape, indicative of two distinct scattering processes. We observe that the width of the main ( $G^+$ ) peak decreases by  $\sim 25\%$   $\Gamma^+(G)$  from  $\sim 10\text{cm}^{-1}$  to  $\sim 7.5\text{cm}^{-1}$  as we go from OFF- to ON-ring condition. This is consistent with theoretical predictions and prior observations of the ‘stiffening’ of the graphene  $E_{2g}$  optical phonon, as a result of doping [8]. The second underlying scattering mode ( $G^-$ ), responsible for the asymmetry, also exhibits a much more significant decrease in width of  $\sim 35\%$   $\Gamma_G^-(G)$  from  $\sim 20\text{cm}^{-1}$  to  $\sim 13\text{cm}^{-1}$  as we go from the suspended graphene to where the graphene sits on the cavity waveguide structure. Asymmetry in the graphene Raman G-peak has previously been attributed to highly localised charge inhomogeneity within the laser probe area [26], i.e. on the sub-micron scale and it has also already been observed when comparing Raman spectra of suspended graphene with that supported by a substrate [22]. Recent studies of graphene supported by nanostructured surfaces [27] have also revealed a multi-peak fine-structure in the G-band, which was interpreted as being the result of extreme curvature or ‘wrinkling’, similar to what is observed in single wall carbon nanotubes. In this case, the doubly degenerate in-plane  $E_{2g}$  optical mode can be split between phonons along the nanotube axis,  $\omega_G^+$  and those that are perpendicular to it,  $\omega_G^-$  with the degree of splitting,  $\Delta\omega_G = \omega_G^+ - \omega_G^-$  being a strong function of the nanotube size (i.e. degree of curvature), even in the absence of any externally applied strain [28]. G-peak splitting has also been observed in graphene under uniaxial strain [5] and in isolated Carbon nanotube’s under hydrostatic pressure [29] where the curvature-sensitive lower frequency ( $G^-$ ) scattering mode itself can be broadened and even split when nanotubes buckle and collapse under high pressure loading. We note from fitting the graphene G-band spectra here that both the frequency difference  $\Delta\omega_G$  and the line-width of the  $G^-$  mode ( $\Gamma_{OFF}^-$ ) are greater for the suspended OFF-ring condition, than for the ON-ring case. In the absence of any evidence (from the peak positions) for a global net strain, we speculate that this may be the result of a localised out-of-plane ‘wrinkling’ in the suspended area, which is ‘smoothed’ out where the graphene is supported by the well-defined underlying waveguide structure of the MRR. Indeed, observations from cross-sectional AFM imaging reveal just such an out-of-plane ‘wrinkling’ effect in suspended graphene[30] whilst it tends to be highly conformal (principally as a result of Van der Waals forces) to underlying structures where it is

supported, which could explain the smaller  $\Delta\omega_G$  and narrower  $G^-$  peaks we observe where the graphene sits on the underlying silicon waveguide structure.

From line scans for both rings, we examined the ratio of peak intensities,  $I_{2D}/I_G$ , which is known to be carrier concentration dependent, being maximum for the intrinsic case and decreasing continuously with increasing (both  $n$  and  $p$ ) doping level, mainly because of a quenching of the 2D mode with increasing carrier-phonon scattering [22, 31].

However, as we observe measurable drop in  $I_{2D}/I_G$ , from  $\sim 3$  to  $\sim 2.5$  between where the graphene is suspended and where it sits atop the underlying silicon waveguide structure, we note that this change is small relative to the degree of  $G$  peak shift we observe, when compared with other reports [26] for the same excitation laser wavelength (633nm). It is worth pointing out though that in [26] there is a high degree of scatter in the data for  $I_{2D}/I_G$  as a function  $G$  peak position, which appears to increase with excitation wavelength, suggesting it may not be the most reliable indicator of doping level.

### 5.3.2. Raman areal peak position mapping

Optical images of the monolayer graphene samples are presented in Figs. 5.4 (a-b). To investigate changes induced shift of the  $G$ , and 2D peak positions at different points along the racetrack resonators, we collected Raman spectra from within the dashed boxes shown in Figs. 5.4 (a-b).

Detailed Raman areal  $G$  peak position maps corresponding to the dashed areas in Fig. 5.4(a), for the cavities of radius  $10\mu\text{m}$  are shown in Figs.5.4(c). It can be seen that the  $G$  peak position is red shifted meaning there is an increase in the wavenumber shift (Fig.5.4c). The position of the  $G$  peak was found with approximately an average shift between ON ring and OFF ring of  $\sim 11\text{cm}^{-1}$ , where the graphene sits on the waveguide structure.

Similarly Figs. 5.4(d), show Raman mapping of the 2D peak position measured from that of the dashed boxes in Figs.5.4(b). In this Fig, the 2D peak position was up-shifted by  $\sim 8\text{cm}^{-1}$  ( $2640\text{-}2648\text{cm}^{-1}$ ), moving from ON ring to OFF ring.

The Raman shift of G and 2D modes can be associated with the impurities or doping effects, strain or a combination of these in the graphene layer. However, in the low strain limit (where there is no splitting of the G peak), the strain related shift of the 2D peak is well-known to be approximately 6 times that of the G peak for a given strain [5]. However, we observe a close to equivalent shifts in Pos (G) and Pos (2D) where the graphene sits on top of the micro-ring waveguide structure. This indicates that the cause of the shift is due to strain. In comparison, the shift rate and direction of the G and 2D peak shifts with doping are highly specific to carrier type [25]. For electron and hole doping, the G peak positions ( $\omega_G$ ) always increases from the origin value, meaning that a plot of G peak position with Fermi level is nearly symmetric about zero. However, for the 2D peak, the frequency ( $\omega_{2D}$ ) is up-shifted significantly for a moderate increase in the hole doping level ( $\sim 15\text{cm}^{-1}$  for  $3 \times 10^{13}\text{cm}^{-2}$ ), it remains almost unchanged from its origin frequency up to an electron concentration of  $\sim 3 \times 10^{13}\text{cm}^{-2}$ , above which it down-shifts rapidly. This leads to a highly asymmetric curve for the 2D peak position with Fermi level about zero. That we observe shift rates that are both same in magnitude and in the same direction for the G and 2D peaks strongly reveals that the graphene is moderately hole doped, where it sits on top of the waveguide structure, compared to where it is suspended over the cavity resonator. In order to quantify this effect, we used the following relations (Eq. 5.1 and 5.2) which extracted from data introduced in previous work [24] to evaluate the approximate Fermi level shift from the shift ( $\Delta\omega$ ) of G and 2D peak positions, after [24].

$$|E_F| \times 41.5 = \Delta\omega_G = \omega_G - \omega_{0(G)} \quad (5.1)$$

$$|E_F| \times 31.5 = \Delta\omega_{2D} = \omega_{2D} - \omega_{0(2D)} \quad (5.2)$$

Where  $\omega_{0(G)}$  is the G peak position ( $1580\text{cm}^{-1}$  [26] and  $\omega_{0(2D)}$  is 2D peak position and  $2640\text{cm}^{-1}$  with a laser of 633 nm [9] respectively) of equilibrium graphene (unstrained, intrinsic),  $\omega_G$  and  $\omega_{2D}$  are the absolute wavenumber measured experimentally at each point of G and 2D peak positions in units of  $\text{cm}^{-1}$ , and  $E_F$  is the Fermi level in units of eV. In Fig. 5.4 (e, f) we show the correlation of G and 2D position derived from the data of Fig. 5.4 (c, d) with Fermi level using (Eq. 5.1 and 5.2). These are mostly equivalent, indicating that the suspended graphene is intrinsic ( $E_F \sim 0$ ) but that the hole is increased

slightly (yielding  $E_F \sim -0.2\text{eV}$ ) where the graphene sits atop the waveguide structure. A similar analysis of a micro-ring resonator with radius,  $r = 20\mu\text{m}$  shown in Fig. 5.5 provided similar result. This result indicates that the effect is not dependent on the device size, but it is only a material dependent doping effect.

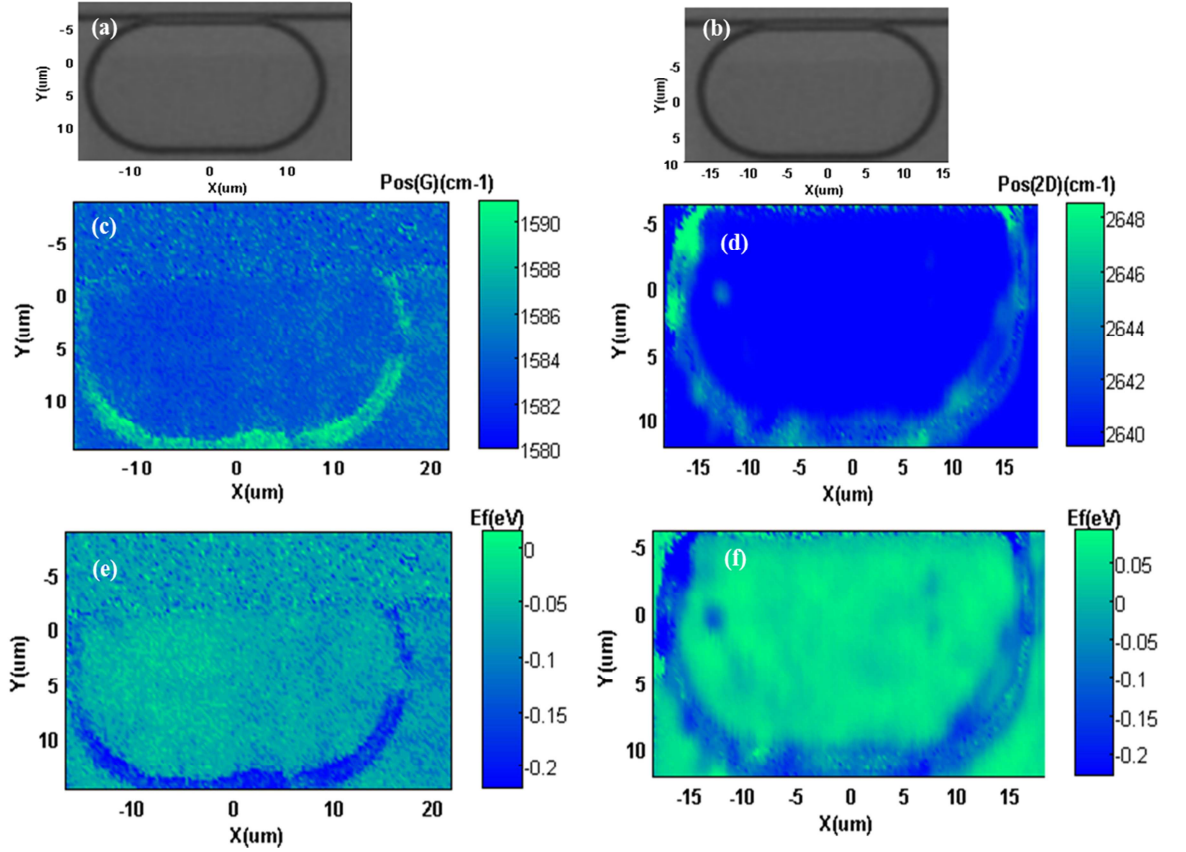


**Figure 5.4 (a, b) Optical images of the graphene coated,  $10\mu\text{m}$  radius micro-ring resonator, (c, d) Raman mapping area of the G and 2D peak position, respectively and (e, f) Raman mapping area of Fermi level determined from the G and 2D peak positions and Eq. (5.1, 5.2)**

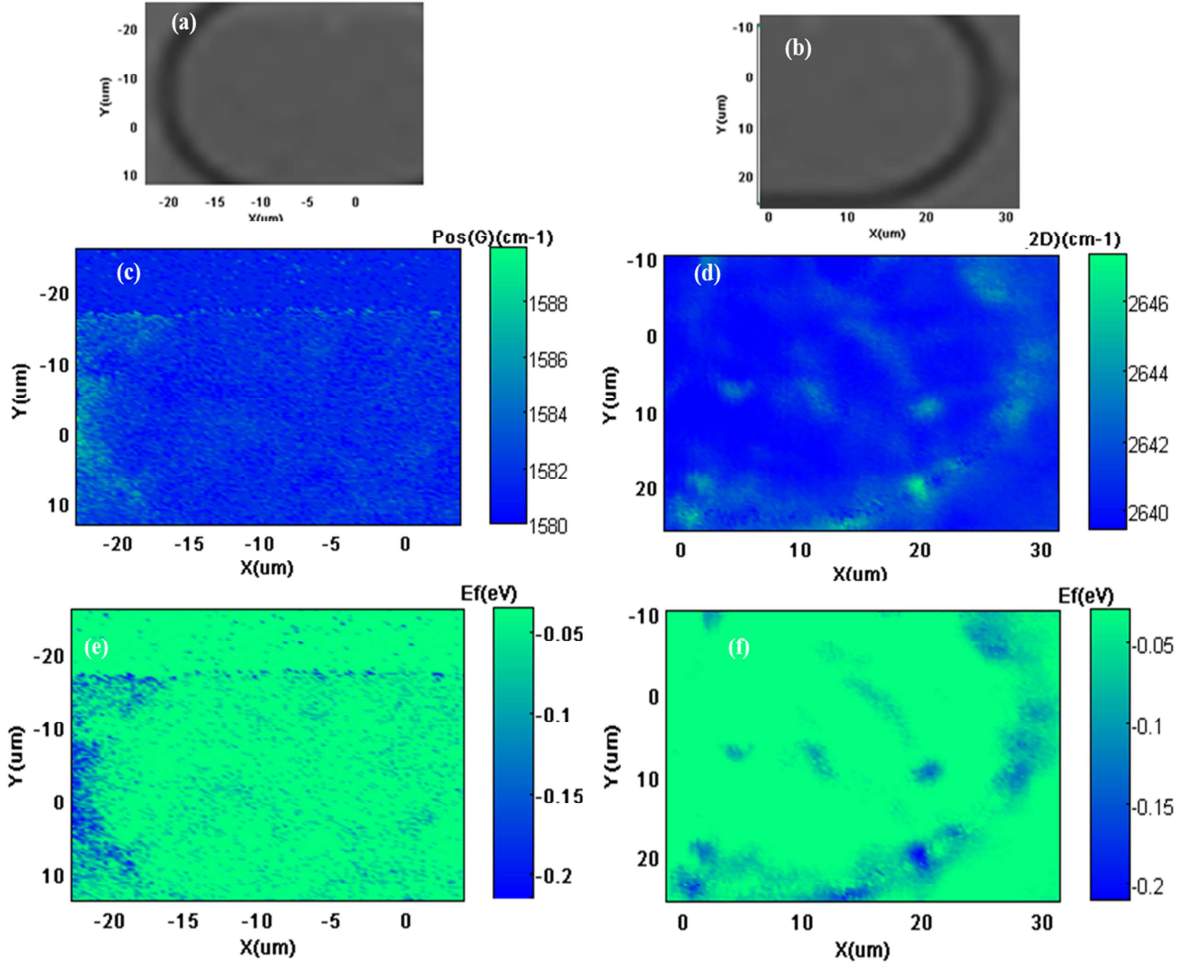


**Figure 5.5** Optical images of the graphene coated, 20μm radius micro-ring resonator, (c, d) Raman mapping area of the G and 2D peak position, respectively and (e, f) Raman mapping area of Fermi level maps determined from the G and 2D peak positions and Eq. (5.1, 5.2).

To throw more light on the doping the ratio of the total integrated peak intensities,  $A_{2D}/A_G$  was analyzed as this covers the variations in intensity ratio ( $I_{2D}: I_G$ ), and the full width of half maximum of 2D and G mode can be used to obtain the carrier concentration directly from Eq. (5.3) [22,31]:

$$\sqrt{\frac{A_G}{A_{2D}}} = C \left[ \gamma_{e-ph} + |E_F| f\left(\frac{e^2}{\epsilon v_f}\right) \right] \quad (5.3)$$

Where  $\gamma_{e-ph}$  is the average electron-phonon scattering rate, previously determined in [31] to be ~33meV,  $C$  is a constant,  $e$  is the electronic charge, the dielectric constant of



the SiO<sub>2</sub> used in the analysis,  $\epsilon(\sim 4)$  [32], which is assumed to be present at the interface (as a native oxide layer) between the silicon and graphene. This gives  $f(e^2/\epsilon v_f) \sim 0.069$  where  $v_f$  is the electron velocity,  $\sim 1.17 \times 10^8$  cm/s. Our measuring results of the area ratio of G and 2D peak positions indicate that  $\frac{A_{2D}}{A_G}$  is lower on the waveguide structure compared to the central suspended area, again supporting the hypothesis that the observed shifts of Raman spectra are the result of a substrate doping effect. Fig. 5.6 reveals the Fermi level that we obtained from the area ratio of the graphene G and 2D peaks and Eq. (5.3) as a function of the position along line scans for the two micro-ring device structures, with  $r = 10$  and  $20 \mu\text{m}$  radius. The maxima in the Fermi level shift,  $|E_F|_{\text{max}} \sim 0.2 \text{ eV}$  is confirmed where the graphene sits on the underlying silicon waveguide structure, in agreement with that we have determined from the peak shifts and previous reports [17]. It is worth mentioning that, even though the different size MRR's coated with graphene we have studied, which leads to a larger region of suspended graphene over the  $20 \mu\text{m}$  radius MRR structure compared with the  $10 \mu\text{m}$  radius structure ( $\sim 54 \mu\text{m}$  suspended compared with  $\sim 36 \mu\text{m}$ , respectively), the local spatial doping pattern is virtually identical, as revealed by the Gaussian fits in Fig. 5.6.

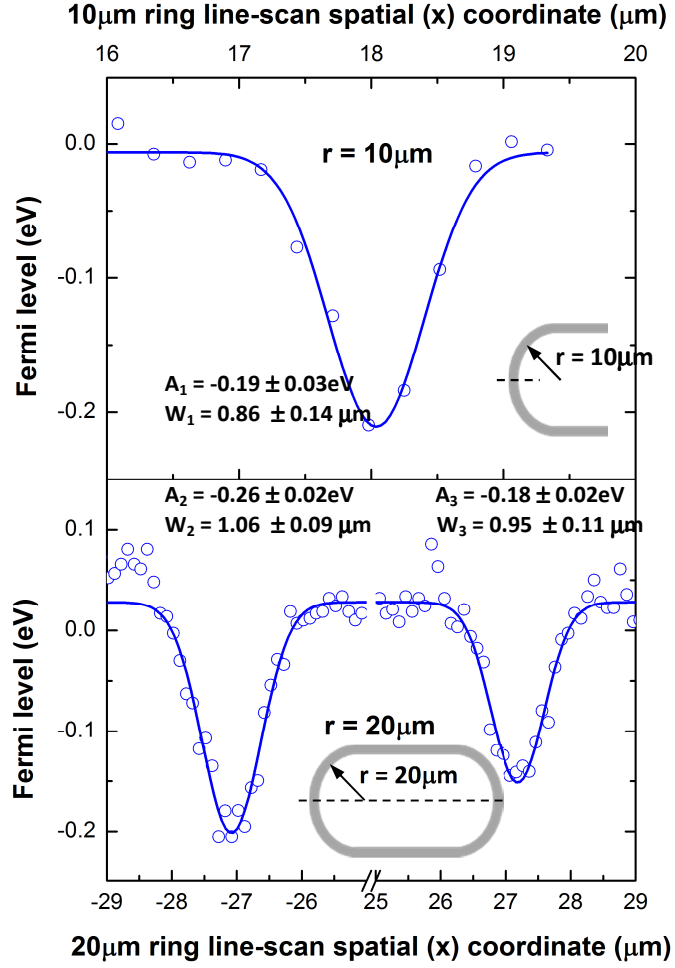


Figure 5.6: The Fermi level determined (from  $\sqrt{\frac{A_G}{A_{2D}}}$ ) as a function of spatial coordinate along the mapping line scans for 10μm cavity (top), and (bottom) 20μm radius cavity. Blue line is Gaussian fitted peak integrated areas and widths are shown for comparison along with the line-scan measured data.

Converting the Fermi level we have determined to a carrier concentration,  $n$  through Eq. (5.4) [32] yields a peak value for  $n \sim 3 \times 10^{12} \text{ cm}^{-2}$  on the cavity structure, which is in generally good agreement with previous reports [25]:

$$n = \left( \frac{E_F}{\hbar v_F} \right)^2 / \pi \quad (5.4)$$

Finally, we examined the correlation between the G and 2D peak positions from our three line-scans measured data in a so-called vector decomposition plot, introduced by Lee *et al* [33], Fig. 5.7.

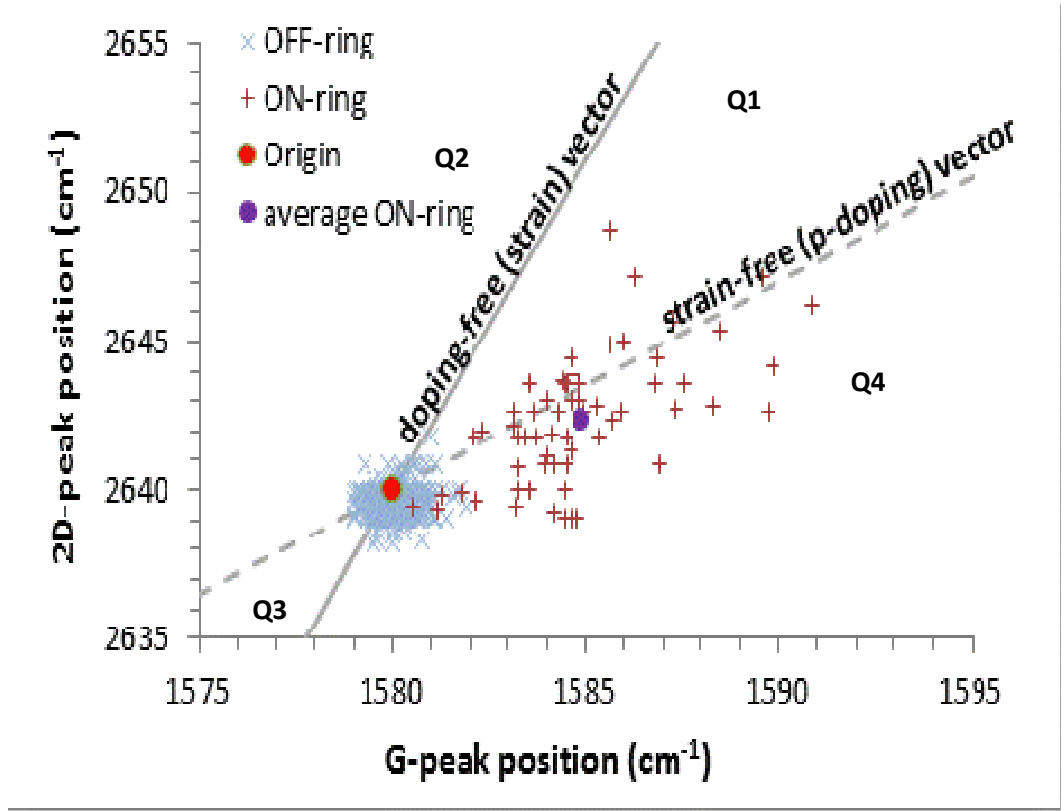


Figure 5.7 correlation plot showing data for three line-scan measurements across the graphene integrated ring resonator. The red crosses are 2D and G frequency points ON-ring structure with the purple dot representing the average of these values and the blue crosses are 2D and G frequency points 'OFF' the ring where the graphene is suspended across the ring resonator. The red dot is freestanding values (unstrained, intrinsic) for graphene with 633nm laser that defines the origin in the plot. The solid line denotes the doping free (strain) vector with  $\Delta\omega_{2D}/\Delta\omega_G \sim 2.2$ , after and the dashed line denotes the strain-free (p-doping) vector with  $\Delta\omega_{2D}/\Delta\omega_G \sim 0.7$  [33].

The aim is to be able to attribute every measured pair of  $\omega_G$  and  $\omega_{2D}$  to a value of strain and doping according to a simple vector model as depicted in [33]. This is based on the fact that the rate of variation in peak position ratios depends on whether the shifts are dominated by strain ( $\Delta\omega_{2D}/\Delta\omega_G \sim 2.2$ ) or doping ( $\Delta\omega_{2D}/\Delta\omega_G \sim 0.7$ ) [33]. Therefore, any frequency point in the 2D-G axis can be decomposed into strain and p-type doping unit vectors. As increasing (decreasing) strain or doping, the values of  $(\omega_G, \omega_{2D})$  will move from the origin coordinate along strain" lines corresponds to increasing compressive (tensile) strain, or along "doping" line corresponds to increasing (decreasing) p doping. The 2D-G axis is divided into four quadrants (Q1–Q4) by the gradient for unit vectors

for strain (2.2) and doping (0.7), respectively. When data points of G, and 2D frequency scatter over Q1(Q4), this is attribute that the shift of the peak positions are the result of a combination of compressive (tensile) strain and strongly hole doped. Whereas scattering data points over Q2 and Q3 are forbidden because hole doping only increases in the  $\omega_G$  frequency.

In Fig. 5.5, the unstrained, intrinsic values of graphene peak position were adapted as the origin for correlated 2D-G coordinate (red dot) [9, 25], The dashed line passing through the origin indicates unit vector for strain-free (p-doping) and the slope denoting the doping-free (strain) is the solid line [29]. Data points scattered around the origin from three line-scans for OFF micro-ring but that data points along the strain-free (p-doping) vector for ON-micro-ring with the average ON-ring coordinate value (purple dot) being (1584.9, 2642.4). The increased scatter data points where the graphene sits ON the MRR structure along the strain-free line indicates a greater range of doping levels observed from the relative peak shifts, possibly due to the uncertainty in probing a highly localised substrate doping effect produced by the underlying, sub-micron waveguide width, compared with the probe laser spot size ( $>1\mu\text{m}$ ). Despite the apparent scatter in the data, into both Q4 and Q1, we discount any significant global strain effects because the average ON-ring coordinate lies so close to the strain-free line. We suggest that the shift rates we observe as result of silicon substrate induced hole-doping and the average value of G-2D axis at ON-ring confirms this to be in the range of  $(2 \text{ to } 3) \times 10^{12} \text{cm}^{-2}$ .

## 5.4. Conclusion

In summary, the characterization of monolayer graphene after integration on silicon strip waveguide based MRRs using Raman mapping technique to study the effect of graphene transfer process on its properties is demonstrated for the first time. Raman peak shifts and integrated intensities of the characteristic graphene Raman G and 2D peaks were determined for mapped area and correlated to the Fermi level. The shift rate of Raman peak indicate a Fermi level where the graphene sits on the silicon waveguide as a result of unintentional hole-doping from the underlying silicon/SiO<sub>2</sub> waveguide (substrate doping effect). The data for the OFF-ring area reveals no measurable distinction from intrinsic graphene but for ON-ring region, a maximum shift of the Fermi level of  $\sim 0.2\text{eV}$  is determined, which corresponds to a peak hole concentration of  $\sim 3 \times 10^{12}\text{cm}^{-2}$ . The result agrees with the reported literature values of  $E_F$  of  $\sim 0.23\text{ eV}$  for the integration of CVD graphene onto silicon (MZI) based waveguide using back gating [17]. An asymmetry in the Raman G peak, which varies according to whether the graphene is suspended or supported, indicates a combination of doping induced 'stiffening' and lifting of the degeneracy of the  $E_{2g}$  optical mode. These effects should be taken into account when graphene is combined with silicon photonic platform, certainly when attempting to use such platform to determine graphene's characteristic properties for optimization of future graphene integrated silicon photonic devices, such as optical modulators and sensors. The researchers in photonics and optoelectronic fields would take these results into consideration during designing devices for different applications such as photo-detectors, bio/or gas sensors, modulators, and polarizers.

## 5.5. References

1. Park, M.K., et al., Label-free aptamer sensor based on silicon microring resonators. *Sensors and Actuators B: Chemical*, 2013. **176**: p. 552-559.
2. Kou, R., et al., Influence of graphene on quality factor variation in a silicon ring resonator. *Applied Physics Letters*, 2014. **104**(9): p. 091122.
3. Guo, Q., et al., Silicon-on-glass graphene-functionalized leaky cavity mode nanophotonic biosensor. *Acs Photonics*, 2014. **1**(3): p. 221-227.
4. Malard, L., et al., Raman spectroscopy in graphene. *Physics Reports*, 2009. **473**(5): p. 51-87.
5. Mohiuddin, T., et al., Uniaxial strain in graphene by Raman spectroscopy: G peak splitting, Grüneisen parameters, and sample orientation. *Physical Review B*, 2009. **79**(20): p. 205433.
6. Stampfer, C., et al., Raman imaging of doping domains in graphene on SiO<sub>2</sub>. *Applied Physics Letters*, 2007. **91**(24): p. 241907.
7. Cançado, L.G., et al., Quantifying defects in graphene via Raman spectroscopy at different excitation energies. *Nano letters*, 2011. **11**(8): p. 3190-3196.
8. Ferrari, A.C., Raman spectroscopy of graphene and graphite: disorder, electron-phonon coupling, doping and nonadiabatic effects. *Solid state communications*, 2007. **143**(1): p. 47-57.
9. Pan, W., et al., Biaxial compressive strain engineering in graphene/boron nitride heterostructures. *Scientific reports*, 2012. **2**.
10. Androulidakis, C., et al., Experimentally derived axial stress-strain relations for two-dimensional materials such as monolayer graphene. *Carbon*, 2015. **81**: p. 322-328.
11. Stojanović, D., et al., Raman spectroscopy of graphene: doping and mapping. *Physica Scripta*, 2013. **2013**(T157): p. 014010.
12. Childres, I., et al., Raman spectroscopy of graphene and related materials. *New developments in photon and materials research*, 2013. **1**.
13. Popov, V.N. and P. Lambin, Theoretical Raman intensity of the G and 2D bands of strained graphene. *Carbon*, 2013. **54**: p. 86-93.
14. Froehlicher, G. and S. Berciaud, Raman spectroscopy of electrochemically gated graphene transistors: Geometrical capacitance, electron-phonon, electron-electron, and electron-defect scattering. *Physical Review B*, 2015. **91**(20): p. 205413.
15. Ferreira, E.M., et al., Evolution of the Raman spectra from single-, few-, and many-layer graphene with increasing disorder. *Physical Review B*, 2010. **82**(12): p. 125429.
16. Pimenta, M., et al., Studying disorder in graphite-based systems by Raman spectroscopy. *Physical chemistry chemical physics*, 2007. **9**(11): p. 1276-1290.
17. Li, H., et al., Optical absorption in graphene integrated on silicon waveguides. *Applied Physics Letters*, 2012. **101**(11): p. 111110.
18. Crowe, I.F., et al., Determination of the quasi-TE mode (in-plane) graphene linear absorption coefficient via integration with silicon-on-insulator racetrack cavity resonators. *Optics express*, 2014. **22**(15): p. 18625-18632.
19. Cai, H., et al., Enhanced linear absorption coefficient of in-plane monolayer graphene on a silicon microring resonator. *Optics express*, 2016. **24**(21): p. 24105-24116.
20. Kou, R., et al., Characterization of optical absorption and polarization dependence of single-layer graphene integrated on a silicon wire waveguide. *Japanese Journal of Applied Physics*, 2013. **52**(6R): p. 060203.

21. Li, X., et al., Large-area synthesis of high-quality and uniform graphene films on copper foils. *Science*, 2009. **324**(5932): p. 1312-1314.
22. Ferrari, A.C., et al., Raman spectrum of graphene and graphene layers. *Physical review letters*, 2006. **97**(18): p. 187401.
23. Kim, K., et al., Raman spectroscopy study of rotated double-layer graphene: misorientation-angle dependence of electronic structure. *Physical review letters*, 2012. **108**(24): p. 246103.
24. Das, A., et al., Monitoring dopants by Raman scattering in an electrochemically top-gated graphene transistor. *Nature nanotechnology*, 2008. **3**(4): p. 210-215.
25. Caridad, J.M., et al., Effects of particle contamination and substrate interaction on the Raman response of unintentionally doped graphene. *Journal of Applied Physics*, 2010. **108**(8): p. 084321.
26. Casiraghi, C., et al., Raman fingerprint of charged impurities in graphene. *Applied Physics Letters*, 2007. **91**(23): p. 233108.
27. Vejpravova, J., et al., Graphene wrinkling induced by monodisperse nanoparticles: facile control and quantification. *Scientific reports*, 2015. **5**.
28. Paiva, T. and R.R. dos Santos, Charge-density waves in one-dimensional Hubbard superlattices. *Physical Review B*, 2002. **65**(15).
29. Sun, Y., et al., Resonance Raman spectroscopy of carbon nanotubes: pressure effects on G-mode. *High Pressure Research*, 2014. **34**(2): p. 191-197.
30. Berger, C.N., M. Dirschka, and A. Vijayaraghavan, Ultra-thin graphene-polymer heterostructure membranes. *Nanoscale*, 2016. **8**(41): p. 17928-17939.
31. Basko, D., S. Piscanec, and A. Ferrari, Electron-electron interactions and doping dependence of the two-phonon Raman intensity in graphene. *Physical Review B*, 2009. **80**(16): p. 165413.
32. Yin, Y., et al., Graphene, a material for high temperature devices—intrinsic carrier density, carrier drift velocity, and lattice energy. *Scientific reports*, 2014. **4**.
33. Lee, J.E.e.a., Optical separation of mechanical strain from charge doping in graphene. 3:1024 doi: 10.1038/ncomms2022 (2012).





## **Chapter 6: Investigation of the light absorption in graphene oxide incorporated into hybrid silicon slot waveguide based ring resonators**

### **6.1. Introduction**

Graphene oxide is, in a sense, a chemical derivative of graphene, which shows additional properties compared to graphene such as ease of processing in solutions, ultrahigh sensitivities and ultra-fast sensing of gas molecule adsorption because of its one-atom thickness[5,6] and extremely high surface-to-volume ratio, also it has enhanced water solubility compared to graphene because it contains hydrophilic oxygen groups [7, 8] which occur widely in bio-chemical systems[9].

CVD is the most widely used synthesis method for graphene, and its incorporation into silicon photonic devices to enhance device performance has been already demonstrated in the Manchester group and elsewhere [10-12]. However, the very high value of the in-plane optical absorption of monolayer graphene makes it undesirable for bio/gas sensing [13-16], furthermore, the difficulty of transferring CVD graphene layers from their initial growth substrate to the waveguide makes scaling the device manufacture a problem. On the other hand, graphene oxide (GO) is an alternative material for graphene coating due to its ability to be processed in solutions, also it can be synthesized from graphite by low-cost and simple processes, and can readily be produced in very stable dispersions using various organic solvent [17]. The absorption efficiency of GO material when coated on optical devices, although much less than graphene, may be still a limiting factor that needs to be considered while designing optical bio, or gas sensors for applications. The absorption efficiency of GO has been widely investigated in the solution form and different values have been reported[18, 19] the optical absorption of GO on silicon photonic devices is still little known due to the limited practical applications of it in solution form. In terms of solutions a constant value of  $2460 \text{ mL} \cdot \text{mg}^{-1} \cdot \text{m}^{-1}$  in different organic solvents has been reported for the GO absorption coefficient [20]. In addition, the same workers have given  $\alpha$  values measured at 660 nm for series of dispersions at different concentrations from 1390 to 6600  $\text{mL} \cdot \text{mg}^{-1} \cdot \text{m}^{-1}$  [19]. An extinction coefficient of  $6150 \text{ mL/mg} \cdot \text{m}^{-1}$  of GO at 230nm

has been determined in biological solutions [21]. Thus a wide range of  $\alpha$  value has been reported depending on the concentration of the GO solution.

Recently, GO has been successfully integrated onto non-silicon waveguides. Chang et al. [22] have demonstrated the integration of GO onto polymer waveguide polarizer to study the effects of the absorption of TE-polarized light by multilayer GO films on the optical characteristics using evanescent field coupling [7,22]. Motivated by the recent progresses reported for GO integrated optical, and electrochemical devices, and due to its high reactivity which can improve the chemical sensing performance, here we demonstrate the use of graphene oxide (GO) to enhance the device performance in a GO-on-SOI MRRs. The first step for building GO-on-SOI MRRs devices was to determine the strength of the graphene oxide light interaction. Therefore, it is of great importance to study the optical absorption efficiency of light propagating along with GO incorporated into cavity resonators, which will give a better understanding on practical limitation of such devices and enable more post processing in chemical sensing.

In this chapter, we demonstrate waveguide-graphene oxide structures, by coating different GO concentrations onto silicon MRRs. We present the optical characterization of uncoated and different GO coated MRRs in TE-polarized mode and report on the measured characteristics of the each device. This characterization provides an essential understanding of the optical behaviours of such devices, and will be built on in subsequent chapters concerning sensing using graphene oxide-integrated SOI MRRs. The main objective of this work is to evaluate the performance (the highest Q factor possible with different GO coating) of the cavities for use as the sensing element in bio and vapour/gas sensing. The aim was to get the highest possible Q value and enable the detection of very small shifts in the cavity resonant wavelength, which is desirable for chemical sensing applications.

## **6. 2.Experimental details**

### **6. 2.1. Sample layout**

The sample consisted of the devices already described for the graphene experiments with a 1.6  $\mu\text{m}$  window etched through cladding layer, a coupling gap  $g = 0.2\mu\text{m}$  and a radius of curvature,  $r = 25\mu\text{m}$ . The devices had built into them a 150 nm thick Titanium nitride (TiN) contact and heating elements. Before we performed any cleaning on the

sample we performed initial measurements of the sample as delivered chip. Then the sample was cleaned thoroughly to remove any polymethylmethacrylate (PMMA layer), as well as any contaminants or particles. The sample were first sonicated in acetone for 10 minutes, before being immersed in ethanol solution for more 10 minutes, then washed with DI water and dried with nitrogen.

### **6.2.2. Preparation of GO incorporated cavity resonators**

GO coated cavity resonators were fabricated by the spin coating technique. The concentrations of GO spun onto the cavity resonators was adjusted to be 0, 1, 1.4, 2, 3, 4mg/mL by volume of GO suspensions, respectively. In detail, a measured amount of 4mg/ml GO solution was first dissolved into the DI water, followed by ultrasonic bath for 30 min to form a homogeneous and transparent solution. Then it was cast into cavity resonators using a micropipette and spun coated at 1500rpm for 30s individually to cover not only the ring resonators but also the waveguide and grating coupler region. Subsequently, the chip is annealed at 40 C<sup>0</sup> until the GO solution was dried and left overnight at room temperature.

## **6.3. Structure characterization and results**

### **6.3.1. SEM scanning characterization**

The surface morphology of the GO films coated on cavity resonators was characterised by using a scanning electron microscope (SEM FEI quanta200). Micrographs of the morphology were taken without coating with any layer and after coating. The micrographs were taken in high vacuum mode with 20 kV acceleration voltages and a medium spot size.

Fig 6.1(a) shows an SEM image of a bare silicon ring resonator. The SEM images of the five different concentrations patterned onto the ring resonator devices are shown in Figs.6.1(b-f). The SEM images clearly show that the GO is effectively coated onto the whole device surface. The surface morphology resembles a strongly folded texture with increasing GO concentration, which indicates that GO sheets are overlapped rather than aggregated, and the surface seems to have an inhomogeneous texture (rough surface), although lower concentrations have a more uniform appearance and also appear produce thinner layers as shown in Fig.6.1(b) for 1mg/ml concentrations,

Raman spectroscopy was used to confirm that the graphene oxide is completely coating the surface.

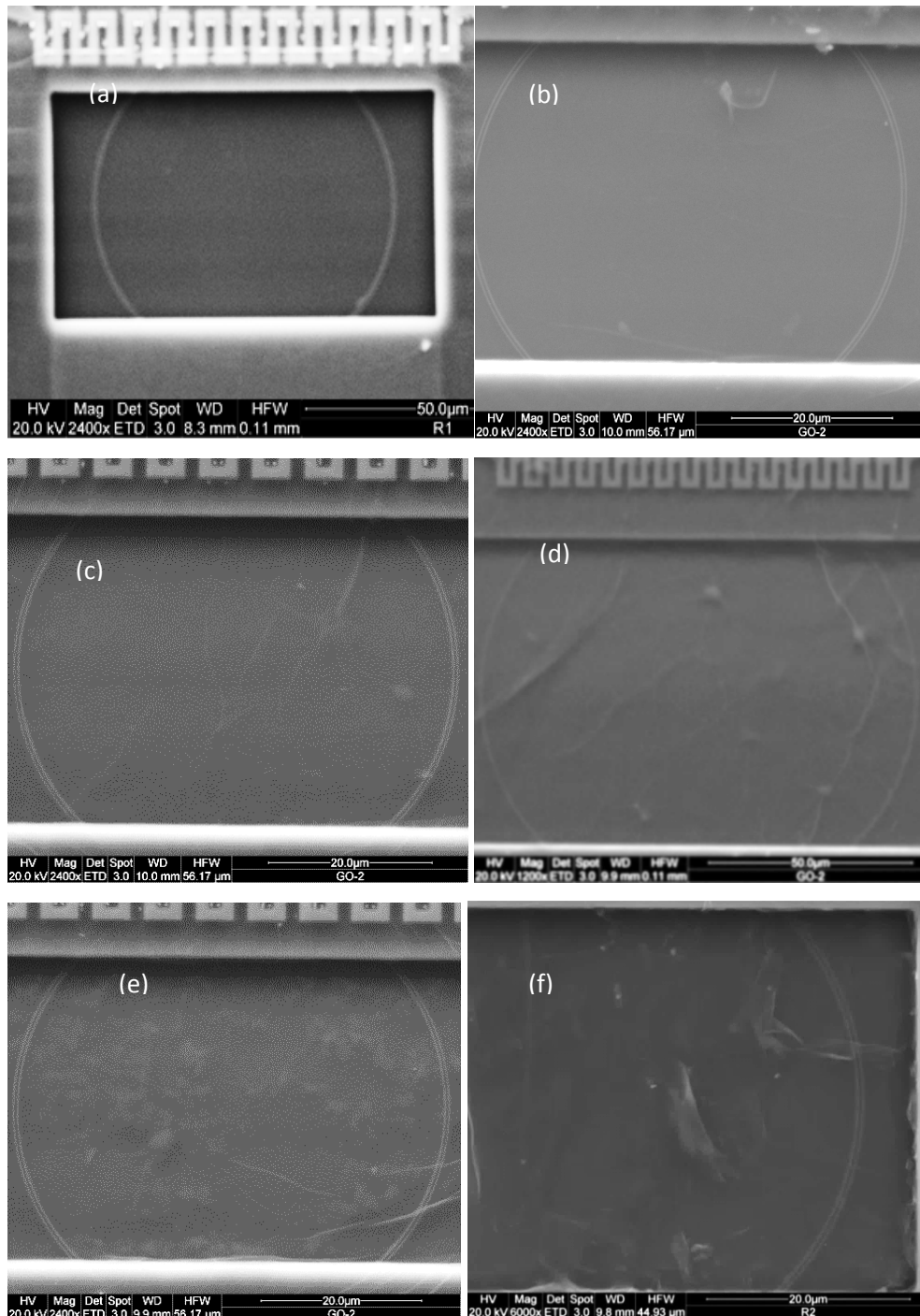


**Figure 6.1(a) SEM image of uncoated silicon ring resonator, (b-f) scanning electron microscope images of the silicon ring resonator coating with different GO concentrations**

### 6.3.2. Raman Spectroscopy characterisation and results

Raman spectroscopy used to characterise the surface in the same manner as for the graphene coated samples. Fig.6.2 shows the Raman spectra of three different GO concentrations. The Raman spectrum of a graphene oxide material is usually characterized by two distinct peaks a strong and broad D-band occurring at  $1350\text{ cm}^{-1}$ , which is assigned to local defects and thus is equivalent to the disordered mode of graphene[24,25], and the G peak ( $\sim 1595\text{ cm}^{-1}$ ) which is very common for all 2d carbon forms and corresponds to first order scattering of E<sub>2g</sub> mode (of sp<sup>2</sup> bonded carbon atoms)[26,27]. As a result of the chemical oxidation of graphene process, the graphene long range structure is lost and this leads to the intensity ratio of D and G bands also being below 1 [28]. The characterization of three different GO concentrations shows the characteristic D band and G-band at  $1343$  and  $1598\text{ cm}^{-1}$ , respectively. Most significantly, the Raman spectra of three GOs, showing different D/G intensity ratios, with less GO concentration the intensity ratio ( $I_D/I_G$ ) was increased and this difference are due to their different defect density intensities[29]. The GO Raman spectra also shows the 2D band around  $2690\text{ cm}^{-1}$ , this peak is the second order of D band.

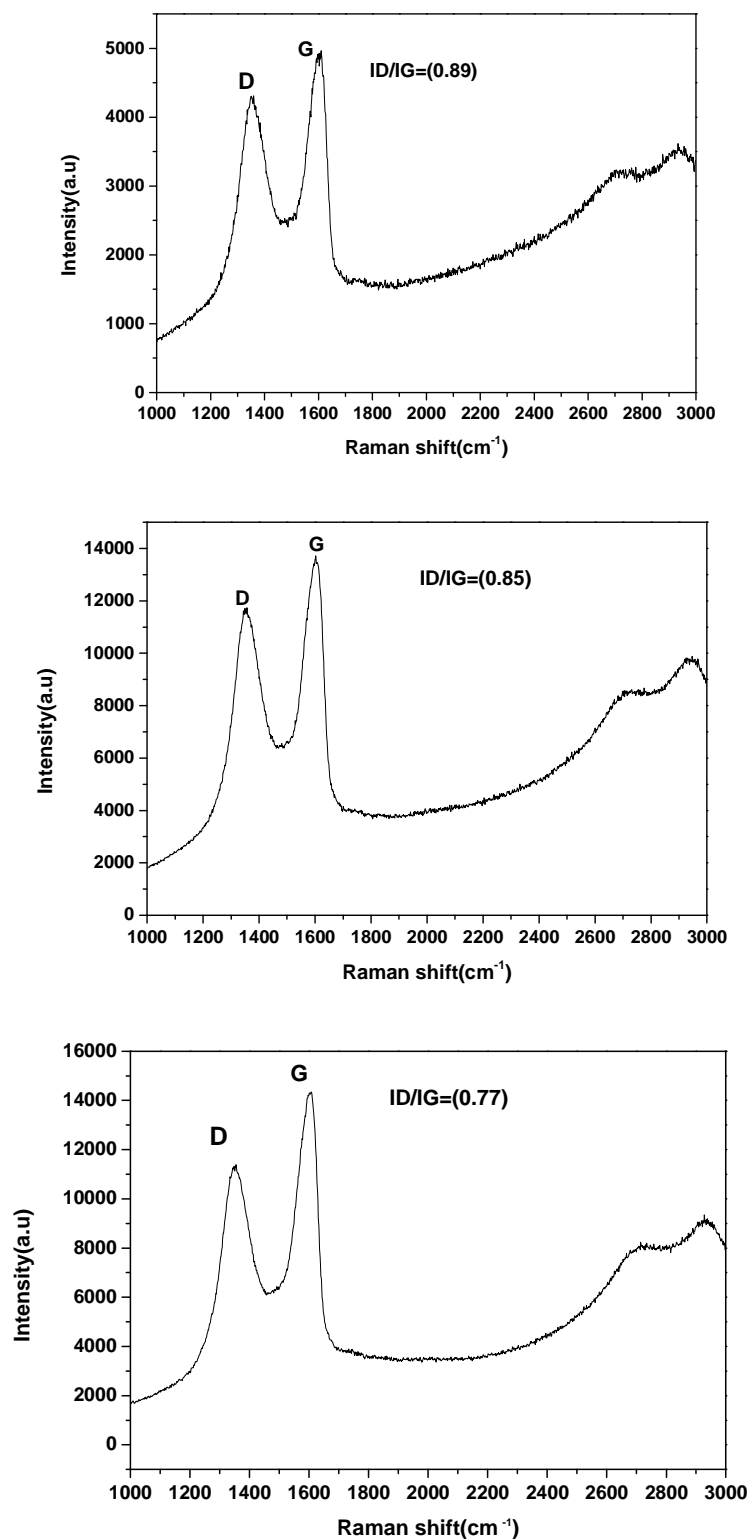


Figure 6.2 Shows the characterization of GO is obtained by Raman for 1, 1.4, and 2 mg/ml GO concentrations, spectra show D peak ( $\sim 1343\text{cm}^{-1}$ ), and G peak ( $\sim 1598\text{cm}^{-1}$ ).

## 6.4. Optical characterisation

The optical setup previously described was used to inject light into the RRs to determine the spectral response of the devices; the light source used was the superluminescent light emitting diode fibre source (SLED) and it was detected with the spectrum analyser and an infrared camera as discussed in section 3.4.3 (chapter 3). In the analysis of resonators the recorded spectra are normalized to the transmission spectrum of a single mode waveguide. In order to remove the Fabry-Perot reflections in this reference spectrum, it was smoothed by a convolution with a Gaussian window with a full width of half maximum 7. We measured the spectral characteristics of the devices for TE mode (electric field parallel to the waveguide surface)

## 6.5. Optical results and discussion

In order to determine how much light was absorbed by the graphene oxide incorporated into the slot waveguides of the ring resonator, we measured the transmission spectra from the through ports of a bare cavity resonator and set of GO concentrations coated cavity resonators as well as a theoretical model of normalized transmitted intensities were performed using eq. 2.10 in chapter 2 [30-33]. Using these equations, the quality factor for through port cavity can be approximated by[34]

$$Q = \left[ \frac{(2\pi n)}{\lambda_0} \right] \cdot \frac{(2\pi r)}{2 \cdot \arccos \left[ \frac{\left( 1 - \frac{4t}{\tau} + \left( \frac{t}{\tau} \right)^2 \right)}{\left( \frac{-2t}{\tau} \right)} \right]} \quad (6.1)$$

Where,  $t$  is the field transmission factor,  $\kappa$  is the field coupling factor to the waveguides which depend on the coupling efficiency of the ring resonator structure, and  $\tau$  is the attenuation of the field per round trip for a cavity respectively,  $\phi$  is the phase shift per round trip around the ring resonator, and  $L_{\text{eff}} = (2\pi r)$  is the total physical round-trip length of the cavity resonator,  $n$  is the effective refractive index.

By taking  $\tau$  from the fitting method presented in eq.2.10 the loss per round trip in the slot waveguide is:

$$\alpha = -10 \times \log_{10}(\tau) \quad (6.2)$$

And the propagation losses in slot waveguides can be estimated using following equation[34].

$$AC_{Si}(\text{dB}/\mu\text{m}) = \frac{-2 \times 10 \times \log_{10}(\tau)}{L(\mu\text{m})} \quad (6.3)$$

In our devices, the analysis of the optical, Raman mapping and SEM images, confirm that the entirety of the resonator is covered with graphene oxide. The total losses of waveguide coated with graphene oxide include the attenuation coefficient of the silicon waveguide-and graphene oxide structure (LAC). The  $LAC_{w(Si+Go)}$  of silicon waveguide coated with GO and can be written as

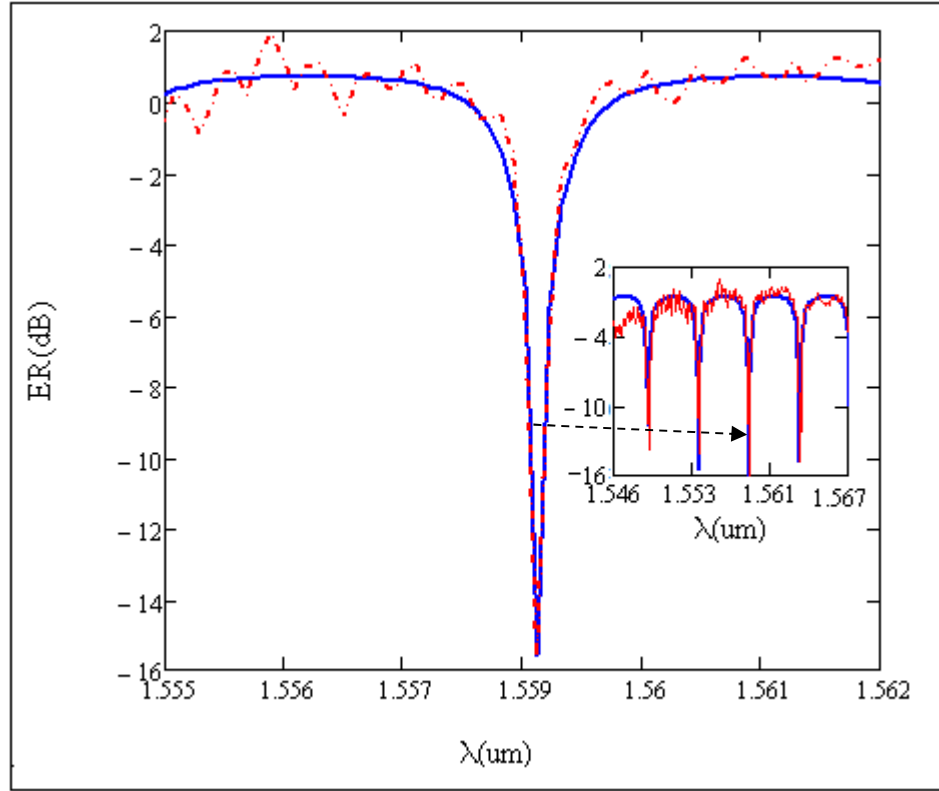
$$LAC_{w(Si+Go)} = \frac{(\alpha_{Si} - \alpha_{Go}(1-n))}{2\pi r n} \quad (6.4)$$

Where,  $\alpha_{Si}$  and  $\alpha_{Go}$  are the loss per round-trip for the bare and GO coated cavities respectively, and n is corrected of graphene oxide fractional coverage length. Hence, the linear absorption of graphene oxide on the silicon micro-ring resonator ( $\alpha_{GO\_Resonator}$ ) is expressed as:

$$\alpha_{GO\_Resonator} = LAC_{w(Si+Go)} - AC_{Si} \quad (6.5)$$

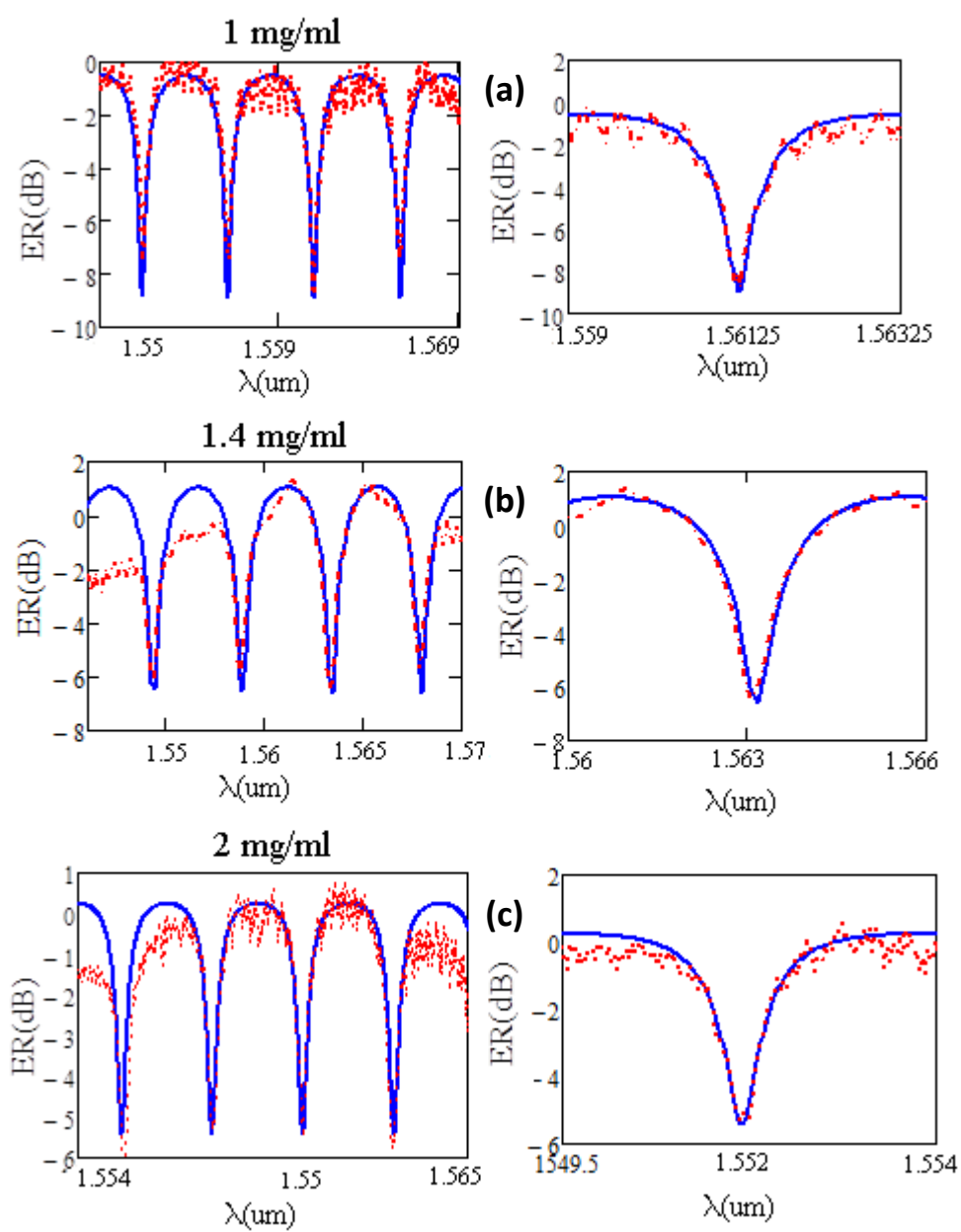
The theoretical transfer function can be fitted to the measured wavelength dependent transmission data for bare cavity resonators (with no graphene oxide) as shown in Fig 6.3, with  $n_{\text{eff}} = 3.40 \pm 0.0005$  as derived from the resonance positions. The value obtained from the fit for r matches the designed value of the cavity. A significant attenuation of 15.9dB at 1.558  $\mu\text{m}$  is observed. Also the fit yields values of  $\tau = 0.998$ , and t= giving the Q factor  $6.823 \times 10^5$ , and propagation loss of 0.011 dB/ $\mu\text{m}$ .





**Figure 6.3 Measured (red) transmission spectrum for a silicon cavity ring resonator (physical dimensions,  $r = 25\mu\text{m}$  and  $g = 0.2\mu\text{m}$ ) without graphene oxide. While blue curve is numerical fit to the data using Eq. (6.2). With  $r = 25\mu\text{m}$ ,  $\alpha = 0.011\text{dBum}^{-1}$  and  $n_{\text{eff}}=3.40351$ . Inset: the measured resonance peaks from  $1.546\mu\text{m}$  to  $1.567\mu\text{m}$**

For precise determination of the attenuation coefficient of graphene oxide integrated devices, five cavity resonators have coated with varying concentration of the graphene oxide. The concentration is varied between 1mg/ml to 4 mg/ml. For each device the resonance spectrum is recorded at the throughput port and the ER calculated. An exemplary set of recorded transmission spectra with different graphene oxide concentrations are shown in Fig 6.4(a–e), along with the theoretically predicated response in Eq.(2.10), which are in good agreement. The result of the fitting of all parameters to the spectra of the through port is listed in table 6.1.



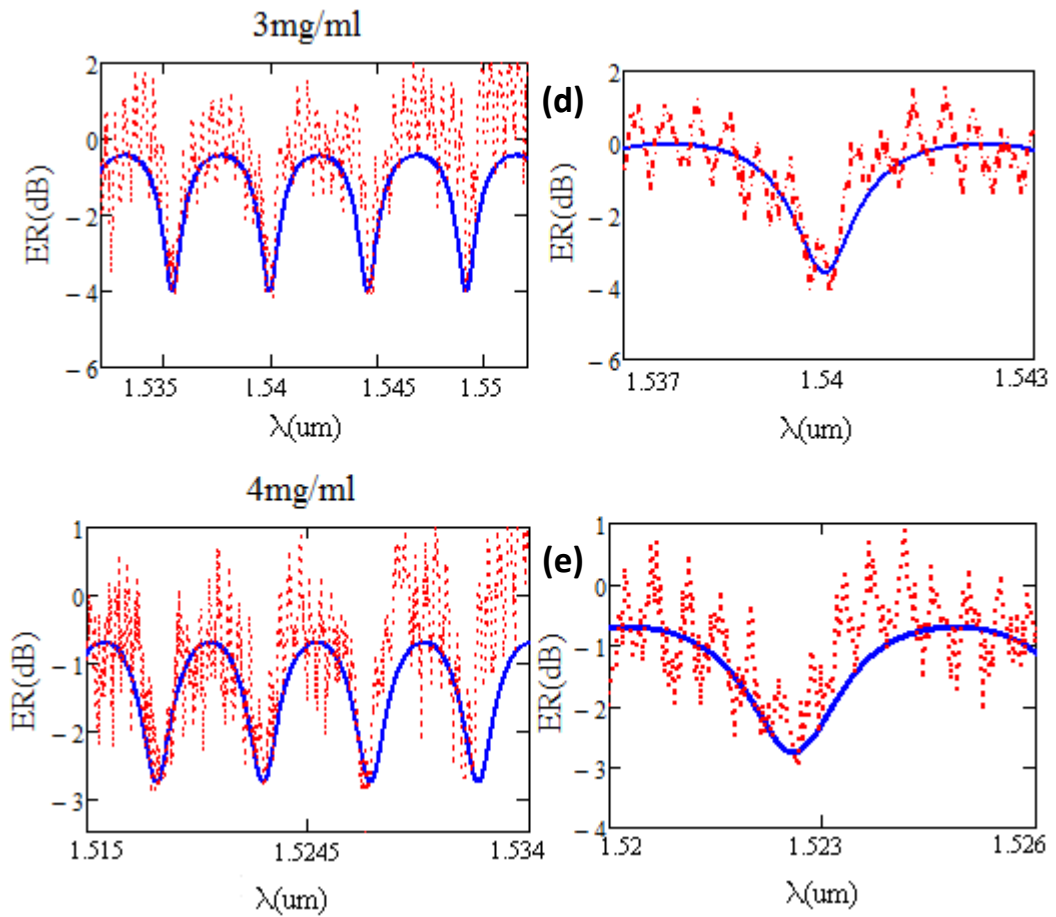


Figure 6.4 (a-e) measured (red) and fitted (eq. (2.10), blue) transmission spectra (left side) (offset for clarity (right side)). Fits to all data sets yield  $n_{\text{eff}} = 3.2973 \pm 0.001$

C(mg/ml)	t	$\tau$	$n_{\text{eff}}$	ER	Q factor	$\alpha_{(\text{GO\_resonator})}$
(1.0)	0.672	0.77	3.3	9dB	$7.67 \times 10^3$	0.02 dB/um
(1.4)	0.677	0.551	3.3004	7.6dB	$5.0 \times 10^3$	0.023 dB/um
(2.0)	0.717	0.54	3.302	5.9dB	$3.19 \times 10^3$	0.038dB/um
(3.0)	0.82	0.46	3.3045	2.9dB	$1.88 \times 10^3$	0.056dB/um
(4.0)	0.80	0.332	3.307	1.8dB	$1.06 \times 10^3$	0.09 dB/um

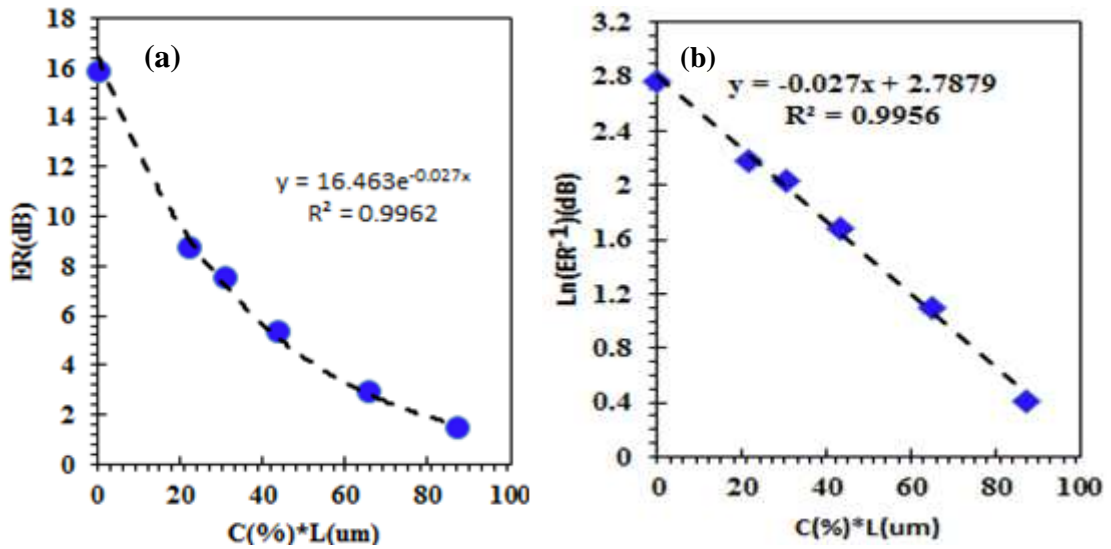
Table6.1 shows parameters for linear absorption coefficient deduction after GO coating with different concentrations.

Fig6.4 shows that the extinction ratio (ER) decreases with increasing the GO concentration. With no graphene oxide An ER (0) of 16dB is obtained, which decreases

from 9dB for a 1mg/ml GO concentration to below 2dB for 4mg/ml Go concentration respectively. Also, the Q factor as calculated from eq. 6.1 decreases with increasing GO concentration. In the case of the GO integrated MRRs we have measured, the losses leading to the significant reduction of the extinction ratio, and the Q factor and the resonances broadening observed in fig 6.4 are almost entirely the result of increased propagation loss in the GO layer over the cavity surfaces.

The extinction ratio values (ER) of each device is plotted as a function of the curvature length coated with different percentage GO concentration , along with the measured extinction ratio point for no-graphene ring (ER (0)~15.9dB) as shown in Fig. 6.5. The attenuation can be obtained from linear fit shown in Fig. 6.5(b) of following equation:

$ER = ER(0) - \alpha \cdot L$ . The absorption coefficient value is extracted from a linear fit to the measured data points agrees with the curve for  $\alpha_{GOTE} = 0.027 \pm 0.02 \text{ dB}\mu\text{m}^{-1}$ .



**Figure 6.5** Shows the relationship of the measured peak extinction of cavity resonators and the curvature length coated with different GO concentration of these cavities.

The dependence of the absorption coefficient on the concentration of the graphene oxide in in mg/ml unit is shown in Fig. 6.6. From the relationship between the attenuation and the solution concentration (C) given by Lambert Beer Law  $A = \alpha \cdot C \cdot l$ , (where A is the absorbance,  $\alpha$  is absorption coefficient, C is the GO solution concentration, and L is the curvature length coated with GO (L= 87 um) the absorption

coefficient is related to the absorbance per length  $A/L$ . Here, the fitted value that extracted from a linear fit in Fig 6.6(a) is divided by the GO length (87 $\mu\text{m}$ ) and obtained  $\alpha$  to be 6590  $\text{L.g}^{-1}.\text{m}^{-1}$  which agrees well with values in [19, 36] for nearly the same concentrations.

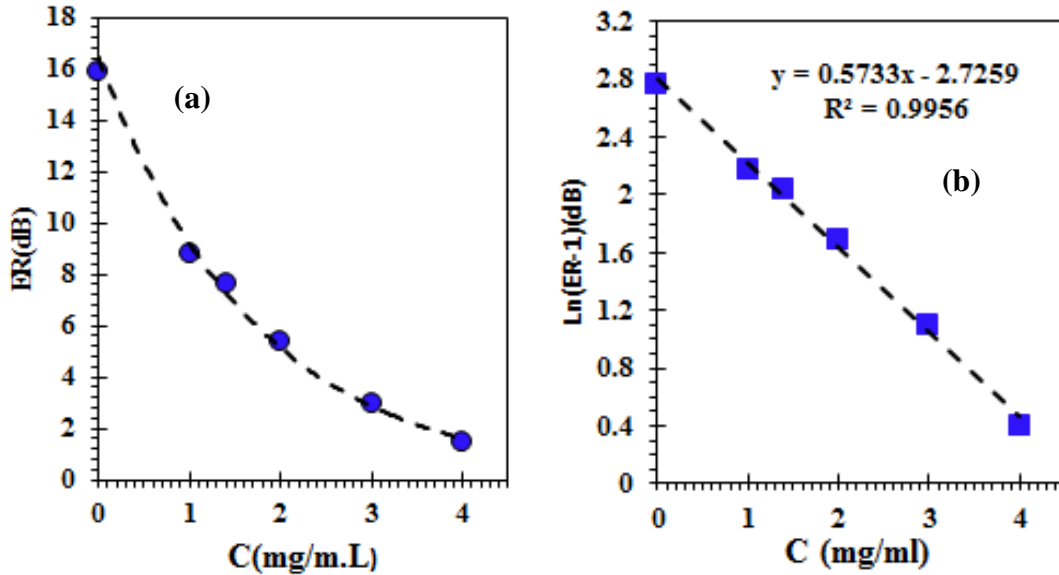


Figure 6.6 Shows the linear relationship between the measured peak extinction and the concentration of GO form  $ER(C)_{\text{dB}} = e^{-\alpha \cdot (C \cdot L)}$  with slope  $\alpha = 6590 \text{ L.g}^{-1}.\text{m}^{-1}$

The performed study have revealed the GO layer on a silicon waveguide has a strong influence on the overall ring performances, i.e., high GO concentrations with a stronger reduction of Q factor and ER. However, lower in-plane optical attenuation coefficient compared with CVD graphene layer on waveguide-based silicon ring resonators, where an attenuation coefficient for CVD graphene between 0.05dB/ $\mu\text{m}$  to 0.23dB/ $\mu\text{m}$  has been reported [13-15,37,38].

## 6.6. Conclusion

In summary, GO integrated with waveguide based MRR have been demonstrated to study the effects of the absorption efficiency of GO coated silicon MRRs. Although the absorption efficiency of GO has been reported with different values in the solution form [18, 19], this the first time that in plane absorption efficiency of GO coated MRRs have been experimentally investigated at near-IR optical wavelength (1550nm). Experimental results indicate that GO on MRRs can retain its high quality factor and line width by careful control of the GO concentrations. Measuring resonances transmission spectra of uncoated and different GO concentrations coated MRRs in TE mode, have been used to determine the attenuation coefficient of a slot waveguide-graphene oxide hybrid structure as  $\alpha_{\text{GOTE}} = 0.027 \pm 0.02 \text{ dBum}^{-1}$ . This is the first time in literature that this has been reported. This work can be used as foundation by other researchers in photonics and optoelectronics in designing GO integrated silicon waveguide based MRRs according to the required applications such as broadband photo-detectors, modulators, polarizers and bio/gas sensors. For example for GO based photo-detectors, want complete absorption so need thick GO film over the cavity resonator, whereas for bio/gas optical sensor applications need thin GO film for partial absorption (i.e. avoid quenching of resonances).

## 6.7. References

1. Dikin, D.A., et al., Preparation and characterization of graphene oxide paper. *Nature*, 2007. **448**(7152): p. 457-460.
2. Stankovich, S., et al., Synthesis of graphene-based nanosheets via chemical reduction of exfoliated graphite oxide. *carbon*, 2007. **45**(7): p. 1558-1565.
3. Dreyer, D.R., et al., The chemistry of graphene oxide. *Chemical Society Reviews*, 2010. **39**(1): p. 228-240.
4. Bolotin, K.I., et al., Ultrahigh electron mobility in suspended graphene. *Solid State Communications*, 2008. **146**(9): p. 351-355.
5. Novoselov, K. and A. Geim, Graphene detects single molecule of toxic gas, 2007, MANEY PUBLISHING STE 1C, JOSEPHS WELL, HANOVER WALK, LEEDS LS3 1AB, W YORKS, ENGLAND.
6. Kochmann, S., T. Hirsch, and O.S. Wolfbeis, Graphenes in chemical sensors and biosensors. *TrAC Trends in Analytical Chemistry*, 2012. **39**: p. 87-113.
7. Lim, W., et al., Graphene oxide-based waveguide polariser: From thin film to quasi-bulk. *Optics express*, 2014. **22**(9): p. 11090-11098.
8. Li, J., et al., The Preparation of Graphene Oxide and Its Derivatives and Their Application in Bio-Tribological Systems. *Lubricants*, 2014. **2**(3): p. 137-161.
9. Wu, C., et al., A novel fluorescent biosensor for sequence-specific recognition of double-stranded DNA with the platform of graphene oxide. *Analyst*, 2011. **136**(10): p. 2106-2110.
10. Gan, X., et al., Chip-integrated ultrafast graphene photodetector with high responsivity. *Nature Photonics*, 2013. **7**(11): p. 883-887.
11. Koester, S.J. and M. Li, High-speed waveguide-coupled graphene-on-graphene optical modulators. *Applied Physics Letters*, 2012. **100**(17): p. 171107.
12. Pospischil, A., et al., CMOS-compatible graphene photodetector covering all optical communication bands. *Nature Photonics*, 2013. **7**(11): p. 892-896.
13. Li, H., et al., Optical absorption in graphene integrated on silicon waveguides. *Applied Physics Letters*, 2012. **101**(11): p. 111110.
14. Crowe, I.F., et al., Determination of the quasi-TE mode (in-plane) graphene linear absorption coefficient via integration with silicon-on-insulator racetrack cavity resonators. *Optics express*, 2014. **22**(15): p. 18625-18632.
15. Cai, H., et al., Enhanced linear absorption coefficient of in-plane monolayer graphene on a silicon microring resonator. *Optics express*, 2016. **24**(21): p. 24105-24116.
16. Kou, R., et al., Influence of graphene on quality factor variation in a silicon ring resonator. *Applied Physics Letters*, 2014. **104**(9): p. 091122.
17. Paredes, J., et al., Graphene oxide dispersions in organic solvents. *Langmuir*, 2008. **24**(19): p. 10560-10564.
18. Khan, U., et al., High-Concentration Solvent Exfoliation of Graphene. *Small*, 2010. **6**(7): p. 864-871.
19. Lotya, M., et al., High-concentration, surfactant-stabilized graphene dispersions. *ACS nano*, 2010. **4**(6): p. 3155-3162.
20. Hernandez, Y., et al., High-yield production of graphene by liquid-phase exfoliation of graphite. *Nature nanotechnology*, 2008. **3**(9): p. 563-568.
21. Robinson, J.T., et al., Ultrasmall reduced graphene oxide with high near-infrared absorbance for photothermal therapy. *Journal of the American Chemical Society*, 2011. **133**(17): p. 6825-6831.

22. Chong, W., et al., Photo-induced reduction of graphene oxide coating on optical waveguide and consequent optical intermodulation. *Scientific reports*, 2016. **6**.
23. Sokolov, D.A., K.R. Shepperd, and T.M. Orlando, Formation of graphene features from direct laser-induced reduction of graphite oxide. *The Journal of Physical Chemistry Letters*, 2010. **1**(18): p. 2633-2636.
24. Ferreira, E.M., et al., Evolution of the Raman spectra from single-, few-, and many-layer graphene with increasing disorder. *Physical Review B*, 2010. **82**(12): p. 125429.
25. Ferrari, A.C., et al., Raman spectrum of graphene and graphene layers. *Physical review letters*, 2006. **97**(18): p. 187401.
26. Krishnamoorthy, K., et al., Investigation of Raman and photoluminescence studies of reduced graphene oxide sheets. *Applied Physics A*, 2012. **106**(3): p. 501-506.
27. Reich, S. and C. Thomsen, Raman spectroscopy of graphite. *Philosophical Transactions of the Royal Society of London A: Mathematical, Physical and Engineering Sciences*, 2004. **362**(1824): p. 2271-2288.
28. Feng, H., X. Wang, and D. Wu, Fabrication of spirocyclic phosphazene epoxy-based nanocomposites with graphene via exfoliation of graphite platelets and thermal curing for enhancement of mechanical and conductive properties. *Industrial & Engineering Chemistry Research*, 2013. **52**(30): p. 10160-10171.
29. Perumbilavil, S., et al., White light Z-scan measurements of ultrafast optical nonlinearity in reduced graphene oxide nanosheets in the 400–700 nm region. *Applied Physics Letters*, 2015. **107**(5): p. 051104.
30. Bogaerts, W., et al., Silicon microring resonators. *Laser & Photonics Reviews*, 2012. **6**(1): p. 47-73.
31. Rabus, D.G., Ring resonators: Theory and modeling. *Integrated Ring Resonators: The Compendium*, 2007: p. 3-40.
32. Rabus, D.G., *Integrated ring resonators*. 2007: Springer.
33. Heebner, J.E., et al., Optical transmission characteristics of fiber ring resonators. *IEEE journal of quantum electronics*, 2004. **40**(6): p. 726-730.
34. Niehusmann, J., et al., Ultrahigh-quality-factor silicon-on-insulator microring resonator. *Optics letters*, 2004. **29**(24): p. 2861-2863.
35. Yang, H., et al., Rapid and non-destructive identification of graphene oxide thickness using white light contrast spectroscopy. *carbon*, 2013. **52**: p. 528-534.
36. Khan, U., et al., Solvent-exfoliated graphene at extremely high concentration. *Langmuir*, 2011. **27**(15): p. 9077-9082.
37. Liu, M., et al., A graphene-based broadband optical modulator. *Nature*, 2011. **474**(7349): p. 64-67.
38. Lee, Y., et al., Wafer-scale synthesis and transfer of graphene films. *arXiv preprint arXiv:0910.4783*, 2009.





## **Chapter 7: Optical based chemical vapour sensing with graphene oxide coated silicon micro-ring resonators**

### **7.1. Introduction**

Graphene oxide (GO) can serve as an ideal material in bio-chemical and gas sensing applications owing to the combination of high specific surface area and hydrophilic oxygen groups, meaning it has high molecular adsorption capacity and strong binding affinity, whilst being water soluble [1,2]. Compared with the transfer process of graphene, GO is also a facile substrate coating as it can be spun on to e.g. silicon or glass in solution form and subsequently dried. GO also exhibits superior performance to graphene, in terms of sensitivity and response time to gas molecular adsorption because of the combined reactivity and porous nature of the material [3,4]. All of these attributes make GO an interesting functional coating material for chemical gas/vapour sensing.

In this work, we propose and demonstrate GO integrated waveguide based silicon micro-ring resonator (MRR) devices for optical based chemical vapour sensing. Measurement of the shift in the MRR cavity resonance wavelength is determined as a result of changes in the concentration of the adsorbed vapour molecules, as a result of changes in the near surface refractive index.

Although GO coating has previously been used for electrical based vapour sensing [1], and combined with optical fibre for optical based sensing [5,6] to our knowledge, this is the first implementation of a photonic chip-based GO integrated MRR as an optical sensor for the detection of gas/vapours. Comparing the sensitivity and response of a bare MRR device exposed to a range of vapours with that of the GO integrated device, we determine both an improved sensitivity and response rate.

### **7.2 Experimental details**

#### **7.2.1 Optical device and GO synthesis**

The MRR devices comprise of an asymmetric slot waveguide based ring (with c. 50nm slot) coupled to a single strip-type bus waveguide. The bus-to-outer ring coupling gap,  $g = 0.25\mu\text{m}$  and the ring (centre-to-slot) radius,  $r = 25\mu\text{m}$ . The sample cleaning and GO

synthesis followed the procedure detailed in the previous chapter (sections 6.2.2 and 6.2.3). Here a 1.5 mg/mL concentration of GO was prepared and sonicated in an ultrasonic bath for 30 min and this was spun-coated over the entire cavity.

### 7.2.2 Sensing characterisation

The response of the uncoated and GO coated MRRs to variable vapour concentrations was determined using the optically integrated gas cell described in chapter 3, and all measurements were conducted at room temperature.

Light from a broadband semiconductor laser diode was coupled into/out of the bus waveguide through grating couplers using purpose built optical delivery/collection and the light detected and measured at set time intervals using an optical spectrum analyser. The gas cell was purged with dry N<sub>2</sub> for a 30 min period in order to suppress contaminant effects of water and oxygen to the target vapour sensing experiments. The target compounds (ethanol, pentene and acetone) were individually evaporated in a purpose built 'bubbler' arrangement by mixing a small volume of the liquid solvents with the dry N<sub>2</sub>. The relative vapour concentration in the mix was controlled by careful adjustment of an integrated flow meter. The vapour concentration was estimated from calculations based on the vapour pressure at 25°C and the diluting/carrier gas (N<sub>2</sub>) flow rate. The output flow rate of vapour,  $F_{\text{solvent}}$  can be described with the bubbler equation [7, 8]:

$$F_{\text{solvent}} = \left( \frac{P_{\text{solvent}}}{P_0 - P_{\text{solvent}}} \right) F_C \quad (7.1)$$

Where,  $P_0$  is the outlet pressure in the bubbler headspace and  $P_{\text{solvent}}$  is the equilibrium vapour pressure of the solvent, which is calculated from the empirical Antoine equation [7]:

$$P_{\text{Solvent}} = 10e^{(A - \frac{B}{C+T})} \quad (7.2)$$

Where  $T$  is the temperature and  $A$ ,  $B$ ,  $C$  are specific empirical constants of the compound. The vapour concentration at the bubbler output is diluted with the N<sub>2</sub> to achieve a required level of vapour concentration. The resultant vapour concentration in parts per million,  $C_{\text{vapour}}(\text{ppm})$  in the detection cell is then calculated from  $F_{\text{solvent}}$  and the dilution ratio by [9] :

$$C_{Vapour}(ppm) = \frac{10^6 \times F_{solvent}}{F_D + F_C + F_{solvent}} \quad (7.3)$$

Where,  $F_c$  is the  $N_2$  carrier flow rate, and  $F_D$  is the dilution flow rate.

We compare the measurement of solvent vapour for bare and GO coated MRRs. The measurements focus on both the absolute shift in resonant wavelength of the MRR and the shift rate for different relative concentrations of the three target vapours we have considered.

### 7.3. Results and discussion

The sensitivity ( $\Delta\lambda/\Delta C_{vapour}$ ) and the limit of detection (LOD) of MRR based sensors generally depends on the ability to resolve spectral shifts and so is improved for narrower resonances i.e. MRRs with a higher Q-factor (where the Q-factor is defined in the usual way by  $\lambda/\Delta\lambda$ ). Comparison of the transmission spectra for the MRR device used in this study, before and after GO coating is shown in Fig 7.1. We observe a reduction of the Q-factor from  $6.7 \times 10^5$  to  $3 \times 10^3$  (broadening of the resonant mode) and a drop in the extinction after GO coating, both of which are a direct consequence of increased cavity losses (due to both scattering at the Si/GO dielectric interface and absorption within the GO layer). The resonant wavelengths are also shifted as a result of the modification of the mode effective refractive index,  $n_{eff}$  induced after GO coating as shown in chapter 6.

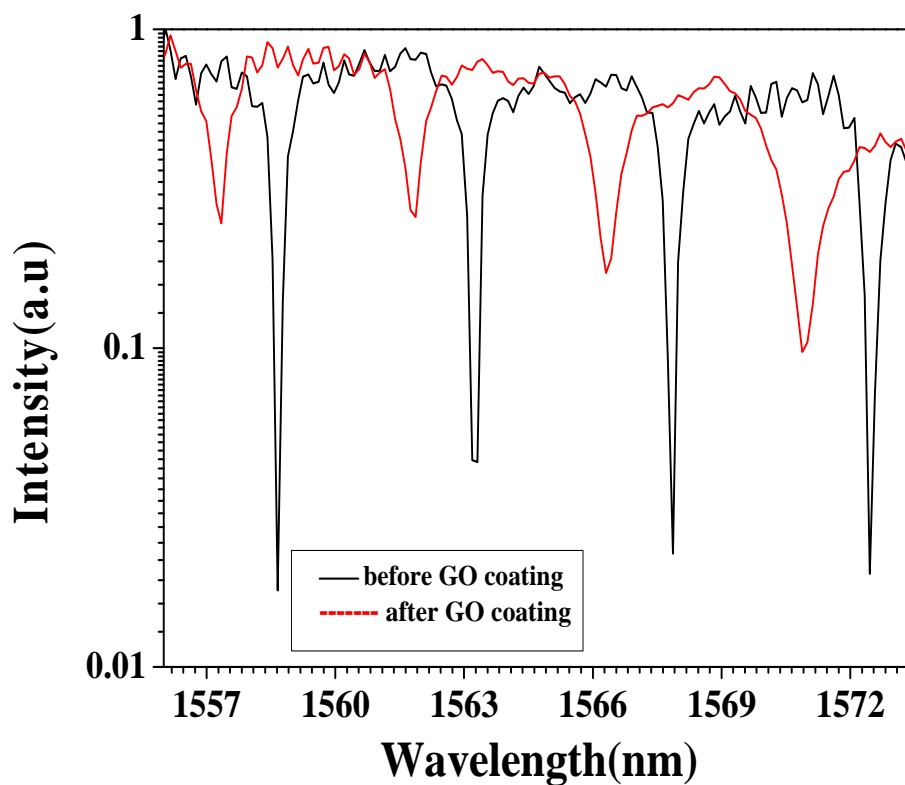


**Figure 7.1 Comparison of the optical transmission spectra of the MRR before (black) and after (red) coating with GO**

We first studied the change in the resonance wavelength for both the bare and GO coated MRR when exposed to ethanol vapour at various concentrations in the range 100 to 1000ppm, Fig 7.2. The spectra are compared with that obtained after purging with dry  $N_2$ .

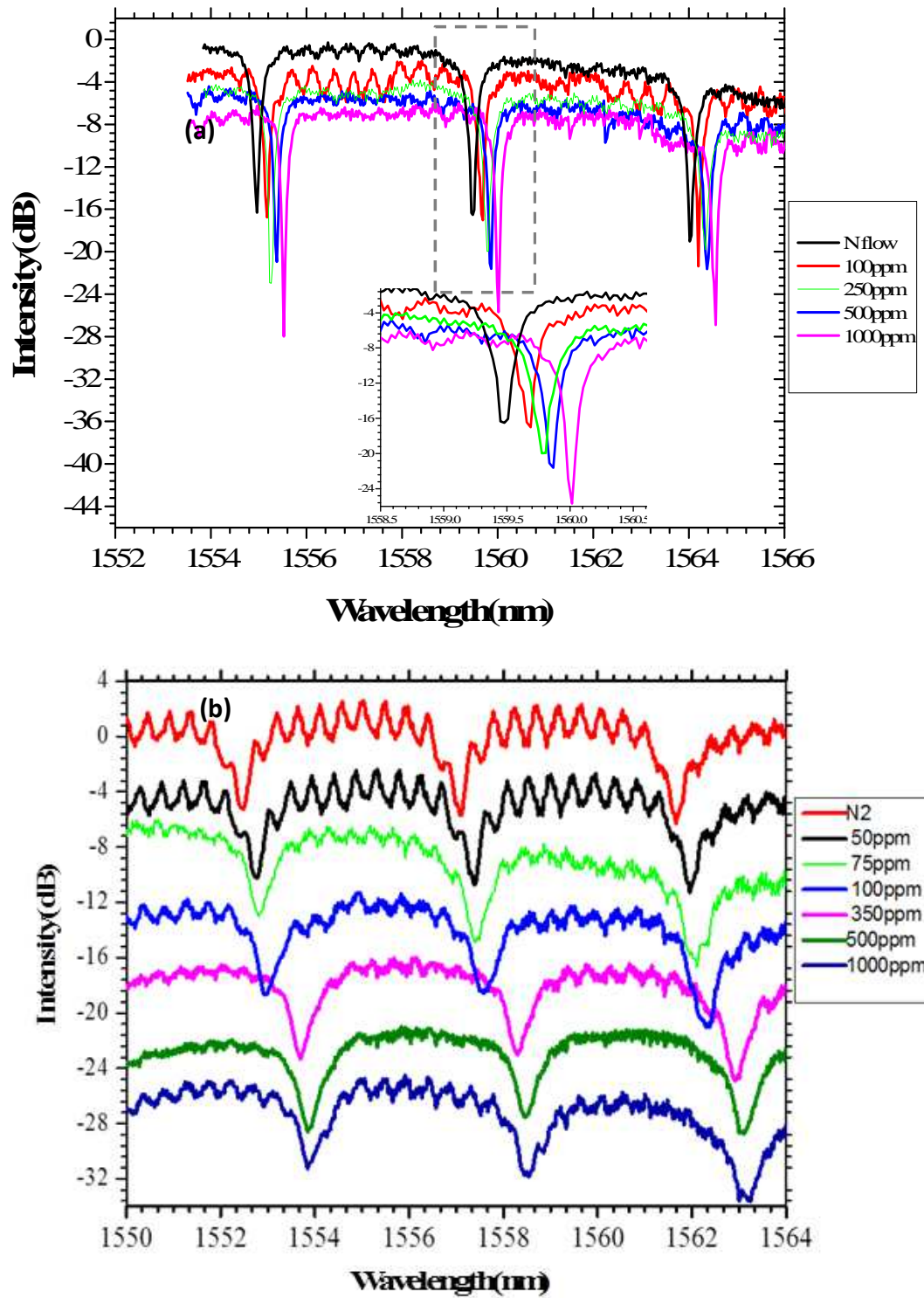


**Figure 7.2 Measured transmission spectra for (a) uncoated and (b) GO coated MRR as a function of ethanol vapour concentration (indicated).**

In general, exposure to ethanol vapour leads to resonance shifts towards longer wavelength, the degree of which increases with vapour concentration. For the bare MRR, the absolute change in resonant wavelength during exposure to ethanol was

small and we noted that the shift was completely reversible (i.e. full return to baseline  $N_2$  value) when the ethanol flow was stopped.

For the GO coated MRR exposed to ethanol in the same range of concentrations, we noted that the resonant wavelength shift was in the same direction but that the degree of shift was approximately 3 times greater (than for the bare MRR) for the same vapour concentration. We also noted, from the dynamic measurements, that the up shift-rate (during ethanol flow) was higher but the down shift-rate (after stopping the ethanol flow) was slower with GO. We also noted that the shift for the GO coated MRR was not fully reversible. These observations imply that the uptake (adsorption) of ethanol is more efficient with GO coated MRRs and that the ethanol molecules become ‘trapped’ (likely within the pores of the GO membrane) meaning that they are released (desorbed) more slowly, with a fraction remaining within the layer. Fig 7.3 (a, b) shows the resonant wavelength shift with ethanol concentration for the bare and GO coated MRRs, respectively.

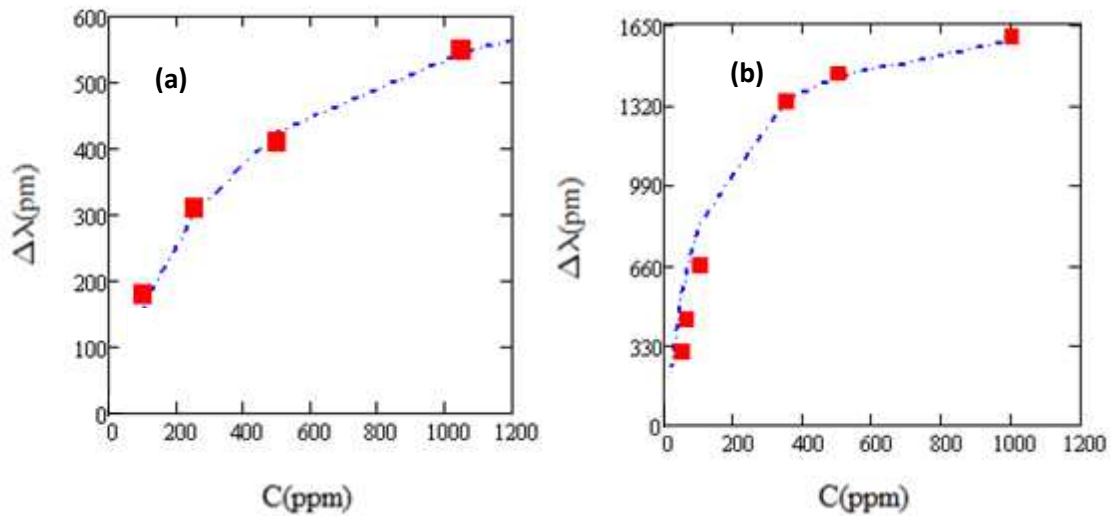


**Figure 7.3** Cavity resonance wavelength shift with ethanol concentration for (a) bare MRR and (b) GO coated MRR. Red squares are measured data of the resonance shift at different ethanol concentrations relative to the resonance shift for pure  $N_2$ , and the blue dashed lines are Langmuir adsorption isotherm fits, eq.7.4.

The data is well described by the Langmuir adsorption isotherm model: [10,11]:

$$\Delta\lambda = \lambda_{max} \frac{C_0 K_A}{1 + C_0 K_A} \quad (7.4)$$

Where  $\Delta\lambda$  is the measured wavelength shift, assumed to be proportional to the volume of adsorbed ethanol, and writing the partial pressure of ethanol as  $C_0/10^6$  bar with  $C_0$  the concentration of ethanol vapour.  $\lambda_{\max}$  is the maximum wavelength shift, i.e. where the bare and GO coated surfaces are saturated with ethanol  $K_A$  is the unitless equilibrium constant. In order to gain insight into the adsorption mechanism, we use the Langmuir fit to determine the Gibbs free energy ( $\Delta G$ ), which reveals the degree of spontaneity of adsorption, or binding affinity from [10]:

$$\Delta G = -RT \ln K_A \quad (7.5)$$

In which  $K_A$  is the equilibrium constant determined from the Langmuir fit,  $T$  is the temperature in Kelvin (K), and  $R$  is the universal gas constant of  $8.314 \text{ J.mol}^{-1} \text{ K}^{-1}$ . The equilibrium constant obtained from the fit in Fig. 7.3 (a) (bare cavity) is,  $K_A = 2.8 \times 10^3$ , yielding a free energy of adsorption of  $-20 \text{ kJ/mol}$ , with a maximum wavelength shift  $\lambda_{\max}$  of  $680 \text{ pm}$ . From the Langmuir fit in Fig. 7.3 (b), (GO coated cavity) we obtain a maximum wavelength shift  $\lambda_{\max}$  of  $1770 \text{ pm}$ , and equilibrium constant,  $K_A = 10 \times 10^3$ , corresponding to a free energy of adsorption of  $-23 \text{ kJ/mol}$ . The larger negative value obtained for the GO coated cavity reflects a more energetically favourable adsorption. This is likely to be the combined result of the porous nature of the GO coating with the high surface area indicating a generally improved sensing performance compared with bare MRR devices.

In the low concentration limit, the Langmuir isotherm in Fig. 7.3 is nearly linear and we use this to estimate the limit of detection (LOD) for the MRR based sensor. The results of these measurements are presented in Fig. 7.4 (a, b).



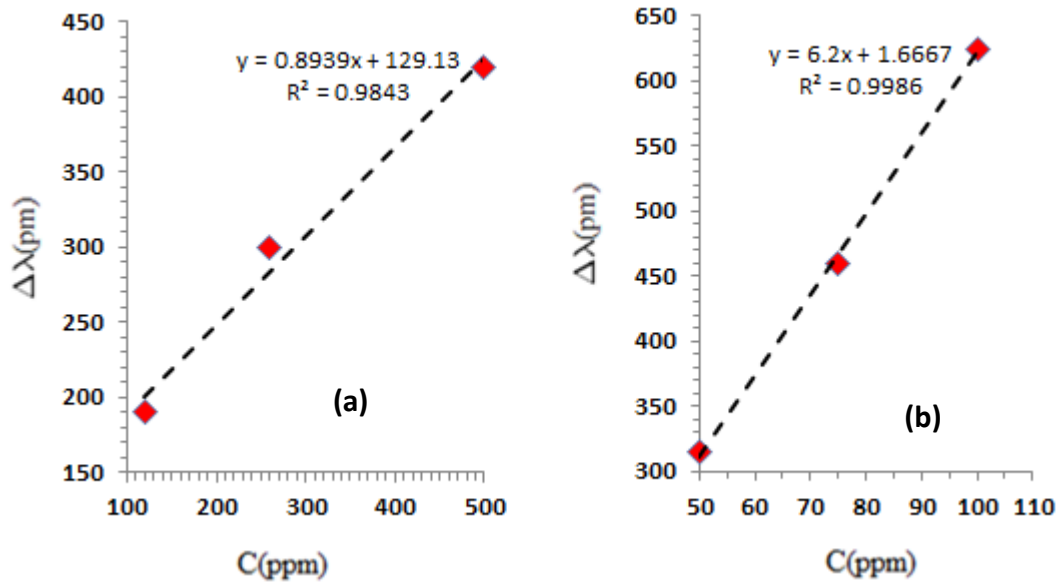


**Figure 7.4 Resonant wavelength shift with ethanol vapour concentration in the low concentration limit relative to the resonance shift of pure N<sub>2</sub> for (a) bare and (b) GO coated MRR.**

The sensitivity in the case of the bare MRR was determined to be  $S \sim 0.9\text{pm/ppm}$ , whereas for the GO coated MRR, the sensitivity was found to be  $S \sim 6.2\text{pm/ppm}$ .

The sensor LOD can be determined from the ratio of the standard error,  $s$  from the linear regression fit to the data in the low concentration limit, and the sensitivity,  $S$ ;  $\text{LOD} = 3.3 s_{y,b}/S$  [12]. By this method, we estimate a LOD of approximately 4.3ppm for the GO integrated MRR, compared with approximately 66ppm for the bare MRR. The sensitivity and LOD determined here (for both bare and GO coated) are higher than that reported previously for an opto-fluidic ring resonators (OFRR) sensor coated with a vapour-sensitive polymer for ethanol vapour [13]. The LOD value determined here for the bare MRR are comparable with that previously reported for ethanol sensing with a ZnO coated ring resonator [14]. The higher sensitivity (lower LOD) values we have determined for the GO coated MRR, despite the reduced MRR Q-factor after GO integration, suggests it could be both an accurate and facile approach to vapour sensing generally.

The dynamic response of the bare and GO coated MRRs to ethanol vapour of different concentrations is shown in Fig.7.5. The sensor was initially purged with N<sub>2</sub> and then

ethanol mixed at different concentrations, with N<sub>2</sub> purging in between to examine both adsorption and desorption rates.

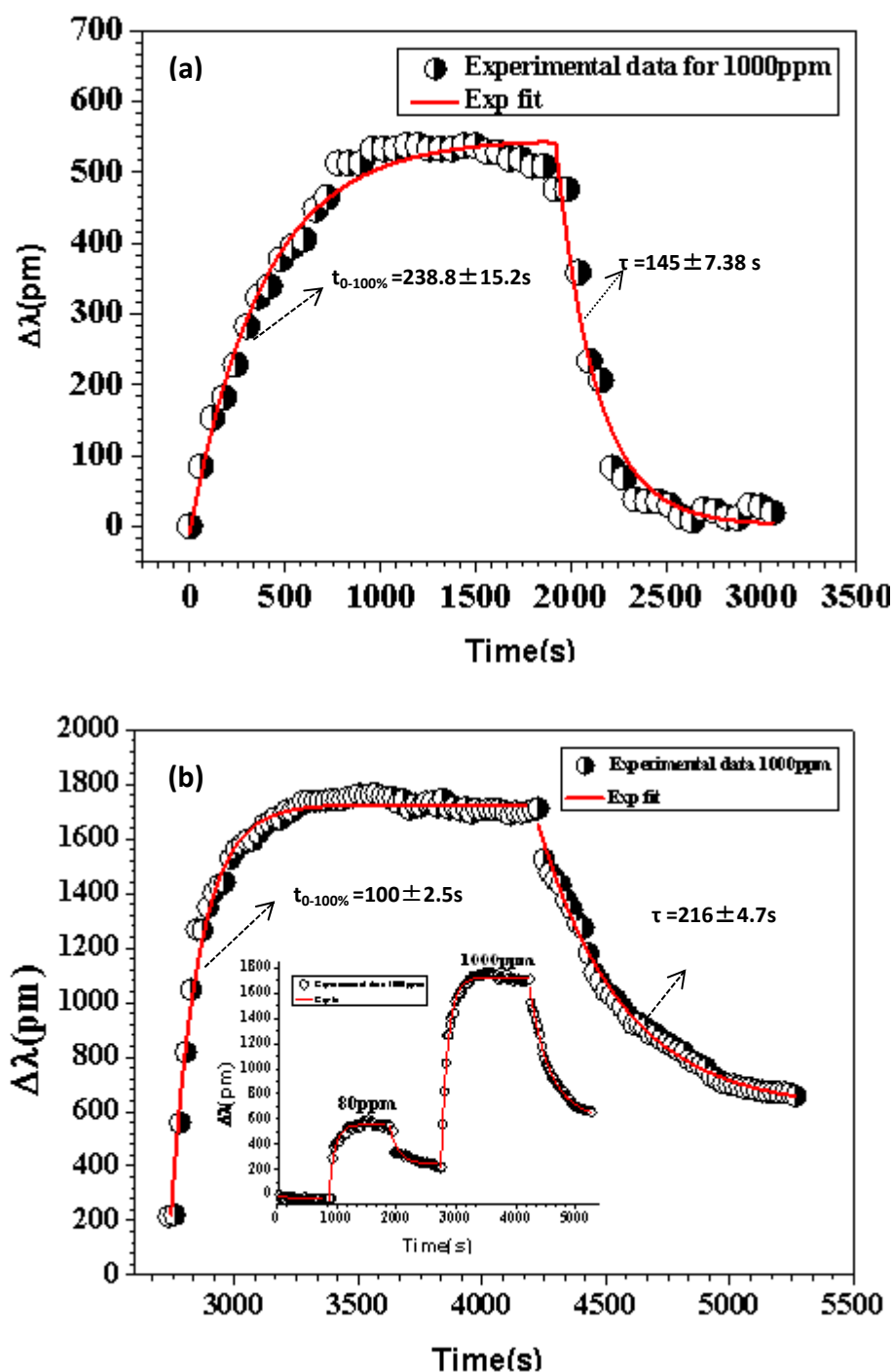


Figure 7.5 Dynamic ethanol vapour sensing characteristics for (a) bare and (b) GO coated MRR cavities. Black points are measured data and red lines are exponential fits.

Fig. 7.5 reveals the very different adsorption/desorption rates for the bare and GO coated MRRs exposed to an equivalent ethanol vapour concentration (1000ppm). The adsorption rates ( $t_{0-90\%}$ ) for the bare and GO coated MRRs were computed to be 215s and 90s, respectively. For pure N<sub>2</sub> purging, desorption rates were determined to be 145s and 216s for the bare and GO coated MRRs, respectively. This indicates that the GO coating lowers (raises) the energy barrier to adsorption (desorption), compared with the bare MRR cavity. We also note the desorbed saturation level is hysteretic, indicating a 'trapping' of a relatively large fraction (possibly as much as 30%) of the adsorbed ethanol. This type of adsorption/desorption behaviour is consistent with the porous nature of the GO coating, indicating a higher density of molecular binding sites (within the porous network) as well as a stronger binding affinity.

In order to investigate whether the MRR based sensing was generally applicable (i.e. to different organic compounds) we examined the response of the bare and GO coated MRRs to freely available compounds; acetone (for comparison of alcohol with ketone) and pentene (for comparison with a phenol). Fig 7.6 (a, b) reveals the measured MRR transmission spectra showing the resonance shifts for bare and GO coated MRRs exposed to pentane in the concentration range 0-1000 ppm.

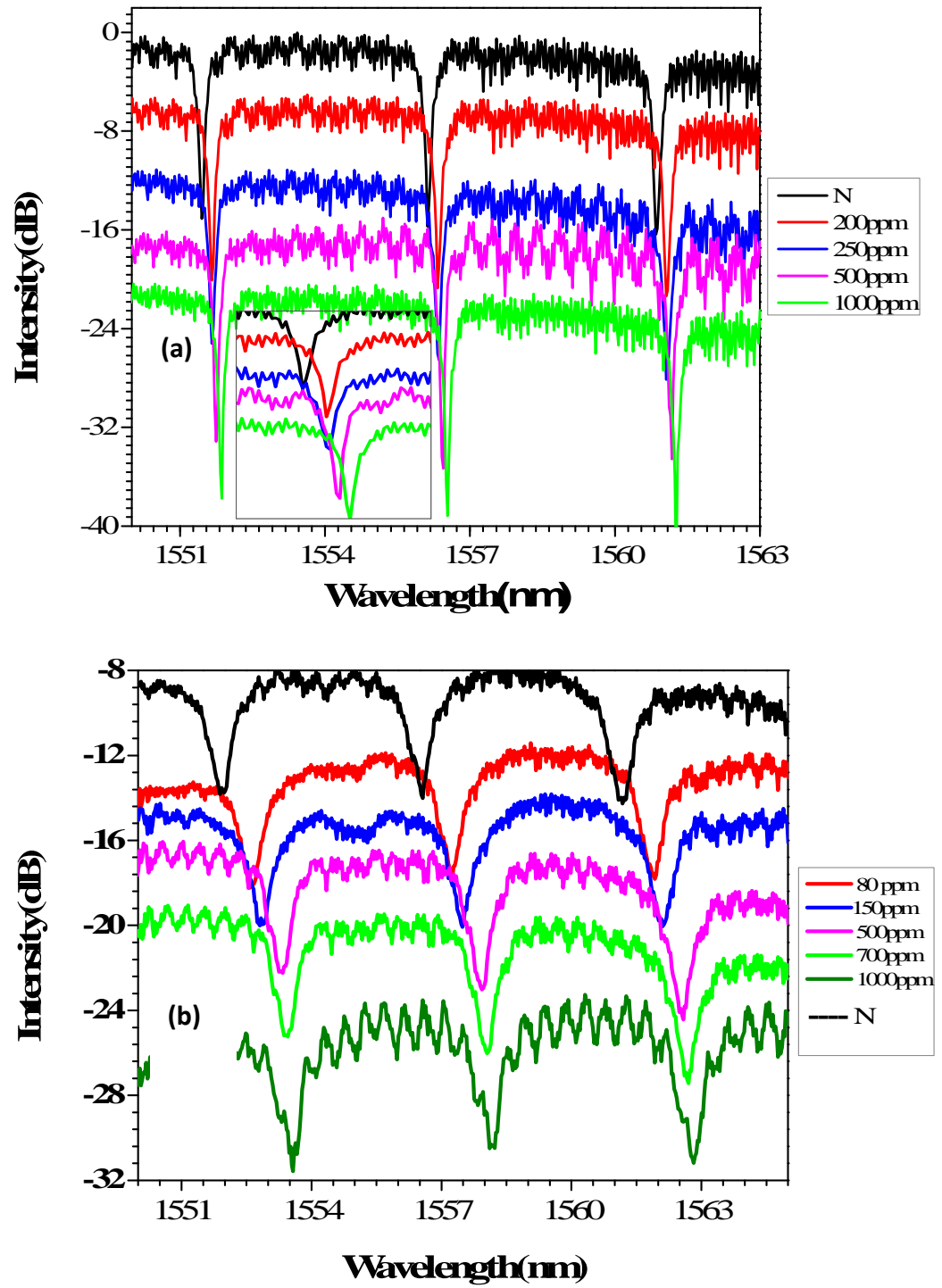
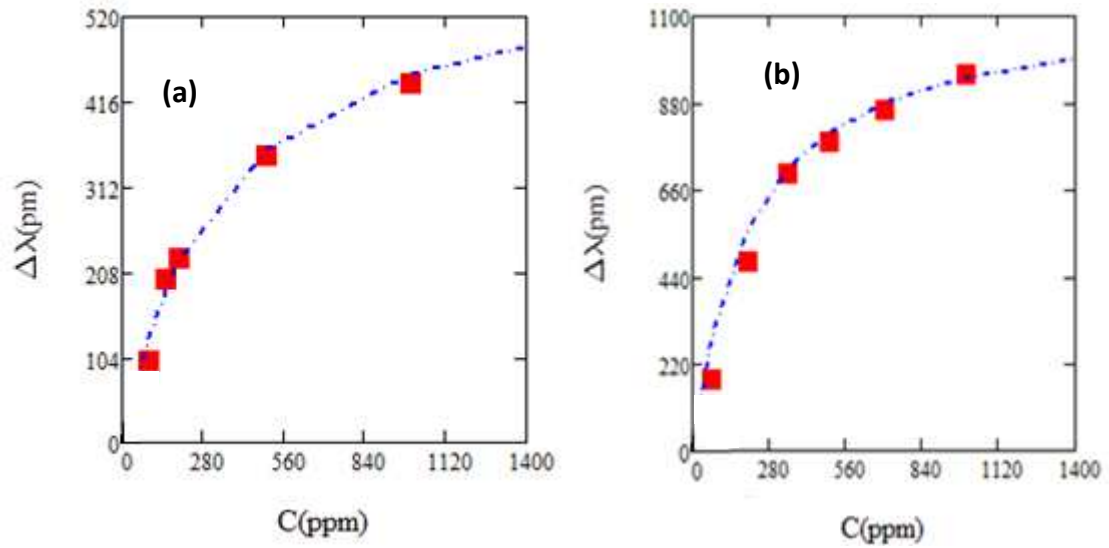


Figure 7.6 Measured transmission spectra of (a) bare and (b) GO coated MRR as a function of pentene vapour concentration

The resonance peak shifts with pentene concentration are shown for the bare and GO coated MRRs in Fig. 7.7 (a, b).



**Figure 7.7** Cavity resonance wavelength shift with pentene concentration for (a) bare MRR and (b) GO coated MRR. Red squares are measured data of the resonance shift for different pentene concentration relative to the resonance shift for pure  $N_2$  (All plotted data is normalised to the point for zero vapour concentration i.e. resonance shift due to vapour is defined relative to 100%  $N_2$ ), and the blue dashed lines are Langmuir adsorption isotherm fits, eq. 7.4.

The data is fitted to the Langmuir adsorption isotherm model and the equilibrium constant and maximum wavelength shift extracted from the fit are  $K_A = 2 \times 10^3$  and  $\lambda_{\max} = 645 \text{ pm}$ , yielding a free energy for the bare MRR,  $\Delta G = -18.5 \text{ kJ/mol}$ . For the GO coated sensor,  $K_A = 6 \times 10^3$  and  $\lambda_{\max} = 1130 \text{ pm}$ , giving  $\Delta G = -21.1 \text{ kJ/mol}$ . Again, these values indicate a lower energy to adsorption for the GO coated MRR but we note that the enhancement provided by the GO is lower than that compared with ethanol.

Fig. 7.8 shows the dynamic response of the bare and GO coated MRRs to pentene vapour in a range of concentrations.

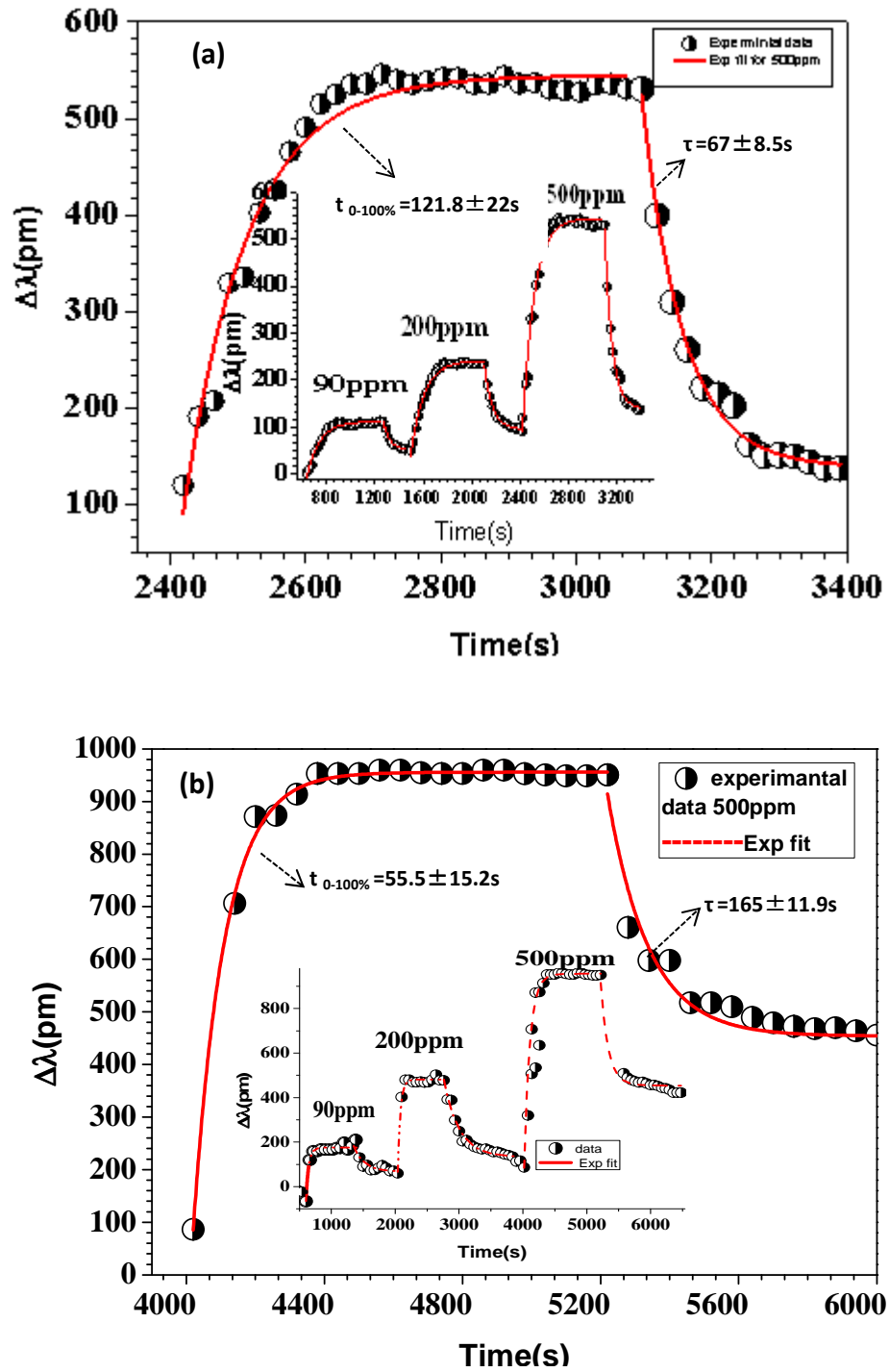


Figure 7.8 Dynamic pentene vapour sensing characteristics for a) bare and (b) GO coated MRR cavities. Black points are measured data and red lines are exponential fits.

The exponential fits to the data in Fig.7.8 reveal 500ppm adsorption rates,  $t_{0-90\%}$  of 109.6s, and 50s and desorption rates of 67s and 165s for the bare and GO coated MRRs, respectively. We note, as with the ethanol sensing, a non-return to zero for the

pentene desorption, although the fraction of retained pentene appears to be higher (than for ethanol), with perhaps as much as 40-50% 'trapped'. Again, the difference in these adsorption/desorption rates (and 'trapping') is generally attributable to a strong binding of pentene within the porous GO network. The fact that the differences (between bare and GO coated MRRs) for pentene differ from that of ethanol might point to a possible route for discriminating between different gases (which is typically challenging when only considering detection based on changes in refractive index).

The transmission spectra showing the sensor response to acetone vapour exposure is shown in figure 7.9 (a,b).

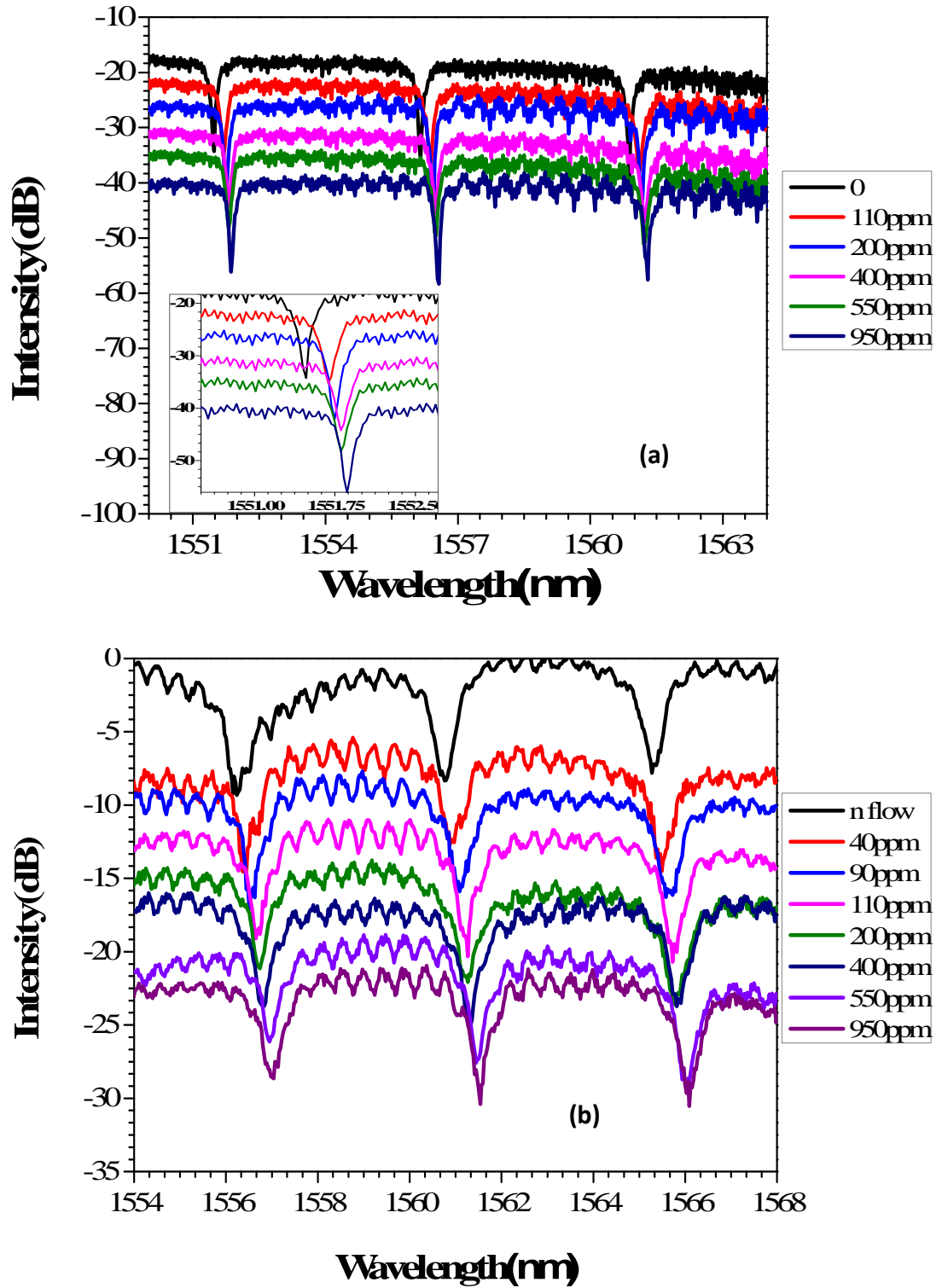
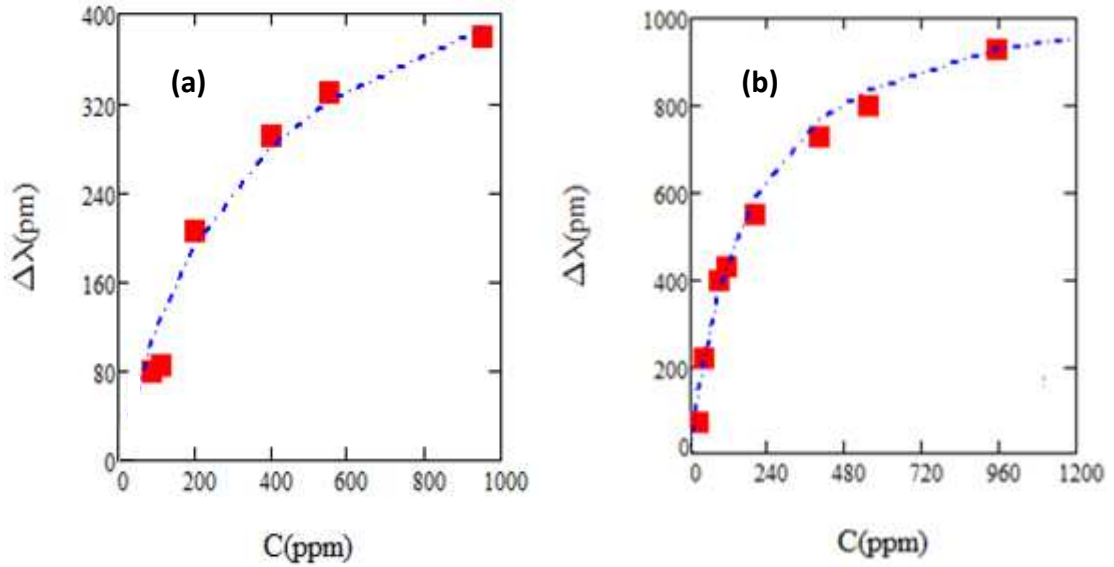


Figure 7.9 Measured transmission spectra of (a) bare and (b) GO coated MRR as a function of acetone vapour concentration

We noted from the transmission spectra that, when attempting to detect acetone vapour with the bare MRR, no response could be determined for concentrations lower than 100ppm and above this, only relatively small shifts in the resonant wavelength



were detected. The sensitivity determined from the linear component of the Langmuir fits in Fig.7.10 (a), for the lowest range of concentrations (up to 200ppm) was approximately  $S \sim 0.8\text{pm/ppm}$ . In contrast, for the GO coated MRR, we were able to reliably detect shifts for concentrations as low as 40 ppm, with a computed sensitivity  $S \sim 3.3\text{pm/ppm}$  in the low concentration limit (up to 110ppm), Fig.7.10 (b). Comparison with literature indicates that this is an improvement over a 20nm PDMS coated slot waveguide for Acetone vapour sensing [15].



**Figure 7.10** Cavity resonance wavelength shift with acetone concentration for (a) bare MRR and (b) GO coated MRR. the Red squares are measured data of the resonance shift at different concentration relative to the resonance shift for pure  $N_2$  (the plotted data is normalised to the point for zero vapour concentration i.e. resonance shift due to vapour is defined relative to 100%  $N_2$ ), and the blue dashed lines are Langmuir adsorption isotherm fits, eq. 7.4.

Fig. 7.11 shows the dynamic response curves for acetone at 110ppm concentration for both bare and GO coated MRR sensors.

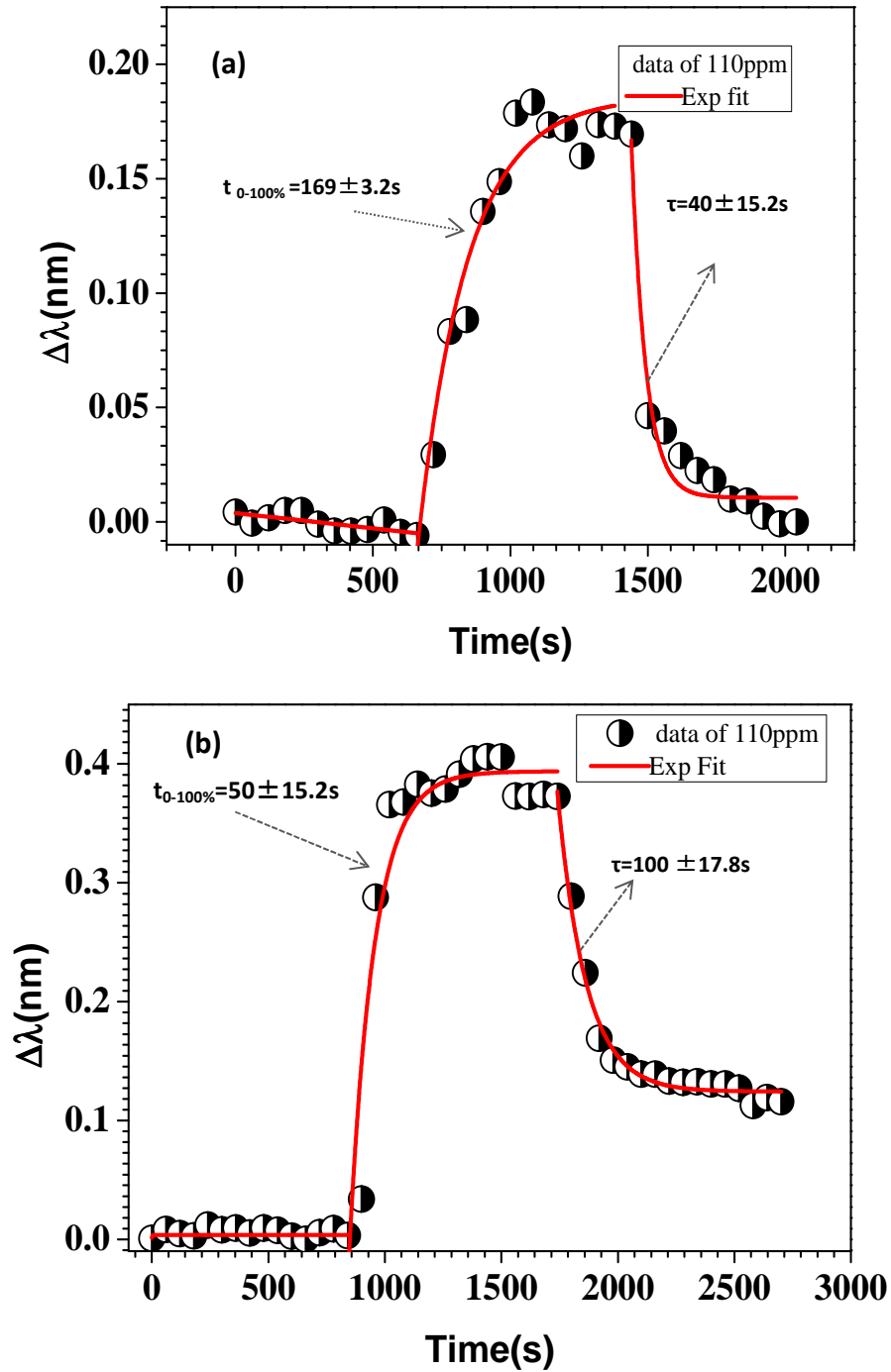


**Figure 7.11** Real-time acetone vapour sensing characteristics of sensors characteristics at 110ppm concentration based on (a) uncoated, and (b) on GO coated cavity resonators, where black dots experimental data, red line exponential fit

We found that the bare sensor response to acetone vapour,  $t_{0-90\%} = 161$  s, whilst for the GO coated sensor, this was approximately 45 s, while desorption recovery is achieved within 40 s and 100 s, respectively. Again, saturation levels were larger for the

GO coated sensor (a little higher than 2 times) and there was evidence of 'trapping' during desorption (pure N<sub>2</sub> purging), at the level of approximately 25 to 30%.

The results indicated that all organic vapours tested here interacted with the GO surface much more strongly than for the uncoated MRRs. However, the different sensitivities due to the different adsorption energy indicating that the GO based sensor has no a degree of selectivity to the different vapours. Furthermore, desorption of vapours on uncoated MRRs, is observed to be fully reversible, whereas for GO sensor is observed to be slow due to the strong adsorption of vapour molecules on GO.

The fact that the different GO adsorption/desorption for different vapours tested could be purely physical; if the porous nature of the GO constricts certain molecules but more easily accepts others, then one would expect a difference in the adsorbed concentration [16,17]. Alternatively, this could be due to different chemical interaction between the GO functional groups and the adsorbed vapours. GO acts as a Lewis acid since the oxygen functional groups can accept pairs of electrons to their incomplete orbitals, while the vapours could be Lewis bases if they include an OH ion or carbonyl group, which can donate a pair of nonbonding electrons. Lewis acid-base interactions should give rise to a much stronger, or higher likelihood of bonding, which would give rise to both a faster and more prominent optical response to the changing surface chemistry (due to the change in near surface refractive index) [18,21,22].

This theory would explain the stronger response to ethanol compared with acetone. The dissociation of a hydrogen (H<sup>+</sup>) atom or OH ion to form a surface hydroxyl, or a surface alcoxide with the former tending to be transformed into an aldehyde or a ketone [18]. Acetone has no H<sup>+</sup> atoms or OH groups and so the reactivity with the GO surface groups can be expected to be weaker [18-20].

## 7.4. Summary

In this chapter, A simple and efficient spin coating of GO onto the waveguide based MRR was demonstrated. This alters the effective refractive index of the guided mode and increases the cavity losses, although not sufficiently to quench the spectrally detected resonances in the optical transmission spectra. The application of bare and GO coated silicon photonic MRR optical cavity devices was studied for chemical vapour sensing. Although a little work for optical vapour sensing using MRRs [13,14,15], and GO combined with optical fibre for optical based sensing [5, 6], have been conducted in literature, this is the first time in literature that the implementation of a photonic chip-based GO integrated MRR for optical gas/vapours detection has been reported. Changes in the near surface refractive index during vapour flowing within the waveguide mode evanescent field result in observed shifts in resonance for both the bare and GO coated MRR. The sensitivities for organic compounds, ethanol and pentene and acetone for both sensors have been experimentally demonstrated. The bare MRR exhibited a relatively low sensitivity but fully reversible response to the three vapours tested. However, the GO coated MRR resonator exhibited a higher sensitivity to vapour sensing despite the higher losses (poorer Q-factor), compared with the (high Q) bare MRR. Comparing the GO coated MRR response to three different organic compounds; we found that the sensitivity was highest for ethanol  $\sim 6.2\text{pm/ppm}$ , followed by acetone  $\sim 3.3\text{pm/ppm}$ , then pentene  $\sim 2.9\text{pm/ppm}$  in the low concentration limit ( $<120\text{ ppm}$ ), with response times in the 45-90s range (depending on compound and exact concentration). Here, the different sensitivities due to the different adsorption energy indicating that the GO based sensor has no a degree of selectivity to the different vapour molecules. In all of the tests, the GO coating provided a faster dynamic response to vapours (and a slower desorption rate) as well as evidence of molecular 'trapping', which we interpret as being indicative of the porous nature of the GO. A deeper understanding of this porous structure and reactivity between GO oxygen functional groups and the different organic compounds, tested here as proof-of-concept, will undoubtedly help to develop this technology. Combining measurement of the cavity resonance change through near surface changes in refractive index with chemical interaction with GO functional groups and physical 'filtering' of specific compounds as a result of their relative size (e.g. by constriction in GO porous networks)

could provide a route to label free detection of mixed compounds (of gases with similar refractive indices) with relatively high sensitivity (compared with bare MRR devices and indeed other functionalised Si based optical and electrical devices already reported). This result demonstrates the potential role of GO functionalized silicon based optical cavity resonators as a potential low cost, real time VOC sensor, e.g. in healthcare, energy and security applications. The work described here can form the basis of optimised device designs by comparing GO coatings with different concentration, functional groups and porosity. For future work, researchers in optical vapour/gas sensors can be used this work to test selectivity for different gas molecules.

## 7.5 References

1. Matesanz, M.-C., et al., *The effects of graphene oxide nanosheets localized on F-actin filaments on cell-cycle alterations*. Biomaterials, 2013. **34**(5): p. 1562-1569.
2. Wu, C., et al., *A novel fluorescent biosensor for sequence-specific recognition of double-stranded DNA with the platform of graphene oxide*. Analyst, 2011. **136**(10): p. 2106-2110.
3. Novoselov, K. and A. Geim, *Graphene detects single molecule of toxic gas*, 2007, MANEY PUBLISHING STE 1C, JOSEPHS WELL, HANOVER WALK, LEEDS LS3 1AB, W YORKS, ENGLAND.
4. Kochmann, S., T. Hirsch, and O.S. Wolfbeis, *Graphenes in chemical sensors and biosensors*. TrAC Trends in Analytical Chemistry, 2012. **39**: p. 87-113.
5. Xiao, Y., et al., *Reduced graphene oxide for fiber-optic toluene gas sensing*. Optics Express, 2016. **24**(25): p. 28290-28302.
6. Yu, C.-B., et al., *Graphene oxide deposited microfiber knot resonator for gas sensing*. Optical Materials Express, 2016. **6**(3): p. 727-733.
7. Wang, Y., et al., *Gas sensors based on deposited single-walled carbon nanotube networks for DMMP detection*. Nanotechnology, 2009. **20**(34): p. 345502.
8. Hersee, S. and J. Ballingall, *The operation of metalorganic bubblers at reduced pressure*. Journal of Vacuum Science & Technology A: Vacuum, Surfaces, and Films, 1990. **8**(2): p. 800-804.
9. Kim, Y.S., et al., *Gas sensor measurement system capable of sampling volatile organic compounds (VOCs) in wide concentration range*. Sensors and Actuators B: Chemical, 2007. **122**(1): p. 211-218.
10. Liu, Y., *Is the free energy change of adsorption correctly calculated?* Journal of Chemical & Engineering Data, 2009. **54**(7): p. 1981-1985.
11. wikipedia. *Langmuir adsorption model*. [web] [cited 2017 21 August]; Available from: [https://en.wikipedia.org/wiki/Langmuir\\_adsorption\\_model](https://en.wikipedia.org/wiki/Langmuir_adsorption_model).
12. Desimoni, E. and B. Brunetti, *About estimating the limit of detection by the signal to noise approach*. PHARMACEUTICA ANALYTICA ACTA, 2015. **6**(3): p. 1-4.
13. Sun, Y., et al., *Rapid chemical-vapor sensing using optofluidic ring resonators*. Optics letters, 2008. **33**(8): p. 788-790.
14. Yebo, N.A., et al., *An integrated optic ethanol vapor sensor based on a silicon-on-insulator microring resonator coated with a porous ZnO film*. Optics Express, 2010. **18**(11): p. 11859-11866.
15. Zhang, G., et al., *Gas Sensor for Volatile Organic Compounds Detection Using Silicon Photonic Ring Resonator*. Procedia Engineering, 2016. **168**: p. 1771-1774.
16. Some, S., et al., *Highly sensitive and selective gas sensor using hydrophilic and hydrophobic graphenes*. Scientific reports, 2013. **3**: p. 1868.
17. Yebo, N.A., et al., *Selective and reversible ammonia gas detection with nanoporous film functionalized silicon photonic micro-ring resonator*. Optics Express, 2012. **20**(11): p. 11855-11862.
18. Gong, H., et al., *Interaction between thin-film tin oxide gas sensor and five organic vapors*. Sensors and Actuators B: Chemical, 1999. **54**(3): p. 232-235.
19. Latif, U. and F.L. Dickert, *Graphene hybrid materials in gas sensing applications*. Sensors, 2015. **15**(12): p. 30504-30524.
20. Wang, L., et al., *Nanosensor device for breath acetone detection*. Sensor Letters, 2010. **8**(5): p. 709-712.

21. D. Kohl, W. Thoren, U. Schnakenberg, G. Schuell, G. Herland, Decomposition of gaseous acetic acid, J. Chem. Soc. Faraday Trans., 87 (16) (1991), pp. 2647-2653.
22. D. Kohl Surface process in the detection of reducing gases with SnO<sub>2</sub> based devices, Sensors and Actuators B, 18 (1989), pp. 71-113





## Chapter 8: Conclusions and future work

### 8.1 Conclusion

In this doctoral thesis, we proposed novel nano-photonic devices based on the integration of graphene and its chemical derivative GO with silicon photonic MRR devices. We investigated these devices by different optical and structural techniques and finally developed a simple vapour sensor, including a gas cell with optical access and a vapour handling system to provide controlled and reliable testing. In brief, a summary of the main contributions in this research are:

One of the first problems that we addressed in this project was achieving enhanced sensitivities from silicon MRRs through application of very large specific surface area coatings. As discussed in Chapter 4, monolayer graphene layers were deposited from material fabricated by the chemical vapour deposition (CVD) technique. A detailed analysis of the optical and structural characterization of several, different sized graphene integrated silicon MRRs were used to understand the practical limitations of graphene as a sensitization layer via its effect on the optical properties of such a device. Measurements and analysis of the transmission spectra for coated and uncoated cavities reveal a strong quenching of the resonance signal with increasing light-graphene interaction length. A model based on the calculated CVD graphene optical losses for different graphene lengths and heights on waveguide was successfully applied. This model provides design rules for optimised sensing and, photo-detector based applications.

A Raman mapping study of graphene coated MRRs to investigate the effects of the transfer process on its structural and optoelectronic properties including analysis of the Raman G and 2D peak positions and relative intensities revealed that the graphene is intrinsic where it is suspended over the MRR but is moderately hole-doped where it sits on top of the waveguide structure.

The strong absorption of guided light by the graphene coating makes it undesirable for optical sensing applications. Rather, we proposed a functionalization based on GO. The spectral responses of the uncoated and different GO concentrations coated MRRs provided precise determination of the attenuation coefficient of the GO. This study

revealed the GO layer on silicon MRRs has lower in-plane optical attenuation coefficient which make it more suitable for chemical sensing based ring resonators. Finally, chemical vapour sensing measurements of uncoated and GO coated MRRs were exposed to a series of organic solvents; ethanol, pentane, and acetone. The experimental results indicated that the sensitivity and response of GO coated cavity was always significantly higher than that of the uncoated devices for all vapours tested and there is some indication of a level of selectivity between the solvents, despite their similar refractive index.

## **8.2 Future work**

In this PhD Thesis, we have worked in the development of chemical sensing devices based RRs using graphene and derivative material for their functionalization, and significant progress has been made in this work. However, there still a several ways to follow and a further work needs to be done to develop these sensing devices before a practical sensing system be deployed into the commercial market. These are listed as follows:

- MRRs based CVD graphene coatings require further modification without huge losses before it will be able to use as functional layer integrated with optical cavity resonators. Device optimization with precise control of CVD graphene transfer and control over its relative height over the waveguide will be important, as will controlling the graphene length. Controlling these parameters are essential to ensure CVD graphene does not quench resonances in transmission spectra and these will hopefully offer the enhancement of these devices and hence the ability to use these devices for bio/chemical sensing based ring resonator.
- Raman measurements and tests need to be conducted while pumping the MRR devices (i.e. injecting Raman laser inside the devices instead of at normal incident). This could give more insight on the effect of graphene's properties on the silicon device structures or vice versa.

- During the real time measurements of the vapour sensing we observed problem related to the signal drift and its stabilization which effects adversely to the system performance. In order to minimize this problem, we suggest the implementation of a temperature control system in the optical spectroscopic setup in order to compensate the environmental temperature variations and reduce intensity noise during the measurements.
- The work which was conducted with the gas cell and vapour handling system requires a level of automation to improve testing and a wider range of technologically important gases (e.g. NO and CH<sub>4</sub>) for various applications should be explored to assess real benefit of this type of sensor, benchmarked against existing sensor technologies.
- Although GO coated MRRs based sensor has high sensitivity to different vapours at room-temperature, future research efforts will be directed towards other characteristics such as, selectivity by exposing the sensor to different vapours/gases, and reversible by developing synthesis techniques in GO, and improving the “poisoning” of GO sensor by heat treatment.